



THE UNIVERSITY OF
WAIKATO
Te Whare Wānanga o Waikato

Research Commons

<http://researchcommons.waikato.ac.nz/>

Research Commons at the University of Waikato

Copyright Statement:

The digital copy of this thesis is protected by the Copyright Act 1994 (New Zealand).

The thesis may be consulted by you, provided you comply with the provisions of the Act and the following conditions of use:

- Any use you make of these documents or images must be for research or private study purposes only, and you may not make them available to any other person.
- Authors control the copyright of their thesis. You will recognise the author's right to be identified as the author of the thesis, and due acknowledgement will be made to the author where appropriate.
- You will obtain the author's permission before publishing any material from the thesis.

**Variations to the Groundwater Seepage Face
on Meso-tidal Dissipative Beaches**

A thesis

submitted in fulfilment

of the requirements for the degree

of

Doctor of Philosophy in Earth Sciences

at

The University of Waikato

by

Amir Emami



THE UNIVERSITY OF
WAIKATO
Te Whare Wānanga o Waikato

June 2016

Dedication

To my family

Abstract

Groundwater seeping from the beachface can induce erosion and so may play a role in controlling the development of beach morphology. This research answers some fundamental questions about the processes that control the groundwater seepage line position on a dissipative beach. For instance: What is the relationship between the observed groundwater seepage line and the intertidal beachface volume? What is the best statistical model, which can describe the importance of the groundwater seepage line and surfzone morphology in changing the beachface volume? How well can video images be used for extracting groundwater seepage lines and shorelines at a dissipative meso-tidal beach? How does the groundwater seepage line on a dissipative meso-tidal beach change over the tidal cycle? What are the main parameters controlling the groundwater seepage line on a dissipative, meso-tidal beach and which driver is the most important in explaining changes to the seepage line? Can numerical models (both linear and non-linear) accurately predict the tidal groundwater changes across the beachface and determine the position of the groundwater exit point?

The processes that are explored are rip currents, characterized by the observed variations in the surfzone morphology, as well as beach slope, hydraulic conductivity, wave set-up, tidal variations and water table variations. Specifically, changes to the alongshore variation and decoupling of the seepage line from the shoreline are studied along two gently-sloping beaches in the west coast of New Zealand using video images, field measurements and a 2D non-linear Boussinesq model. Finally the advantages and disadvantages of applying the linear versus the non-linear Boussinesq equations to beach groundwater modelling are discussed. The thesis also demonstrates the accuracy of using video images for extracting the seepage line and shoreline.

The statistical study conducted using video imagery and surveys of the seepage line at Muriwai Beach showed that the variation of the beach volume can be related to the seepage line and surfzone morphology, (which was measured using the pixel

intensity extracted from the time-averaged video images). My results showed that in most regions of the beach, there is a clear correlation between the beachface volume and the seepage line, with an elevated seepage line causing a reduction of volume. This inverse correlation occurred in all datasets. The seasonal analysis showed that the seepage line in winter is more correlated with volume than summer. The field results also indicated that the beachface volume is more correlated with the seepage line at low tide rather than high tide. Hence, the seepage line has a greater effect lower on the beach, and beachface volume reduction is more influenced by the low tide seepage line. This study also showed that the seepage line was less clearly related to changes in the surfzone morphology.

One of the shortcomings of the study at Muriwai Beach was the lack of survey data and the inability to use the video imagery more effectively because of the lack of ground truthing. Therefore images collected at Ngarunui Beach, where cameras were still operating, were used to study the application of the time-averaged images in extracting the seepage line and variance images in detecting the shoreline. The comparison between the extracted shoreline and beach survey data showed that the difference between the surveyed data and video based data in upper intertidal beach is much lower than lower part of the beach indicating that the video extracting algorithm works better at the high tide rather than the low tide. On the other hand, both seepage line and shoreline showed the decoupling process very well in both incoming and outgoing tides. During the rising tide, the infiltration from the tidal wave causes the water table rise, although beach groundwater level increases much more quickly than rising tide. An hourly comparison of the decoupling process showed that the seepage line decouples from the shoreline more quickly on the lower part (less steep intertidal beachface) rather than the steeper upper part of the beach profile. This decoupling process showed that Ngarunui Beach fills more rapidly than the tide rises, and drains more slowly than tide falls. This finding was tested using my field data collected using Solinst piezometers -Solinst is the brand name of the piezometers which were used at Ngarunui Beach- and manual water detectors at the beach. The decoupling between the seepage line and the shoreline extracted from video images also showed that the seepage face width is much greater in north and

middle of the beach rather than south part. The rip current in south of the beach may have an effect on lowering the groundwater exit point elevation and shortening the seepage face width. Although according to the data from the current meters deployed in the beach, it seems that the rips may have a small effect on changing the groundwater seepage line rather than sediment properties and beach topography.

Modelling using a 2D non-linear Boussinesq model, which I developed during the research, showed that the seepage line calculated by my model is compatible with the surveyed seepage line. The non-linearity effect of the hydraulic conductivity and the groundwater depth may play an important role in accuracy of the results. The non-linear model also showed the same pattern of the decoupling between the seepage line and the shoreline as the video images showed. Similar to the result of my 1D numerical model at Muriwai beach, the numerical model results at Ngarunui beach also showed that the seepage line elevation decreases with increasing the hydraulic conductivity and intertidal beachface slope. The model successfully replicated the wider seepage face in middle and north of the beach rather the south (also shown in the video image analysis).

Acknowledgments

I would like to thank my chief supervisor Associate Professor Karin Bryan (UoW) for her kind attention and giving me this opportunity to do my programme under her supervision. I would also like to thank my second supervisor Dr Willem de Lange (UoW) for his kind help and support. Many thanks to Professor David Lowe (UoW) for his kind attention. I really appreciate them.

I am grateful for the University of Waikato and New Zealand Coastal Society for funding this study. Thanks to the staff in School of Science for being helpful during these years, especially Sydney Wright. I would like to thank Amy Robinson (Waikato Regional Council), for her work and sampling in Muriwai Beach and Rafael Guedes for providing Ngarunui Images. Thanks to Dean Sandwell, Annette Rodgers, Dirk Immenga, Christopher Paul Morcom, Alex Port, Shawn Harrison, Steve Hunt, Neeltje De Groot and Justy Park for helping me with Ngarunui field data sampling.

I really appreciate Leila for her kindly support and encouragement. Also many thanks to Maryam. I should appreciate my mum and dad back home for all their support, help and encouragement from when I was child until now, when I am 16,000 km away from them.

Thank GOD.

Whakawhetai ATUA.

Table of Contents

Abstract	iii
Acknowledgments	vi
Table of Contents	vii
List of Figures	xi
List of Symbols	xxi
Chapter 1 : Introduction	1
1.1 Thesis topic and its significance	2
1.2 Thesis aims and objectives	3
1.3 Beach field sites	5
1.4 Thesis structure	6
Chapter 2 : Literature Review	7
2.1 Beach groundwater and erosion	8
2.2 Video techniques	17
Chapter 3 : Groundwater Seepage and Surfzone Morphology Control on Muriwai Beachface Volume	25
3.1 Introduction	26
3.2 Field data	30
3.2.1 Site description	30
3.2.2 Surveying data	31
3.3 Methods	33

3.3.1	Video images.....	33
3.3.2	Statistical methods	35
3.3.3	Numerical modelling.....	36
3.4	Field data analysis and results	39
3.5	The numerical model results	43
3.6	Discussion	49

Chapter 4 : The Use of the Video Imagery to Extract the Groundwater Seepage Line and Shoreline at Ngarunui Beach..... 53

4.1	Introduction	54
4.2	Field data	55
4.2.1	Site description.....	55
4.2.2	Video images.....	56
4.2.3	Survey data.....	58
4.3.	Methods	59
4.3.1	Extracting Seepage line from time-averaged images.....	60
4.3.2	Extracting Shore line from Variance images	62
4.4.	Results	64
4.4.1	Groundwater seepage line detected at Ngarunui beach	64
4.4.2	Shoreline detected at Ngarunui beach.....	67
4.4.3	Decoupling between the groundwater seepage line and the shoreline..	70
4.5.	Discussion	72

Chapter 5 : Ngarunui Beach Field Data Collection	79
5.1 Introduction	80
5.2 Field data	83
5.2.1 Survey data.....	83
5.2.2 Sediment sampling and hydraulic conductivity	85
5.3 Methods, instrument data and results	87
5.3.1 ISD deployment and long-term water table variation.....	87
5.3.2 Solinst piezometers deployment and short-term groundwater variation 89	
5.3.3 Dipwells and manual beach groundwater level detecting.....	91
5.3.4 <i>ADV</i> deployment and wave data	93
5.4 Discussion	101

Chapter 6 : The Use of the 2D Boussinesq Equation to Analyse the Groundwater Seepage Line on Ngarunui Beach

107	
6.1 Introduction	108
6.2 Field data	110
6.2.1 Beach surveying data and groundwater table measurement	110
6.2.2 Tide and Wave data.....	112
6.3 Methods	113
6.3.1 Numerical Model based on Linear Boussinesq equation.....	114
6.3.2 Numerical Model based on Non-linear Boussinesq equation	115
6.3.3 Using Numerical Model in Ngarunui Beach.....	116
6.4 Sensitivity of the numerical model to involved factors.....	118
6.4.1 Sensitivity of the model to the time interval (Δt).....	118

6.4.2	Sensitivity of the model to the hydraulic conductivity (<i>K</i>).....	120
6.4.3	Sensitivity of the model to the inland water table (<i>WT</i>).....	122
6.4.4	Sensitivity of the model to the wave set-up (<i>S-U</i>)	124
6.5	Numerical modelling results.....	126
6.5.1	Groundwater exit point and extent of the seepage face	126
6.5.2	Comparison between the numerical model results and surveyed groundwater seepage line.....	130
6.6	Discussion	132
6.7	Conclusion.....	138
Chapter 7 : Conclusions		140
References		149
Appendix A: Field Data Collection.....		157

List of Figures

FIGURE 2.1 PARAMETERS USED IN FORMULATING THE COASTAL BOUNDARY CONDITION FOR GROUNDWATER MODELING. SWS (STILL WATER SURFACE): THE SMOOTH SEA SURFACE WITHOUT CONSIDERING WAVES THAT FLUCTUATES WITH CHANGES IN ATMOSPHERIC PRESSURE AND TIDES; MWS (MEAN WATER SURFACE): THE LOCAL SHORT TIME AVERAGING OF THE WATER ELEVATION, AND IS AVERAGED OVER THE SCALE OF INDIVIDUAL WAVES; SL: THE SHORELINE POSITION AND RL IS RUN-UP LIMIT. (NIELSEN, 1999)..... 9

FIGURE 2.2 A SNAP-SHOT OF SWASH AND GROUNDWATER SEEPAGE LINE AT RAGLAN BEACH. GROUNDWATER SEEPAGE FACE APPEARS AS A SHINY AREA BETWEEN SEEPAGE LINE AND SHORELINE. (HUISMAN ET AL., 2011). 10

FIGURE 2.3 THE SKETCH OF THE SEEPAGE FACE AND DEFINITION OF THE EXIT POINT (TURNER, 1993)..... 11

FIGURE 2.4 SEEPAGE FACE PARAMETER AS A FUNCTION OF TIDE RANGE (TR), HYDRAULIC CONDUCTIVITY AND BEACHFACE SLOPE (TURNER, 1995) 12

FIGURE 2.5 DECOUPLING BETWEEN THE TIDE (SOLID LINE) AND GROUNDWATER EXIT POINT (DASHES); AND FORMATION OF THE SEEPAGE FACE (LI ET AL., 1997). 13

FIGURE 2.6 SEEPAGE FACE EXTENT ACROSS THE INTERTIDAL PROFILE (TURNER, 1998).. 13

FIGURE 2.7 DECOUPLING BETWEEN THE SHORELINE (CIRCLES) AND SEEPAGE LINE (TRIANGLES); A: THE DIFFERENCE BETWEEN THE SEEPAGE LINE AND SHORELINE IS SIMILAR AT LOW TIDE AND HIGH TIDE. B: THE DIFFERENCE IS MUCH LARGER AT LOW TIDE THAN HIGH TIDE. (HUISMAN ET AL., 2011). 14

FIGURE 2.8 CONCEPTUAL MODEL OF THE RELATIONSHIP BETWEEN BEACH GROUNDWATER AND SEDIMENT TRANSPORT IN THE SWASH ZONE (AFTER GRANT 1948; BAIRD AND HORN, 1996)..... 15

FIGURE 2.9 PIC DETECTION METHOD IN EXTRACTING SHORELINE FROM VIDEO IMAGES (AARNINKHOF ET AL., 2003). 21

FIGURE 2.10 CCD METHOD. THE DIVERGENCE OF THE RED AND BLUE INTENSITY SHOWS THE SHORELINE LOCATION (PLANT ET AL., 2007)..... 22

FIGURE 2.11	COMPARISON BETWEEN DIFFERENT SHORELINE DETECTING METHODS (PLANT ET AL., 2007).	22
FIGURE 2.12	A SCHEMATIC OF THE BEACH PROFILE AND BEST FIT LINE OF THE INTERTIDAL PROFILE DETERMINED FROM THE HOURLY VIDEO IMAGES (SMITH AND BRYAN, 2007).	23
FIGURE 3.1	LEFT PANEL: LOCATION OF THE FIELD SITE ON THE NORTHWEST COAST OF THE NORTH ISLAND OF NEW ZEALAND; RIGHT PANEL: AERIAL IMAGE OF THE MURIWAI BEACH AND THE STUDIED ZONE (IMAGE RETRIEVED FROM LAND INFORMATION, NEW ZEALAND).	30
FIGURE 3.2	SURVEYING DATA IN FEBRUARY 2003 INCLUDING FOUR GROUNDWATER SEEPAGE LINE MEASUREMENTS AND THREE BEACH PROFILES (THE PROFILES ARE THREE LINES THAT RUN PERPENDICULAR TO THE BEACH). THE AREA BETWEEN RED DASHED LINE AND RED DASHED-DOT LINE INDICATES THE INTERTIDAL BEACH ZONE.	32
FIGURE 3.3	PANEL A: STRAIGHTENED AND INTERPOLATED TIME-AVERAGED IMAGE IN FEBRUARY 2003 (TAKEN AT LOW TIDE). THE AREA BETWEEN THE HORIZONTAL BLACK LINE AND DASH LINE INDICATES THE INNER ZONE; AND THE OUTER ZONE IS SPECIFIED BETWEEN THE BLACK LINE AND THE DOT-DASH LINE. IN THE TOP OF THE IMAGE, TICKER BLUE LINE SHOWS THE LOWER SEEPAGE LINE AMONG FOUR OBSERVED SEEPAGE LINES. PANEL B: VARIATIONS OF THE PIXEL INTENSITY VERSUS ALONGSHORE DISTANCE.	34
FIGURE 3.4	BEACH GROUNDWATER PROFILE DURING A TIDAL CYCLE (EXAMPLE FOR A BEACH PROFILE IN FEBRUARY)	37
FIGURE 3.5	PANEL A: THE VARIATION OF THE R-SQUARE VALUES FOR MODEL 3 ($V_o = a_1 + a_2 \times GWSL + a_3 \times SM$) VERSUS WINDOW SIZES IN 5 MONTHS. PANEL B: THE VARIATION OF THE F-STATISTIC WITH WINDOW SIZE AND THE ZONE OF STATISTICALLY SIGNIFICANT RESULTS (AT A=5 AND 10%).	39
FIGURE 3.6	VARIATION OF THE ALONGSHORE-AVERAGED R-SQUARE VERSUS DIFFERENT MODELS IN FIVE MONTHS. THE BLACK SQUARES SHOW THE STATISTICALLY SIGNIFICANT RESULTS AT A=5%.	40
FIGURE 3.7	PANEL A: THE ALONGSHORE VARIATION OF THE INTERTIDAL BEACHFACE VOLUME. PANEL B: THE GROUNDWATER SEEPAGE LINE ELEVATION (SOLID BLACK LINE) AND THE PIXEL INTENSITY (DASHED GREEN LINE). PANEL C: REGRESSION R-SQUARE	

VALUES. DASHED BLUE LINE: USING JUST GROUNDWATER SEEPAGE LINE (MODEL 1), GREEN LINE: USING JUST PIXEL INTENSITY -OR SURFZONE MORPHOLOGY- (MODEL 2) AND THICKER BLACK LINE: USING A REGRESSION MODEL WITH BOTH GROUNDWATER AND SURFZONE MORPHOLOGY (MODEL 3). PANEL D: THE RECTIFIED AVERAGED VIDEO IMAGE OF MURIWAI BEACH IN FEBRUARY 2003. SHOREWARD IS AT THE TOP AND SEAWARD AT THE BOTTOM. THIS IS TAKEN FROM THE ARGUS VIDEO NETWORK BY R. A. HOLMAN ([HTTP://CIL-WWW.OCE.ORST.EDU/](http://CIL-www.oce.orst.edu/)) 41

FIGURE 3.8 PANEL A AND B: THE ALONGSHORE VARIATION OF INTERTIDAL BEACHFACE VOLUME AND DIFFERENT GROUNDWATER SEEPAGE MEASUREMENTS IN FEBRUARY 2003. PANEL C: VARIATION OF R-SQUARE VERSUS DIFFERENT MEAN GROUNDWATER ELEVATIONS IN 3 MONTHS. THE R-SQUARE VALUES ARE ONLY FOR THE REGRESSION BETWEEN VOLUME AND GROUNDWATER (MODEL 1). 42

FIGURE 3.9 VARIATION OF THE GROUNDWATER SEEPAGE LINE ELEVATION VERSUS THE INLAND GROUNDWATER TABLE, TIDE ELEVATION AND WAVE SET-UP 43

FIGURE 3.10 OBSERVED GROUNDWATER SEEPAGE LINE (GWSL) AND VARIATION OF THE NUMERICAL MODEL RESULTS VERSUS HYDRAULIC CONDUCTIVITY (K) AND INTERTIDAL BEACH SLOPE (S). PANEL A: THE OBSERVED GWSL ELEVATION COLLECTED AT MURIWAI BEACH. PANEL B: THE MODEL RESULTS, WHICH WERE CALCULATED WITH DIFFERENT VALUES OF K. EACH CURVE INDICATES A SPECIFIED S. PANEL C: THE MODELED GWSL, WHICH WAS OBTAINED WITH DIFFERENT VALUES OF S. PANEL D: THE HISTOGRAM OF K, WHICH WAS CALCULATED BASED ON THE FIELD SAMPLING. PANEL E: THE HISTOGRAM OF S OBTAINED FROM THE BEACH SURVEY. 45

FIGURE 3.11 PANELS A AND B: ALONGSHORE VARIATION OF THE NUMERICAL MODEL RESULTS AND OBSERVED GROUNDWATER SEEPAGE LINE IN FEBRUARY, AT 2 AND 6 HOURS AFTER THE HIGH TIDE, RESPECTIVELY. PANEL C: ALONGSHORE VARIATION OF THE OPTIMIZED WAVE SET-UP. PANELS D AND E: RELATION BETWEEN THE MODELLED AND OBSERVED GWSL AT 2 AND 6 HOURS AFTER THE HIGH TIDE, RESPECTIVELY..... 48

FIGURE 3.12 PANELS A AND B: ALONGSHORE VARIATION OF THE NUMERICAL MODEL RESULTS AND OBSERVED GROUNDWATER SEEPAGE LINE IN AUGUST, AT 2 AND 6 HOURS AFTER THE HIGH TIDE, RESPECTIVELY. PANEL C: ALONGSHORE VARIATION OF THE OPTIMIZED WAVE SET-UP. PANELS D AND E: RELATION BETWEEN THE MODELED AND OBSERVED GWSL AT 2 AND 6 HOURS AFTER THE HIGH TIDE, RESPECTIVELY..... 48

FIGURE 3.13	SCHEMATIC OF THE BEACH, AND THE EFFECT OF THE GROUNDWATER SEEPAGE LINE AND SURFZONE MORPHOLOGY ON CHANGING THE INTERTIDAL BEACHFACE VOLUME. (A) FOR THE WINTER PATTERN, WHERE SURFZONE MORPHOLOGY AND BEACH VOLUME ARE POSITIVELY CORRELATED; (B) FOR THE SUMMER PATTERN, WHERE SURFZONE MORPHOLOGY AND BEACH VOLUME ARE NEGATIVELY CORRELATED.	51
FIGURE 4.1	LOCATION OF THE NGARUNUI BEACH ON THE WEST COAST OF THE NORTH ISLAND	55
FIGURE 4.2	UPPER PANEL: VIDEO CAMERAS PLACED ON THE TOP OF THE HOME AT NGARUNUI BEACH. LOWER PANELS: TIME-AVERAGED VIDEO IMAGES AT NGARUNUI BEACH AT HIGH TIDE AND LOW TIDE	57
FIGURE 4.3	LEFT PANEL: SURVEY TRACKS (GUEDES, 2010). RIGHT PANEL: SURFACE MAP OBTAINED FROM THE BEACH SURVEYS.	58
FIGURE 4.4	PANEL A: AN EXAMPLE OF THE VALUE (V) VARIATION IN A SINGLE PIXEL ROW OF A TIME-AVERAGED IMAGE. THE THRESHOLD USED FOR DETECTING THE SEEPAGE LINE IS INDICATED WITH A HORIZONTAL BLACK DASH-DOT. THE VERTICAL LINE SHOWS THE CROSS-SHORE LOCATION OF THE GROUNDWATER EXIT POINT. PANEL B: A TIME-AVERAGED AT 7:10 AM ON 8 TH NOVEMBER 2010. THE HORIZONTAL RED DASH-DOT SHOWS THE SELECTED PIXEL ROW FOR V VARIATION AND THE CIRCLE INDICATES THE EXIT POINT ON THE ALONGSHORE SEEPAGE LINE.....	61
FIGURE 4.5	PANEL A: AN EXAMPLE OF THE INTENSITY (I) VARIATION IN A SINGLE PIXEL ROW OF A VARIANCE IMAGE. THE VERTICAL DASH-DOT LINE SHOWS THE CROSS-SHORE LOCATION OF THE AVERAGE SHORELINE. PANEL B: VARIANCE IMAGE AT 7:10 AM ON 8 TH NOVEMBER 2010. THE HORIZONTAL RED DASH-DOT SHOWS THE SELECTED PIXEL ROW FOR I VARIATION AND THE CIRCLE INDICATES THE SHORELINE POSITION.....	63
FIGURE 4.6	DETECTED GROUNDWATER SEEPAGE LINES FROM TIME-AVERAGED VIDEO IMAGES AT NGARUNUI BEACH DURING RISING TIDE ON 08/11/2010	65
FIGURE 4.7	DETECTED GROUNDWATER SEEPAGE LINES FROM TIME-AVERAGED VIDEO IMAGES AT NGARUNUI BEACH DURING FALLING TIDE ON 08/11/2010	66
FIGURE 4.8	DETECTED SHORELINES (RED LINES) FROM VARIANCE VIDEO IMAGES AT NGARUNUI BEACH DURING RISING TIDE ON 08/11/2010.....	68

FIGURE 4.9 DETECTED SHORELINES (RED LINES) FROM VARIANCE VIDEO IMAGES AT NGARUNUI BEACH DURING FALLING TIDE ON 08/11/2010..... 69

FIGURE 4.10 DECOUPLING BETWEEN THE GROUNDWATER SEEPAGE LINE EXTRACTED FROM TIME-AVERAGED IMAGES (BLACK LINE) AND THE SHORELINE DETECTED FROM VARIANCE IMAGES (RED LINE) DURING RISING TIDE ON 8TH NOVEMBER 2010. THE SURFACE MAP OBTAINED FROM THE BEACH SURVEYS CARRIED OUT ON 8TH AND 9TH NOVEMBER (GUEDES, 2010) IS ALSO SHOWN IN THE BACKGROUND. 71

FIGURE 4.11 DECOUPLING BETWEEN THE GROUNDWATER SEEPAGE LINE EXTRACTED FROM TIME-AVERAGED IMAGES (BLACK LINE) AND THE SHORELINE DETECTED FROM VARIANCE IMAGES (RED LINE) DURING FALLING TIDE ON 8TH NOVEMBER 2010. THE SURFACE MAP OBTAINED FROM THE BEACH SURVEYS CARRIED OUT ON 8TH AND 9TH NOVEMBER (GUEDES, 2010) IS ALSO SHOWN IN THE BACKGROUND. 71

FIGURE 4.12 PANEL A: SURFACE MAP OBTAINED FROM THE BEACH SURVEYS. PANEL B: CALCULATED SURFACE MAP (USING DETECTED SHORELINES FROM VARIANCE IMAGES) DURING INCOMING TIDE. PANEL C: CALCULATED SURFACE MAP DURING OUTGOING TIDE. 74

FIGURE 4.13 DIFFERENCE BETWEEN THE SURVEYED SURFACE MAP AND CALCULATED SURFACE MAP (BASED ON DETECTED SHORELINES) DURING INCOMING TIDE (PANEL A) AND OUTGOING TIDE (PANEL B). SHORELINES, WHICH WERE EXTRACTED FROM VARIANCE IMAGES EVERY HALF HOUR, ARE SHOWN IN BOTH PANELS. 74

FIGURE 4.14 THE ERROR OF THE EXTRACTING SHORELINE METHOD FROM VARIANCE VIDEO IMAGES AT NGARUNUI BEACH. 75

FIGURE 4.15 DECOUPLING BETWEEN GWSL EXTRACTED FROM TIME-AVERAGED IMAGES AND SL DETECTED FROM VARIANCE IMAGES (LEFT PANEL AT LOW TIDE AND RIGHT PANEL AT HIGH TIDE). THE RECTANGULAR SHOWS THE STUDY AREA FOR THE FIELD WORK AND DASH LINES INDICATE THREE TRANSECTS (CHAPTER 5). 77

FIGURE 4.16 PHOTO TAKEN ON 15TH AUGUST 2015 AT 4PM (AT LOW TIDE) AT NGARUNUI BEACH. UPPER PANEL SHOWS A PANORAMA VIEW OF THE BEACH. LOWER PANEL SHOWS THE STUDY AREA. 78

FIGURE 5.1 UPPER PANEL: STUDIED AREA ON THE RECTIFIED TIME-AVERAGED IMAGE. HIGH TIDE AND LOW TIDE SOLINST PIEZOMETERS ARE SHOWN WITH SQUARES (E.G. T1SHT, T1SLT). CIRCLES AND DASHED CIRCLES SHOW DIPWELLS (E.G. T1D1,..., T1D7). BLACK CIRCLES INDICATE ADVs (E.G. T1ADV). YELLOW SQUARE SHOWS THE ISD STATION. THREE CROSS-SHORE TRANSECTS (T1, T2 AND T3) AND APPROXIMATE SHORELINE AT HIGH TIDE AND LOW TIDE ARE ALSO SHOWN. LOWER PANEL: PHOTO TAKEN IN NGARUNUI BEACH, SHOWING THREE TRANSECTS (FROM RIGHT TO LEFT: T1, T2 AND T3)..... 81

FIGURE 5.2 A SCHEMATIC CROSS-SHORE TRANSECT SHOWING THE RELATIVE POSITION OF DEPLOYED INSTRUMENTS ALONG EACH OF THE 3 TRANSECTS. ISD: LONG-TERM WATER TABLE RECORDER (ONLY ONE ISD BEHIND THE DUNE). SHT: THE HIGH TIDE SOLINST PIEZOMETER, WHICH WAS A PIEZOMETER LOCATED AT HIGH TIDE, MEASURING SHORT-TIME BEACH GROUNDWATER VARIATIONS). SLT: THE LOW TIDE SOLINST PIEZOMETER, WHICH WAS A PIEZOMETER LOCATED AT LOW TIDE. ADV: THE ACOUSTIC DOPPLER VELOCIMETER, WHICH WAS A DEVICE DEPLOYED IN SWASH ZONE FOR MEASURING WAVE CHARACTERISTICS. D1, 2, ETC: DIPWELLS FOR MANUAL GROUNDWATER DETECTION. 82

FIGURE 5.3 SURVEY DATA FROM NGARUNUI BEACH, 18 AND 19 SEPTEMBER 2013..... 83

FIGURE 5.4 PANEL A: SURVEYED GROUNDWATER SEEPAGE LINE (GWSL) FROM 18TH SEPTEMBER 2013 AT 11:35 AM (MID TIDE) AND 12:25 PM (1 HOUR AFTER MID TIDE) (GWSL 1, AND 2). PANEL B: GWSL ON 19TH SEPTEMBER AT 10:45 AM (1.5 HOUR AFTER HIGH TIDE) AND 01:10 PM (1 HOUR AFTER MID TIDE) (GWSL 3, AND 4) 84

FIGURE 5.5 UPPER PANEL: LOCATION OF SEDIMENT SAMPLES ALONG THE THREE TRANSECTS. LOWER PANEL: SEDIMENT HYDRAULIC CONDUCTIVITY VARIATION ALONG THE THREE TRANSECTS. 86

FIGURE 5.6 WATER TABLE VARIATION ON NGARUNUI BEACH DURING THE 3 MONTH TIME PERIOD. 88

FIGURE 5.7 SCHEMATIC OF THE SOLINST PIEZOMETER DEPLOYED IN NGARUNUI BEACH. THE BROWN LINE IS THE BEACH SURFACE AND THE BLUE LINE REPRESENTS THE WATER TABLE. SYMBOLS ARE THE SAME AS USED IN EQ. 5.2. 90

FIGURE 5.8 SHORT-TERM BEACH GROUNDWATER VARIATION MEASURED BY THE SOLINST PIEZOMETERS. THE THREE UPPER LINES REPRESENT MEASUREMENTS FROM THE HIGH

TIDE LOCATIONS ON EACH TRANSECT (T1SHT, T2SHT, AND T3SHT) AND THE TWO LOWER LINES SHOW MEASUREMENTS AT THE LOW TIDE LOCATIONS (T1SLT AND T2SLT). THE THICKER BLACK LINE SHOWS TIDE VARIATION. THE DAYLIGHT HOURS DURING THE EXPERIMENT (18 AND 19TH SEPTEMBER 2013) ARE INDICATED IN THE FIGURE. 90

FIGURE 5.9 PANELS A AND B: THE LOCATION OF DIPWELLS ALONG THREE TRANSECTS IN NORTHING-EASTING AND ALONGSHORE-CROSS SHORE COORDINATE SYSTEMS. PANEL C: GROUNDWATER ELEVATION MEASURED IN DIPWELLS DURING THE FALLING TIDE. THE LINES REPRESENT THE BEACH SURFACE ELEVATION. 92

FIGURE 5.10 (1): ADV 1 AT HIGH TIDE. PANEL A: WATER DEPTH (ADV PRESSURE IN METRES, RELATIVE TO MEAN SEA LEVEL) WITHIN ONE BURST (20 MINUTES). PANEL B: VARIATION OF WAVE-INDUCED VELOCITIES IN CROSS-SHORE AND ALONGSHORE DIRECTION (UW AND VW). PANEL C: VW VERSUS UW. PANEL D: VARIATION OF THE WAVE SPECTRAL DENSITY (MODIFIED PERIODOGRAM SPECTRAL ESTIMATION USING WELCH METHOD) VERSUS FREQUENCY. 95

FIGURE 5.11 (1): ADV 2 AT HIGH TIDE. PANEL A: WATER DEPTH (ADV PRESSURE IN METRES, RELATIVE TO MEAN SEA LEVEL) WITHIN ONE BURST (20 MINUTES). PANEL B: VARIATION OF WAVE-INDUCED VELOCITIES IN CROSS-SHORE AND ALONGSHORE DIRECTION (UW AND VW). PANEL C: VW VERSUS UW. PANEL D: VARIATION OF THE WAVE SPECTRAL DENSITY (MODIFIED PERIODOGRAM SPECTRAL ESTIMATION USING WELCH METHOD) VERSUS FREQUENCY. 96

FIGURE 5.12 (1): ADV 3 AT HIGH TIDE. PANEL A: WATER DEPTH (ADV PRESSURE IN METRES, RELATIVE TO MEAN SEA LEVEL) WITHIN ONE BURST (20 MINUTES). PANEL B: VARIATION OF WAVE-INDUCED VELOCITIES IN CROSS-SHORE AND ALONGSHORE DIRECTION (UW AND VW). PANEL C: VW VERSUS UW. PANEL D: VARIATION OF THE WAVE SPECTRAL DENSITY (MODIFIED PERIODOGRAM SPECTRAL ESTIMATION USING WELCH METHOD) VERSUS FREQUENCY. 97

FIGURE 5.13 PANEL A: TIDE VARIATION IN 18TH AND 19TH SEPTEMBER 2013 AT NGARUNUI BEACH. PANELS B, C AND D: VARIATION OF THE MODIFIED POWER SPECTRAL DENSITY (PSD) VERSUS DIFFERENT WAVE FREQUENCIES OVER ALL ADV BURSTS ALONG TRANSECTS 1, 2 AND 3 RESPECTIVELY. 98

FIGURE 5.14 PANEL A: TIDE VARIATION IN 18TH AND 19TH SEPTEMBER 2013 AT NGARUNUI BEACH. PANELS B AND C: VARIATION OF THE MODIFIED POWER SPECTRAL DENSITY OVER ADV BURSTS FOR INFRAGRAVITY AND INCIDENT WAVES. 99

FIGURE 5.15 PANEL A: VARIATION OF THE AVERAGE ADV PRESSURE (WATER DEPTH) AND TIDE (BLACK LINE) VERSUS TIME ELAPSED FROM 12 AM ON 18TH SEPTEMBER 2013. PANEL B AND C: VARIATION OF THE CROSS-SHORE AND ALONGSHORE VELOCITIES VERSUS TIME, RESPECTIVELY..... 100

FIGURE 5.16 INSTRUMENT DEPLOYMENT RESULTS. UPPER HORIZONTAL LINE SHOWS THE HIGH TIDE SOLINST PIEZOMETERS AND LOWER LINE SHOWS THE LOW TIDE PIEZOMETERS. THE BLACK LINE PRESENTS TIDE DATA AND CIRCLES INDICATES THE LOCATION OF DIPWELLS AND GROUNDWATER ELEVATION MEASURED IN THEM. (PANEL A, B AND C: TRANSECTS 1, 2 AND 3 RESPECTIVELY). 102

FIGURE 5.17 VARIATION OF THE BEACH GROUNDWATER ELEVATION (MEASURED IN DIPWELLS AND GRIDDED) VERSUS TIME IN THREE TRANSECTS. BLACK HORIZONTAL LINES SHOW THE LOCATION OF THE SOLINST PIEZOMETER AND BLACK DOTS INDICATES THE DIPWELL LOCATIONS. PANELS A, B AND C SHOWS THE RESULTS IN THE FIRST FIELD WORK (18TH SEPTEMBER 2013) IN TRANSECTS 1, 2 AND 3 RESPECTIVELY. PANELS D, E AND F PRESENTS RESULTS FROM THE SECOND FIELD WORK (19TH SEPTEMBER 2013) ALONG THE THREE TRANSECTS. 104

FIGURE 5.18 DIFFERENCE BETWEEN THE GROUNDWATER ELEVATION BETWEEN TWO TRANSECTS. PANEL A, C: BETWEEN TRANSECTS 1 AND 2 IN THE FIRST AND SECOND DAY RESPECTIVELY. PANEL B, D: BETWEEN TRANSECTS 2 AND 3 IN THESE TWO DAYS. 105

FIGURE 6.1 MESH GRID OF BEACH SURFACE ELEVATION AT NGARUNUI BEACH. TRANSECTS 1, 2 AND 3 ARE SHOWN WITH GREEN (TOP), RED AND BLUE (BOTTOM) LINES RESPECTIVELY. A BLACK DIAMOND IN DUNE SHOWS THE ISD LOCATION. ALONG EACH TRANSECT, THE CIRCLES SHOW THE HIGH TIDE AND LOW TIDE SOLINST PIEZOMETERS (SHT, SLT), THE HEXAGRAMS INDICATE THE ADVs AND THE SQUARES SHOW THE LOCATION OF DIPWELLS FOR MANUAL GROUNDWATER MEASUREMENT..... 111

FIGURE 6.2 VARIATION OF TIDE, SIGNIFICANT WAVE HEIGHT AND WAVE SET-UP ON 18TH AND 19TH OF SEPTEMBER 2013. 112

FIGURE 6.3 SCHEMATIC FIGURE OF NODES USED IN THE 1D AND 2D NUMERICAL MODEL (UPPER AND LOWER PANELS, RESPECTIVELY). THE GREEN LINE/AREA SHOWS THE INITIAL CONDITION OF THE NUMERICAL MODEL. RIGHT AND LEFT BLUE LINES/PARALLELOGRAMS SHOW THE UPPER AND LOWER BOUNDARY CONDITIONS RESPECTIVELY..... 117

FIGURE 6.4 SENSITIVITY OF THE LINEAR MODEL (A) AND NON-LINEAR MODEL (B) TO TIME INTERVAL. 119

FIGURE 6.5 SENSITIVITY OF THE LINEAR MODEL (A) AND NON-LINEAR MODEL (B) TO BEACH HYDRAULIC CONDUCTIVITY. 121

FIGURE 6.6 SENSITIVITY OF THE LINEAR MODEL (A) AND NON-LINEAR MODEL (B) TO INLAND GROUNDWATER TABLE. 123

FIGURE 6.7 SENSITIVITY OF THE LINEAR MODEL (A) AND NON-LINEAR MODEL (B) TO WAVE SET-UP..... 125

FIGURE 6.8 LINEAR MODEL GROUNDWATER EXIT POINT ELEVATION (RED LINE), VARIATION OF THE SHORELINE ELEVATION (BLUE LINE) AND SURVEYED GROUNDWATER SEEPAGE LINE (BLACK SQUARES) IN TRANSECT 1 (A), TRANSECT 2 (B) AND TRANSECT 3 (C) 128

FIGURE 6.9 NON-LINEAR MODEL GROUNDWATER EXIT POINT ELEVATION (RED LINE), VARIATION OF THE SHORELINE ELEVATION (BLUE LINE) AND SURVEYED GROUNDWATER SEEPAGE LINE (BLACK SQUARES) IN TRANSECT 1 (A), TRANSECT 2 (B) AND TRANSECT 3 (C) 128

FIGURE 6.10 GROUNDWATER SEEPAGE FACE WIDTH VARIATION CALCULATED FROM LINEAR BOUSSINESQ EQUATION IN TRANSECT 1 (B), TRANSECT 2 (C) AND TRANSECT 3 (D) 129

FIGURE 6.11 GROUNDWATER SEEPAGE FACE WIDTH VARIATION CALCULATED FROM NON-LINEAR BOUSSINESQ EQUATION IN TRANSECT 1 (B), TRANSECT 2 (C) AND TRANSECT 3 (D) 129

FIGURE 6.12 COMPARISON BETWEEN THE SURVEYED GROUNDWATER SEEPAGE LINE (SOLID LINE) AND LINEAR MODEL RESULTS (DOTS). PANEL A: FIRST DAY (18TH SEPTEMBER 2013), PANEL B: SECOND DAY (19TH SEPTEMBER 2013)..... 130

FIGURE 6.13 COMPARISON BETWEEN THE SURVEYED GROUNDWATER SEEPAGE LINE (SOLID LINE) AND NON-LINEAR MODEL RESULTS (DOTS). PANEL A: FIRST DAY (18TH SEPTEMBER 2013), PANEL B: SECOND DAY (19TH SEPTEMBER 2013)..... 131

FIGURE 6.14 VARIATION OF THE “AVERAGE OF THE GROUNDWATER SURFACE, CALCULATED BY THE NUMERICAL MODEL” WITH TIDE 133

FIGURE 6.15 DECOUPLING BETWEEN THE GROUNDWATER SEEPAGE LINE (GREEN DOTS, CALCULATED FROM LINEAR MODEL) AND THE SHORELINE (BLUE LINE) AT HIGH TIDE (A), LOW TIDE (B), HIGH TIDE (C) ON 18TH AND AT HIGH TIDE (D), LOW TIDE (E) ON 19TH SEPTEMBER 135

FIGURE 6.16 DECOUPLING BETWEEN THE GROUNDWATER SEEPAGE LINE (GREEN DOTS, CALCULATED FROM NON-LINEAR MODEL) AND THE SHORELINE (BLUE LINE) AT HIGH TIDE (A), LOW TIDE (B), HIGH TIDE (C) ON 18TH AND AT HIGH TIDE (D), LOW TIDE (E) ON 19TH SEPTEMBER 2013 135

FIGURE 6.17 VARIATION OF THE GROUNDWATER EXIT POINT ELEVATION (PANELS A, B) AND EXTENT OF THE SEEPAGE FACE WITH THE TIDE (PANELS C, D, E, F) ALONG TWO DIFFERENT BEACH TRANSECTS (RED INDICATES TRANSECT 1 AND BLUE INDICATES TRANSECT 3). LEFT PANELS SHOW LINEAR MODEL RESULTS AND RIGHT PANELS SHOW NON-LINEAR MODEL RESULTS..... 137

FIGURE 7.1 POTENTIAL BEACH MORPHOLOGICAL FEEDBACK LOOP (PANEL A) AND SURFZONE MORPHODYNAMICS FEEDBACK LOOP (PANEL B) 148

List of Symbols

ADV: Acoustic Doppler Velocimeter

a_i : Regression coefficients

D: Averaged-aquifer thickness

d_m : Mean grain size

d_{10} : Grain diameter for which 10% of the sample are finer

El_2 : Beach surface elevation

El_1 : Elevation of top of the tube

FTCS: Forward time, central space scheme in a numerical model

g: Gravity acceleration

GW_{El}: Groundwater elevation

GWEP: Groundwater exit point

GWSL: Groundwater seepage line

GW: Groundwater

H_{rms} : Root mean-square wave height

H_S : Significant wave height

HSV: Hue-Saturation-Value-space image

h_b : Breaking wave height

$h_{i,j}^t$: Groundwater elevation in node $[i, j]$ at time step of t

$h_{i,j}^{t+1}$: Groundwater elevation in node $[i, j]$ at the next time step ($t + 1$)

$h_{i,j+1}^t, h_{i,j-1}^t, h_{i+1,j}^t$ and $h_{i-1,j}^t$: Groundwater elevation in adjacent nodes at time step of t

I: Intensity in a RGB image

K: Hydraulic conductivity

n: Sediment porosity

$o(\Delta t)$, $o(\Delta x^2)$ and $o(\Delta y^2)$: computational errors in the numerical model.

PDE: Partial Differential Equation

P: Pressure

PSD: Power Spectral Density

PI: Pixel intensity

RGB: Red-Green-Blue image

S-U: Wave set-up

S: Beachface slope

SL: Shoreline

SF: Groundwater seepage face

SHT, and *SLT*: High tide and low tide Solinst piezometers

SM: Surfzone morphology parameter

Sy: Specific yield

TR: Tide elevation

t: Time.

U_w: wave-induced velocity in alongshore directions

V_w: wave-induced velocity in cross shore direction

V: Value in a HSV image

V_o: Intertidal beachface volume

WT: Inland groundwater table

X₂: Barometric pressure

X₁: Piezometer data

x : Horizontal cross-shore distance

y : Horizontal alongshore distance

Δx : Local distance between adjacent nodes in cross-shore space

Δy : Local distance between adjacent nodes in alongshore space

Δt : Time difference between adjacent time steps

\emptyset : Standard deviation

μ : Dynamic viscosity

ν : Kinematic viscosity

γ : Wave breaking coefficient

η_{set-up} : Wave set-up height.

ρ : Density

λ : Courant number

Chapter 1 : Introduction

1.1 Thesis topic and its significance

Coastal erosion is one of the most common problems at many beaches. It is caused by both natural factors and human activities. Sea level rise, climate changes such as changes in precipitation and temperature regimes, extreme wave and storm surge conditions, tidal currents, subsidence and coastal flooding could cause changes in the groundwater level and consequently the beachface erosion pattern. Human interventions including woodland establishment, urbanization, damage to sand dunes and removal of coastal plants also increase the beach erosion rate (e.g. Masterson and Garabedian, 2007; Holman, 2006). There are two common types of coastal erosion. Firstly, there is short-term (e.g. weeks to decades) erosion that is caused by storms. In this case, the position of the shoreline is not changed permanently, although the full beach erosion and recovery cycle may last several decades. Secondly, there is long-term erosion caused by factors such as sea-level rise. In this type of erosion the shoreline position is changed. Global warming could cause sea level rise and consequently cause a long-term increase to coastal erosion. A global sea level rise of 0.2 to 0.25 m has been recorded over the last century, while it has risen almost 0.3 m over the last 300 years. The International Panel on Climate Change estimates that the global average sea level will rise between 0.4 and 0.8 m in the next century (IPCC, 2015).

The elevation of the water table in relation to the average sea level changes with tide and waves, causing infiltration and exfiltration of water into the beach, which has a consequence to sediment transport (Li et al., 1999). The water table variation in a beach can influence swash sediment transport and as a result deposition or erosion across the beach will occur (Turner, 1995). In other words, the location of zones of erosion and deposition is established by tidal movement of the sea-level and the seepage line across the beachface. For instance, below the effluent line, the beachface is saturated and erodible while it is unsaturated and more likely to be a zone of deposition above the line (Eliot and Clarke, 1988).

1.2 Thesis aims and objectives

The general aim of this thesis is to study the variation of the groundwater seepage line on gently-sloping dissipative beaches using field survey data, video images and numerical models. There are some experiments and mathematical models to simulate beach groundwater variations (e.g. Parlange et al., 1984; Turner, 1993; Nielsen, 1990; Turner and Nielsen, 1997; Turner et al., 1997; Li et al., 1997; Turner, 1998; Baird et al., 1998; Li et al., 1999; Raubenheimer et al., 1999; Li et al., 2000; Li et al., 2002; Li and Jiao, 2003; Jeng et al., 2005; Li et al., 2006; Song et al., 2007; Li et al., 2008; Guo et al., 2010). Many of these studies have focused on wave run-up and tide induced changes to the groundwater. However, some of these numerical models have limitations in their theories and applications, including limitation of the numerical computation, data requirements, boundary conditions, model assumptions and uncertainty of the simulation results. The non-heterogeneous character of the aquifer, which has often been ignored in models, is another problem (Xiu-yuan et al., 2009).

Although the relationship between groundwater table and beach volume has been studied previously (e.g. Grant, 1948; Eliot and Clarke, 1988; Turner and Leatherman, 1997), there are few studies on high energy gently-sloping dissipative beaches. The location of the groundwater seepage line could be a function of a range of factors such as sediment porosity and hydraulic conductivity, beach morphology, beachface slope, wave set-up, tide variations, water infiltration and exfiltration into or from the beachface, the inland water table and local rainfall. Changes in these parameters cause water table variation and consequently beachface volume changes.

This study will test following questions:

- ✚ What is the relationship between the observed groundwater seepage line and the intertidal beach volume and can this effect be separated from the influence of the rip currents?

✚ What is the best statistical model which can describe the role of the groundwater seepage line and surfzone morphology in changing beachface volume? What is the accuracy of this statistical method?

✚ How well can video images be used for extracting the groundwater seepage line and shoreline at a dissipative meso-tidal beach? What is the accuracy of this technique in comparison with surveying data?

✚ How does the groundwater seepage line on a dissipative meso-tidal beach change over a tidal cycle? How can video images be used to observe the decoupling of the groundwater seepage line from the shoreline?

✚ What are the main parameters controlling the groundwater seepage line on a dissipative meso-tidal beach? Which driver (intertidal beach geometry, beach sediment porosity and hydraulic conductivity, tide variation, inland water table, rip currents and wave set-up) is the most important in explaining changes to the seepage line?

✚ Can numerical models (both linear and non-linear) based on the Boussinesq equation accurately predict the tidal groundwater changes across the beachface and determine the position of the groundwater exit point? Can the numerical model results show the decoupling between the groundwater seepage line and the shoreline?

1.3 Beach field sites

Two sites on the west coast of the New Zealand's north island were studied in this research. First Muriwai beach was selected to study the correlation between the groundwater seepage line, rip current locations (characterised by video image pixel intensity) and the intertidal beachface volume. Muriwai is a meso-tidal gently-sloping beach located on the west coast, approximately 35 km west of Auckland and 48 km south of Kaipara Harbour entrance. The west coast has significant wave heights of between 1 and 3 m and the average wave period of 6-8 s (Gorman et al., 2003). The mean spring tidal range at Muriwai is about 3 m (Bryan et al., 2007). The surf zone is 400-500 m wide on average and includes an inner bar and more gently-sloping outer bars; however during high energy storms, the surf zone width may be greater than 800 m. The beachface has an average slope of 1:100 and generally consists of fine sands with the mean diameter of 0.25 mm (Brander and Short, 2000). A one-dimensional linear Boussinesq equation was also used to study the movement of the groundwater exit point across the beachface transects. The effect of inland water table, beach slope, beach sediment hydraulic conductivity, tidal range and wave set-up on the groundwater exit point was discovered. The model was run based on the field data collected by Robinson (2004). The lack of the field data including updated beach survey, sediment properties, and video images resulted in a switch in the study area from Muriwai to Ngarunui beach for the remainder of the thesis. Ngarunui beach is also a dissipative beach located near Raglan on the west coast. The beach is approximately 1.8 km length, in almost 4 km south-west of Raglan city. There is a steep dune (~1:5) in the east of the beach. At the north, the beach turns into Raglan Estuary (Morris et al., 2007). Ngarunui is a black sandy beach with an average grain size of 0.31 mm (Laurent, 2000). The beach slope is approximately 1:70 (Huisman et al., 2011). The spring tide ranged between 2 and 3 m and neap tide is 1.5-1.8 m (Walters et al., 2001). The groundwater seepage face, which generally appears between the shoreline and the groundwater seepage line during the retreating tide, is clearly exposed as a glassy surface, and so could be obtained using standard surveying techniques and video images.

1.4 Thesis structure

Regarding aims and objectives of the research , this thesis is mainly focused on A) understanding the beachface variation associated with the groundwater table and determining the correlation between the groundwater seepage line, rip current and beachface volume on a gently-sloping dissipative beach “Chapter 3”; B) extracting the shoreline and the seepage line from video images and study the process of decoupling of the shoreline from the groundwater seepage line during a tidal cycle “Chapter 4”; C) a field experiment on a gently-sloping beach to measure the long-term groundwater table changes, short-term variation of the beach groundwater level and wave data “Chapter 5”; D) using a two dimensional numerical model based on the Boussinesq equation to study changes in the groundwater exit point across the beachface, variation of the groundwater seepage line along the beach, and determining the role of the onshore characters and offshore factors which affect the groundwater seepage line variations “Chapter 6”. The results of this research could be generalized to other coasts that experience dissipative conditions.

Chapter 2 : Literature Review

2.1 Beach groundwater and erosion

As coastal groundwater is one of the most significant issues affecting beach volume and coastal erosion; hence, understanding the relation between the beach groundwater table and beachface erosion and accretion has been a focus of coastal engineers for a wide range of research purposes and practical applications (e.g. Grant, 1948; Duncan, 1964; Eliot and Clarke, 1986; Turner, 1993; Turner and Leatherman, 1997; Turner 1998; Huisman et al., 2011). Field studies have shown that the elevation of the beach groundwater fluctuates with tidal cycle, waves, and weather patterns (e.g. Duncan, 1964; Eliot and Clark, 1986; Hegge and Masselink, 1991; Nielsen, 1999; Horn, 2006). Nielsen (1999) mentioned that the groundwater overheight depends on the wave amplitude, tide range and the beachface slope. For example, several metres super-elevation of the groundwater is observed when large waves or tides occur on a flat sandy beach. As shown in Figure 2.1 the groundwater table increases landward of the shoreline. At high tide, this rise is because of the infiltration from waves. This procedure changes the shape of the water table to a humped-shape with the maximum near the run-up limit. The water table fluctuates between $UENV$ and $LENV$ (upper and lower boundaries of water table fluctuation). The difference between the elevation of the intersection of $UENV$ and $LENV$, and MSL (Mean Sea level) is used to determine the average super-elevation of the groundwater (η^+) (Nielsen, 1999). Turner et al. (1997) also showed that wave run-up, variation in tide and rainfall cause a super-elevation of the groundwater table above the tide elevation.

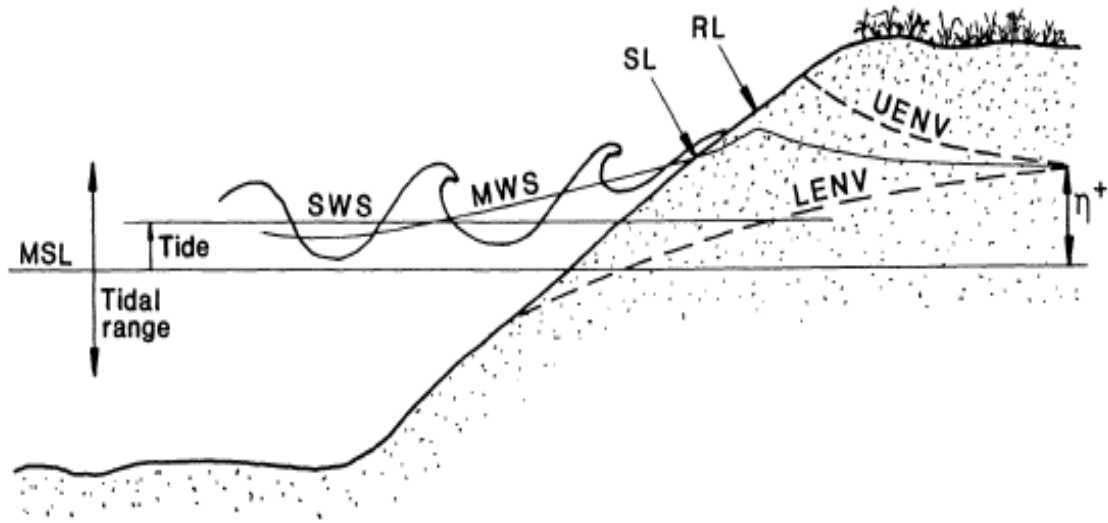


Figure 2.1 Parameters used in formulating the coastal boundary condition for groundwater modeling. SWS (Still Water Surface): the smooth sea surface without considering waves that fluctuates with changes in atmospheric pressure and tides; MWS (Mean Water Surface): the local short time averaging of the water elevation, and is averaged over the scale of individual waves; SL: the shoreline position and RL is run-up limit. (Nielsen, 1999)

Besides offshore factors, groundwater location and its movement are generally related to the geology and soils comprising the coastal zone. Groundwater can be located within several feet of the ground surface or deeper within sandy beaches. Basically, there are three approaches for monitoring the groundwater elevations and flow in a sandy coastal aquifers: A) measurements of the hydraulic head using piezometers to determine vertical and horizontal flows through the aquifer; B) measurements of the local water table elevations using data collected from monitoring wells (Turner, 1998); C) the extend of the seepage face, which exposes across the beachface and groundwater seepage line that outcrops the beach (Figure 2.2).



Figure 2.2 A Snap-shot of swash and groundwater seepage line at Raglan beach. Groundwater seepage face appears as a shiny area between seepage line and shoreline. (Huisman et al., 2011).

Groundwater studies at coastal zones showed that, in practical applications, landward of the swash zone the water table is approximately horizontal and shore-normal. The assumption of one-dimensional flow equates the phreatic surface - the location where the pore water pressure is under atmospheric conditions - to the water levels monitored in each piezometer using equations by Dupuit (1863) and Forchheimer (1930).

On high tide, the infiltration of seawater to the coastal aquifer causes the water table to rise. During the descending tide, if the beach drains more slowly than the tide falls, the groundwater seepage face (Figure 2.3) will appear between the shoreline (SL) and the groundwater seepage line ($GWSL$) because of the groundwater exfiltration (Turner, 1993). The seepage face is a dynamic area between the shoreline and the intersection of the water table and the beachface (Turner, 1995). The

intersection of the seepage line and the cross-shore profile indicates the groundwater exit point that differentiates the upper unsaturated zone from the lower saturated land part. Monitoring of the groundwater seepage line has been done on a number of beaches in order to understand the role that groundwater seepage might play in controlling beach dynamics. For example, Turner (1998) determined the dynamics of the exit point, where the groundwater table crosses the beachface, using linear interpolation between piezometers and observed data from different beaches over a tidal cycle. The dynamics of the groundwater exit point on the beachface specifies the time-varying area of the saturated and unsaturated parts in the intertidal zone. The elevation of the groundwater exit point specifies a boundary between two different intertidal areas (upper and lower regions), before over-topping by the rising tide (Turner, 1995). The seepage face parameter was applied by Turner (1993, 1995) to illustrate the sensitivity of the coastal seepage face development to tide, beach profile and sediment characteristic (Figure 2.4). Turner (1993) indicated that the seepage face is a function of the profile slope and permeability characteristics (such as soil porosity).

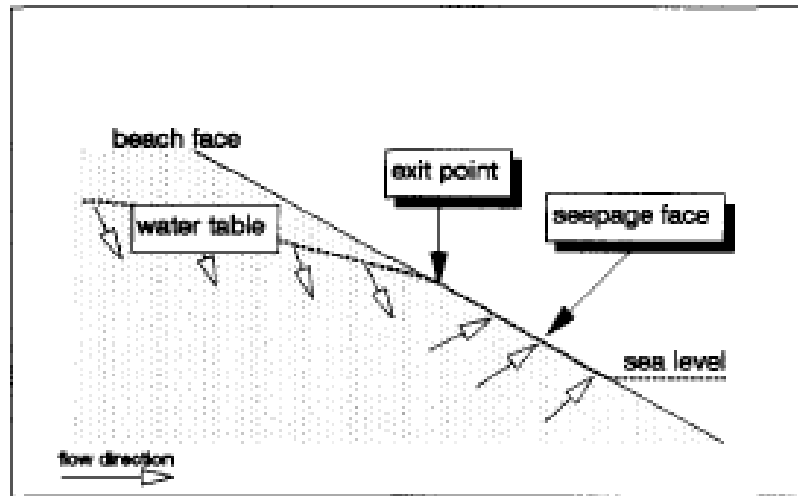


Figure 2.3 The sketch of the seepage face and definition of the exit point (Turner, 1993)

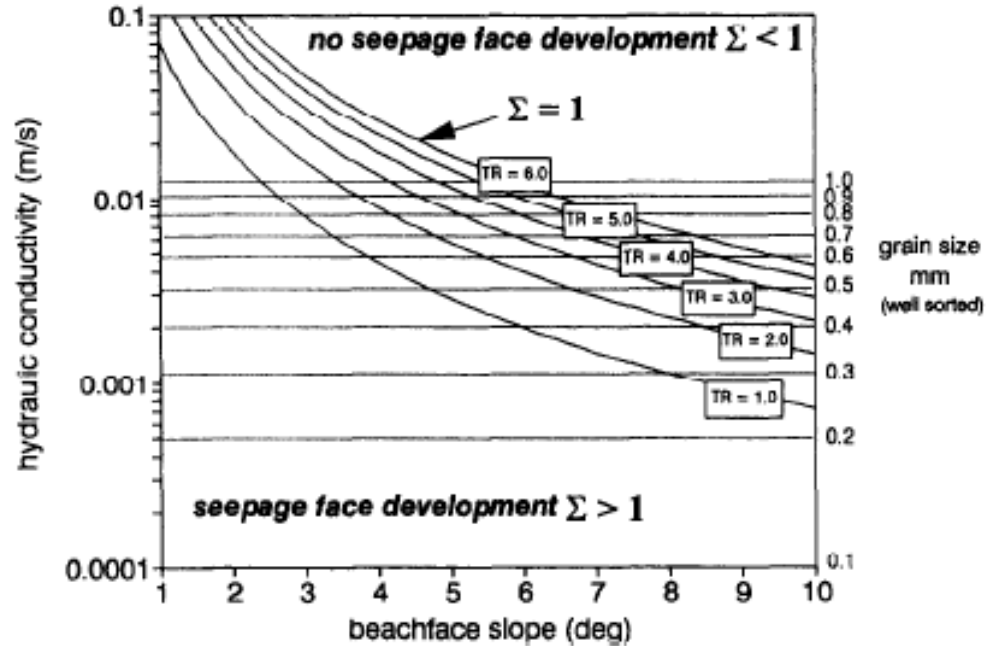


Figure 2.4 Seepage face parameter as a function of tide range (TR), hydraulic conductivity and beachface slope (Turner, 1995)

The development and motion of the seepage face has been modeled using only the ascending and descending tide and beach permeability; however pressure distribution within the beach are often neglected in early work. For example, the point of outcropping (exit point) and the movement of the seepage face across the intertidal profile and consequently the extent of the saturated and unsaturated regions of the intertidal zone were simulated by Turner (1993) using the “SEEP” Model (Turner, 1993 and 1995). Applying the SEEP model showed that even small changes in the beachface slope and permeability characteristics cause large changes in exit point location (Turner, 1993), and the exit point fall increases when soil permeability and beach slope are increased. After Turner (1993 and 1995), the movement of the groundwater exit point along the seepage line, and the separation between the wet-dry boundary and the tide (or the mean position of the swash) have been largely simulated by more complex models, which include pressure gradients (Li et al., 1997; Baird et al., 1998; Li and Barry, 2000; Li et al., 2000, 2002; Huisman et al., 2011) (e.g. Figures 2.5, 2.6 and 2.7).

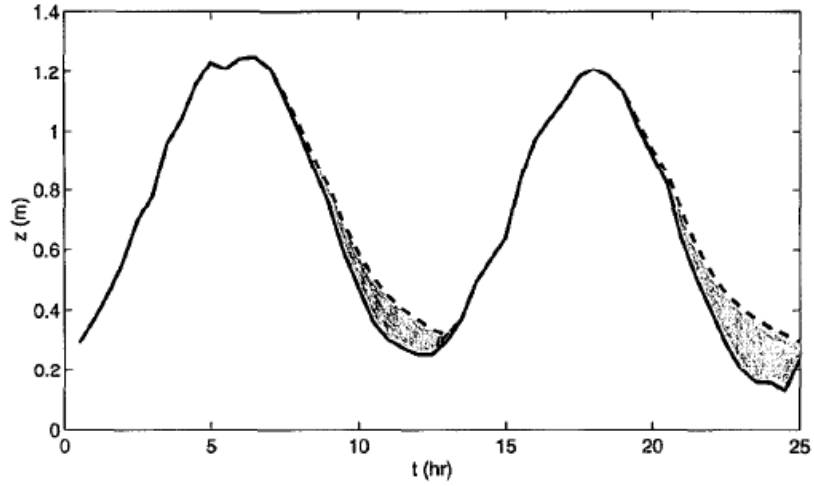


Figure 2.5 Decoupling between the tide (solid line) and groundwater exit point (dashes); and formation of the seepage face (Li et al., 1997).

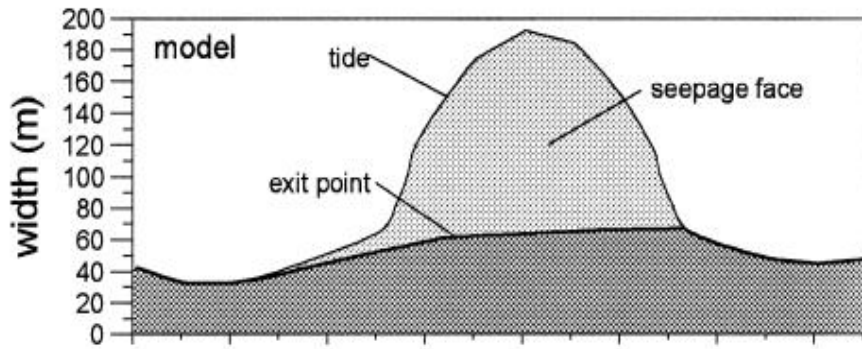


Figure 2.6 Seepage face extent across the intertidal profile (Turner, 1998).

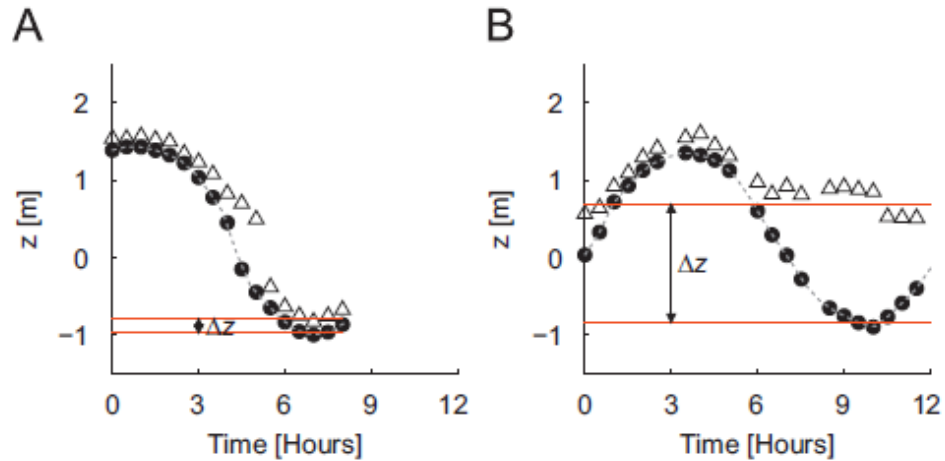


Figure 2.7 Decoupling between the shoreline (circles) and seepage line (triangles); A: the difference between the seepage line and shoreline is similar at low tide and high tide. B: the difference is much larger at low tide than high tide. (Huisman et al., 2011).

Huisman et al., (2011) indicated that there were 6 days where the difference in elevation between the wet–dry boundary and the shoreline remained constant. The difference (Δz in Figure 2.7A) is equal to the difference between the run-up maxima and the shoreline elevation. In this case when a coupled groundwater seepage line (GWSL) developed, the wet–dry boundary is related to the upper swash limit. Reversely, during the other 8 days of their experiment, the wet–dry boundary and the shoreline decoupled (Figure 2.7B). They described that in these days Δz is more related to the beach watertable rather than run-up at low tide.

There is a strong empirical relationship between the water table elevation and foreshore erosion and slope (Harrison, 1969), and maximum degradation occurs when the beachface is saturated (Eliot and Clarke, 1988). Many field and laboratory experiments have indicated that a high beach groundwater table promotes beach erosion and the low water table enhances beach accretion (e.g. Grant, 1948; Baird and Horn, 1996; Turner and Leatherman, 1997; Li et al., 2002) (Figure 2.8).

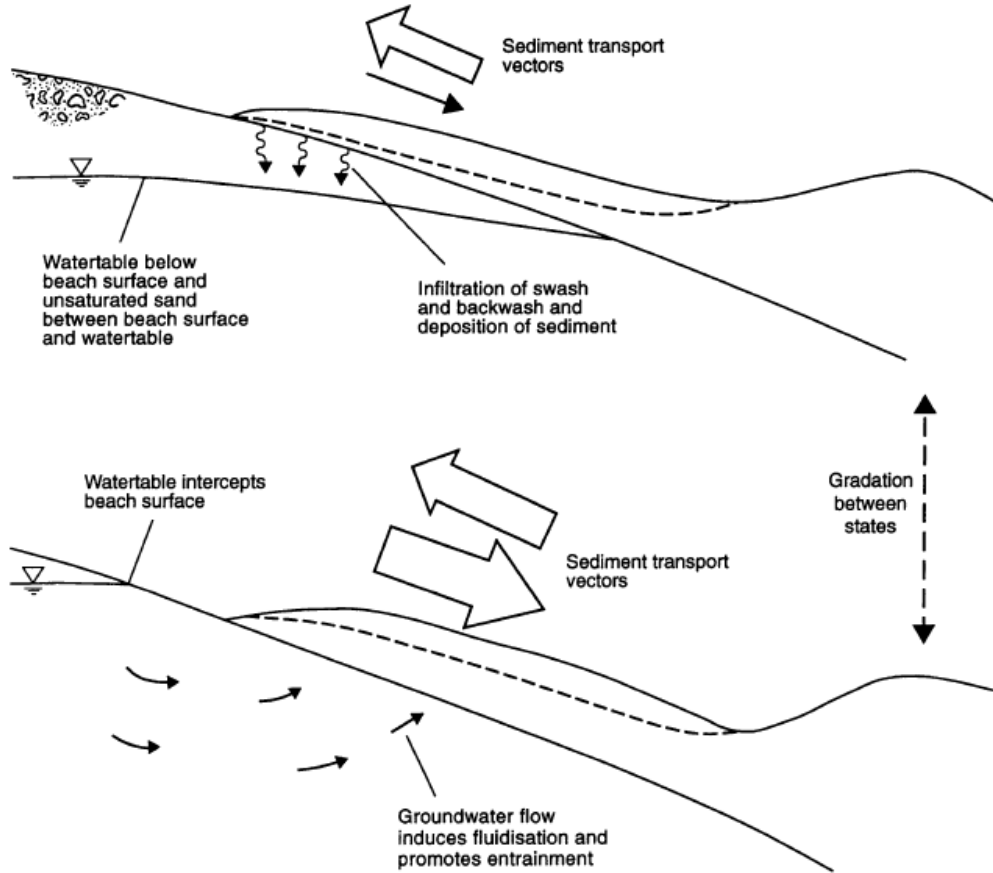


Figure 2.8 Conceptual model of the relationship between beach groundwater and sediment transport in the swash zone (after Grant 1948; Baird and Horn, 1996).

Groundwater seeping from the beachface can induce lower beachface volume (e.g. Grant, 1948; Duncan, 1964; Harrison, 1969; Eliot and Clarke, 1986; Baird and Horn, 1996; Turner and Leatherman, 1997; Li et al., 2002), and so may play a role in controlling the development of the beach morphology, beachface dynamics, and, consequently, the stability of the coastline (e.g. Hegge and Masselink, 1991). Higher water tables influence swash sediment transport by causing saturation and enhanced entrainment and subsequently, lower beachface volume (Grant, 1948; Duncan, 1964; Eliot and Clarke, 1988; Turner, 1995). Thus, there is a negative correlation between the water table elevation and beachface volume, in which beachface volume decreases with increase in groundwater elevation (e.g. Duncan, 1964; Turner and Leatherman, 1997). The beach water table can change not only due to variations in

the inland water table, but also when the sea level rises causing infiltration of seawater into the beachface.

The relationship between the beach groundwater table and beach profile changes has been demonstrated in numerous field investigations (e.g. Duncan, 1964; Eliot and Clarke, 1986, 1988; Turner, 1993; Turner and Leatherman, 1997; Li et al., 2002). Duncan (1964) studied the cyclic beach cut and fill patterns in foreshore beach profile during a single semi-durnal tidal cycle on the gently-sloping Manhattan Beach, California. He attributed some of the variations to the interaction between the location of the swash zone and the groundwater out-cropping. Harrison (1969) built on this earlier study by empirically showing that the ratio of the hydraulic head of the groundwater to the swash run-up may explain the changes in foreshore morphology during the falling tide.

It can be concluded that there is a negative correlation between the seepage line elevation and the beachface volume, which means beachface volume is reduced with increases in the groundwater table elevation. Further, swash and beach groundwater causes beach erosion in saturated beachface (e.g. Eliot and Clarke, 1988; Grant, 1948; Turner, 1993, 1995). In fact, the elevation of the beach groundwater is an important factor affecting beachface dynamics and changing the coastline stability (Hegge and Masselink, 1991). On the other hand, changes in the beachface volume can also alter the groundwater table as a consequence of changes to the sediment characteristics. The soil properties change during time and vary the rate of infiltration from the sea (Holman, 2006). This feedback process can be an important issue in groundwater modelling.

2.2 Video techniques

Relating beach erosion to groundwater table dynamics requires robust measurements of changes in the foreshore slope over morphologically-relevant time scales. Monitoring foreshore changes through time has been considered by coastal engineers both for research purpose and practical applications. As observation of beach variation using surveyed profiles is a time-consuming and expensive approach, measurement of the past shoreline changes are often carried out using aerial photographs. One of the cheapest and automated approaches for beach observation is video imagery (Smith and Bryan, 2007). Although new surveying systems such as kinematic GPS, or LIDAR scanners, can be used for quick data collection in the field, such video-based techniques have provided the ability to automatically collect data. High resolution images in space and time are two of the most important characteristics of this system for coastal management (Koningsveld et al., 2007). As optical remote sensing techniques have presented cost efficient and long-term data with minimum operational difficulties (Holman and Stanley, 2007), these techniques have become an effective alternative to classical surveying approaches. The coastal video system that was first presented as the ARGUS programme has been developed over two decades by the Coastal Imaging Lab (CIL) at Oregon State University (OSU; <http://www.coas.oregonstate.edu/>) (Holman and Stanley, 2007; Aarninkhof et al., 2003). The main purpose of this programme was to develop approaches for low-cost long-term optical measurements, using Argus Stations. In recent years, the Argus Programme has facilitated obtaining large number of geophysical parameters from image data including, coastal morphology, surface currents and wave parameters.

The ARGUS and Cam-Era video systems are two of optical video techniques that help us with monitoring coastal morphology and morphodynamics using high resolution images during long term periods. Every hour (for ARGUS) or every half-hour (for Cam-Era) during daylight conditions, an on-site computer collects a snapshot image, an average image and a variance image, which described as follow. Among different types of video-images, time exposure images have been largely used

for discovering morphological patterns (Lippmann and Holman, 1989; Holman and Stanley, 2007).

- Single Snapshot image: at the beginning of each hour the camera takes a single snapshot image to record the beach conditions and also produce an image that could be used in explaining other collected data.
- Time-averaged (Timex or time-exposure) images: these images are the most important images in video systems that are collected hourly or every half-hour (in ARGUS and Cam-Era, respectively). Although, Timex images do not have visual points and marks associated with individual waves, each image shows the time-mean of all of the frames, which taken of 2 Hz during 10-minute period of the procedure (Holman and Stanley, 2007). The images obtained during low tide indicate the intertidal morphology (bars, troughs and rips).
- Variance images: variance images are collected based on the same 10-minute period of sampling as Timex images. The difference between these two types of images is that variance images are produced from the standard deviation of 10-minute period image intensities, while time-averaged images are the time-mean of image intensities. Variance images show the areas of greatest change, and are mainly used to define the surfzone and the area, which waves break. The surfzone is shown as a bright area, because of the waves breaking, while the dark part in a variance image shows the sandy beach, which does not change over the 10-minute interval (Holman and Stanley, 2007).

In the spatial domain, the nearshore is an area where wave characteristics change over several hundred metres as the waves shoal, break, disperse across a surf zone, and reflect from the shore in the swash zone. In the first 100 m from the beach, rip currents usually cause strong variations (Holman and Stanley, 2007). Bathymetry changes greatly over tens to hundreds of metres. In this area sand bars occur in very complex forms (Lippmann and Holman, 1990). Morphodynamics of the nearshore system, which is the response of nearshore to the overlying waves and currents, represents the time-averaged quasi-equilibrium of the forcing and responses, and should be quantified to understand the beach behaviour. Time intervals used for

sampling (e.g. taking each of the photos in the video sequence) are very important. The periods of wind waves and swell is 10s, so sampling must be considered at several samples per second (Holman and Stanley, 2007). Tide causes fluctuations of surfzone characteristics with approximately 12-hour periods. Bathymetry variations at the shoreline can happen in hours; and storms can affect sand bars in one day (Sallenger et al., 1985; Holman and Stanley, 2007).

Optical techniques allow us to see features because of the variations in the reflection coefficient of water with sea surface slope, such as the length, direction and period of waves (Holman and Stanley, 2007). Fluctuations in wave breaking, which cause wave foam are also easily identified in the images. Wave breaking is one of the most important drivers of the dynamics of nearshore wave and current (e.g. Lippmann et al., 1997). In addition, zones of concentrated wave breaking show the location of the submerged sand bars (Lippmann and Holman, 1989). Video-based techniques have been used for: measurement of the sediment transport (Drake et al., 1988); measurement of the wave run up (Holland et al., 1995; Holland and Holman, 1993); the location of the shoreline and sand bars (Lippmann and Holman, 1989, 1990); beach profiles (Holman et al., 1991); determination of the intertidal beach elevations over the alongshore during a specified period (Plant and Holman, 1997); estimation of the operation of coastal protection structures (Aarninkhof, et al., 2003); extracting the wet-dry boundary across the beachface (Huisman et al., 2011) and mapping beach bathymetry (Uunk et al., 2010).

Among mentioned application of video images in coastal sciences, determining the position of the rip currents and extracting the shoreline and groundwater seepage line were studied as part of this thesis:

➤ There is a correlation between the white narrow part of time-averaged images and the location of the submerged sand bar crests. This relationship was firstly presented by Lippman and Holman (1989). In time-averaged images areas with low intensity, which appear as black, show rip currents. Sand bars are often cut by cross-shore rip channels (Holman and Stanley, 2007) and appear as white in the time-averaged

images. Hence, this type of images can be used to determine the morphology and the location of the nearshore sand bars and rip currents (Lippmann and Holman, 1989).

➤ Shoreline could be determined as the bright narrow part of the shore break, and it could be defined using time-averaged video images. This technique is based on the difference between the colour and contrast of the dry and wet sand (Plant and Holman, 1997; Aarninkhof et al., 2003). The shoreline could be also extracted from timestack images (Huisman et al., 2011). As shoreline mapping needs only a few image frames provided by a specific camera location, shoreline mapping has become one of the most practical approaches among other methods (Plant et al., 2007). There are several different approaches to the shoreline mapping method using images received from one specific camera. Some shoreline discovering methods are as follows:

- Shore Line Intensity Maximum (SLIM Model) (Plant and Holman, 1997): In this method, a superposition of Quadratic and Gaussian-shaped functions was fitted to the intensities along a cross-shore transect that included the entire intertidal zone; therefore, SLIM positions were located with corresponding uncertainty distributions. At regions with steep slope of the intertidal beach and narrow intertidal zone; clear swash zone shows that SLIM method could be a good factor for describing the actual shoreline (Plant et al., 2007). On the other hand, as this algorithm determines the shoreline based on the existence of the narrow bright part relative to the shore break that does not exist in dissipative beaches (Aarninkhof et al., 2003; Plant et al., 2007), the application of this model will be limited to non-dissipative beaches.
- Pixel Intensity Clustering (PIC Model) (Aarninkhof et al., 2003; Plant et al., 2007): As the SLIM method commonly had inaccurate results for more dissipative coastlines with gentle beach slope, the PIC Model was developed. In this method, the difference in colour between the dry and wet sand is considered. In the first step, values in the red, green, and blue (*RGB*) channels are converted into hue, saturation, and intensity values (*HSV*) (Plant et al, 2007). *HSV-space* is more sensitive for this application rather than *RGB-space*, because colour information (*H* and *S*) is separated from gray

scale intensity and luminance information (Huisman et al., 2011). In the next step, a *HS* histogram of the hue and saturation or intensity is used to specify the shoreline. In the *HS* histogram, pixels related to the water are largely distinguished from ones corresponding to the dry land. By this way, the shoreline location could be specified as a line where a discriminator function is equal to zero (Plant et al., 2007). It should be noted that the earlier SLIM method that was based on discovering the shoreline using *HSV* images can be only used when there is no groundwater seepage on the beach (Huisman et al., 2011).

- Colour Channel Divergence (CCD Model) (Plant et al., 2007; Smith and Bryan, 2007): The main assumption of this approach is that the comparative amount of the blue and red light on camera could differentiate the water part of the image from sand surface.

Figures 2.9, 2.10, 2.11 show some of the recent works on extracting shoreline from video images.

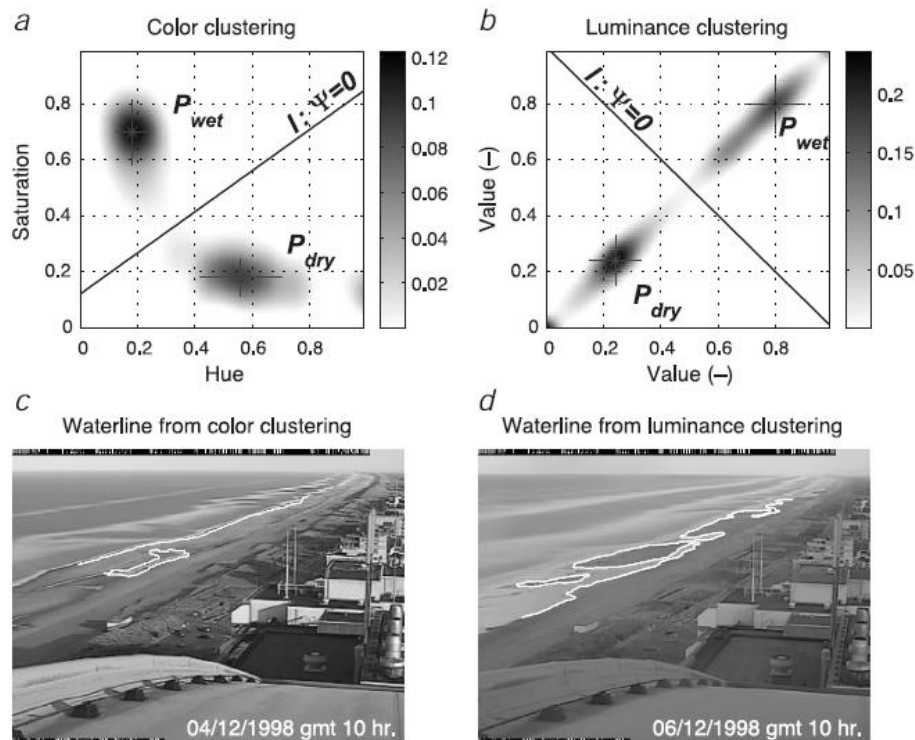


Figure 2.9 PIC detection method in extracting shoreline from video images (Aarninkhof et al., 2003).

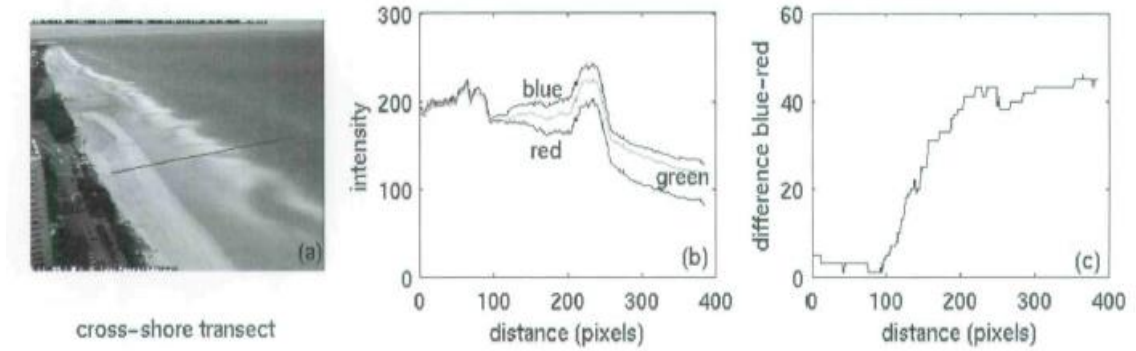


Figure 2.10 CCD method. The divergence of the red and blue intensity shows the shoreline location (Plant et al., 2007).

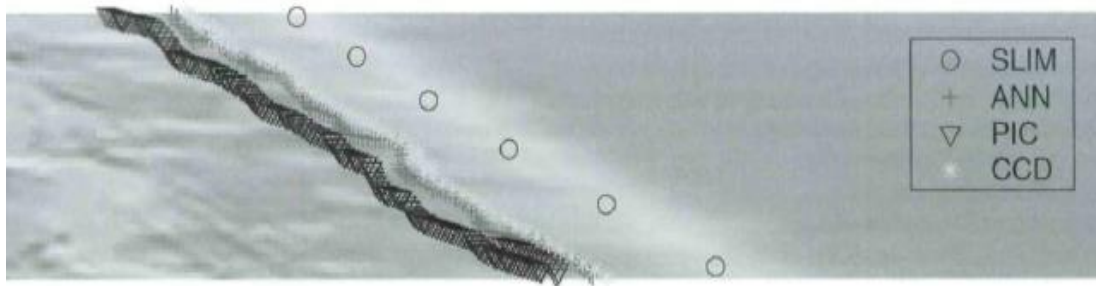


Figure 2.11 Comparison between different shoreline detecting methods (Plant et al., 2007).

➤ The groundwater seepage line could also be extracted from video images. The wet-dry boundary could be found using 10-minute time-averaged images. The research carried out by Huisman et al. (2011) showed that the wet-dry boundary is closely associated with the groundwater seepage line. They noted that in some days of beach observation using video imagery, the wet-dry boundary got separated from the actual shoreline during falling tide; and the wet-dry boundary shows the groundwater seepage line (GWSL) around the low tide time. On the other hand, groundwater seepage line was not obvious in video images when the elevation difference between the shoreline and wet-dry boundary stay the same during the tide cycle. In fact at high tide, the wet-dry boundary represents the upper limit of the swash zone and super-

elevation in this boundary above the shoreline is always because of the swash dynamics (Huisman et al., 2011) (Figures 2.7).

➤ Study the movement of the waterline on video images during a tidal cycle can be used to generate intertidal beach morphology maps. Even though video is generally only suitable for monitoring intertidal volumes, these volumes are well correlated with changes to the beachface volume (e.g. Figure 2.12). The effects of sand extraction, storms, sea level changes, and coastal protection works on beaches could be expressed by the volumetric beachface changes (e.g., Smith and Bryan, 2007).

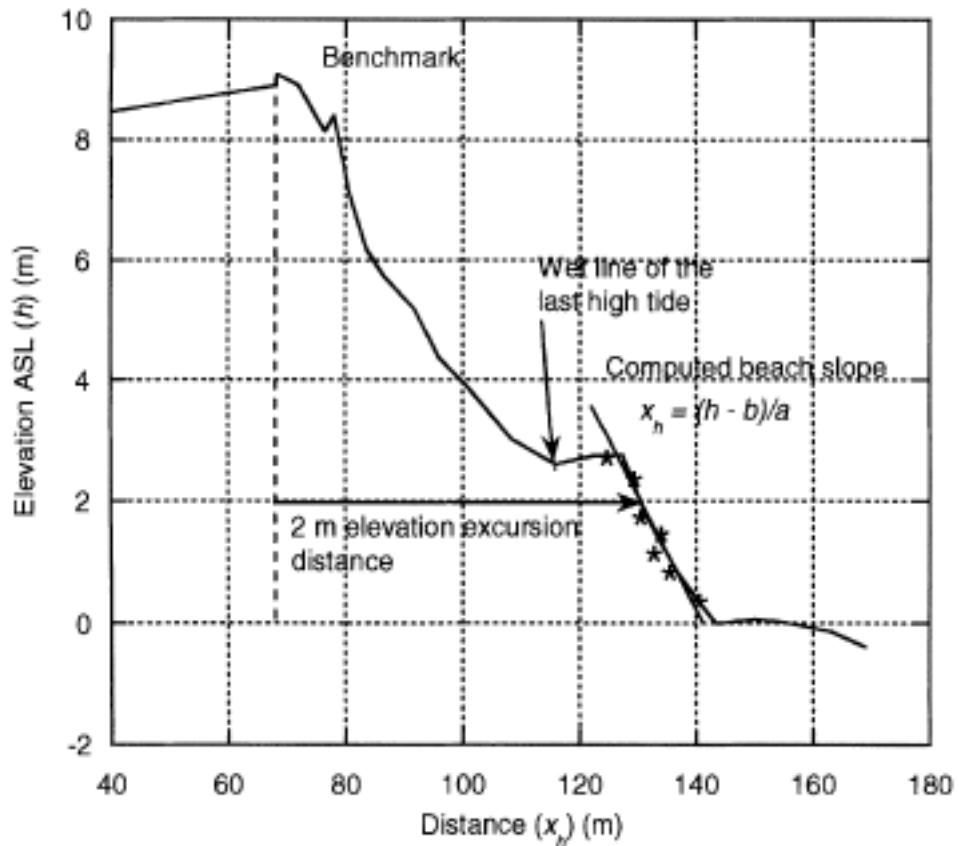


Figure 2.12 A schematic of the beach profile and best fit line of the intertidal profile determined from the hourly video images (Smith and Bryan, 2007).

To sum up, video imagery has become one of the most effective ways to study nearshore processes. Although the new video image technique shows good results for steep reflective regions, they tend to be less precise for flatter dissipative areas (Aarninkhof, et al., 2003). Therefore, there is a need to refine the technique for flat dissipative beaches. Furthermore, the acceptance of this new method could be increased by contrasting it with more conventional and accepted techniques and other data sources to show its advantages, reliability and accuracy (Koningsveld, et al., 2007).

**Chapter 3 : Groundwater Seepage and Surfzone
Morphology Control on Muriwai Beachface
Volume**

3.1 Introduction

As described before, groundwater seeping from the beachface can induce lower beachface volume (e.g. Grant, 1948; Duncan, 1964; Harrison, 1969; Eliot and Clarke, 1986; Baird and Horn, 1996; Turner and Leatherman, 1997; Li et al., 2002), and so may play a role in controlling the development of the beach morphology, beachface dynamics, and, consequently, the stability of the coastline (e.g. Hegge and Masselink, 1991). Higher water tables influence swash sediment transport by causing saturation and enhanced entrainment and subsequently, lower beachface volume (Grant, 1948; Duncan, 1964; Eliot and Clarke, 1988; Turner, 1995). Thus, there is a negative correlation between the water table elevation and beachface volume, in which beachface volume decreases with increase in groundwater elevation (e.g. Duncan, 1964; Turner and Leatherman, 1997). The beach water table can change not only due to variations in the inland water table, but also when the sea level rises causing infiltration of seawater into the beachface. Areas where local increases in the water table occur might drive localized 'hot-spots' of the lower beachface volume. Such hot-spots are difficult for coastal engineers to model, yet they can be a large contributor to the coastal erosion hazard (List et al., 2006). Such hot-spots may play a role in the development of patterns on beaches, which have been attributed to rip current circulation (Thornton et al., 2007), the influence of offshore structures and/or the coupling with offshore bars (Castelle et al., 2010). In the case of patterns caused by rip currents, the mega-cusp embayment generally occurs at the intake of the rip current (e.g. Thornton et al., 2007; Short and Hesp, 1982).

The largest change in water level on a meso- to macro-tidal beach is caused by the tide. At high tide, the infiltration from the elevated sea level causes the groundwater table to rise. During the descending tide, if the beach drains more slowly than the tide falls, the groundwater table separates from the sea level, water outcrops in the intertidal zone and the groundwater seepage face will be formed between the shoreline (*SL*) and the groundwater seepage line (*GWSL*) (Turner, 1993, 1995). The groundwater seepage line often appears on gently sloping, fine-grained beaches

especially with large tidal ranges (Turner et al., 1997; Huisman et al., 2011). The sediment characteristics control the drainage rate by controlling the hydraulic conductivity. On a cross-shore profile of the beach, the upper limit of the seepage face indicates the groundwater exit point that differentiates the upper unsaturated zone from the lower saturated land part. The groundwater exit point is the point at which the seepage line intersects a beach profile.

The relationship between the beach groundwater table and beach profile changes has been demonstrated in numerous field investigations (e.g. Duncan, 1964; Eliot and Clarke, 1986, 1988; Turner, 1993; Turner and Leatherman, 1997; Li et al., 2002). Duncan (1964) studied the cyclic beach cut and fill patterns in foreshore beach profile during a single semi-durnal tidal cycle on the gently-sloping Manhattan Beach, California. He attributed some of the variations to the interaction between the location of the swash zone and the groundwater out-cropping. Harrison (1969) built on this earlier study by empirically showing that the ratio of the hydraulic head of the groundwater to the swash run-up may explain the changes in foreshore morphology during the falling tide. Field experiments by Eliot and Clarke (1988) confirmed that when the beachface was most saturated and the groundwater table was at the highest elevation, the maximum beach profile erosion occurred, although results were dependent on slope. Turner (1993, 1995) measured the dynamics of the groundwater exit point and development of the groundwater seepage face using linear interpolation between piezometer data over a tidal cycle and compared results to his model “SEEP” at North Harbour Beach, Queensland, Australia. In his model, the seepage face was a function of the profile slope and permeability characteristics only. According to his results, the elevation of the groundwater seepage line decreases with increasing hydraulic conductivity and beachface slope and even small changes in beachface slope and permeability characteristics caused large changes to the seepage line movement.

The movement of the seepage line and the variation of the saturated zone on the beach have been modeled more extensively using Darcy's Law and various approximations to Laplace's equations. The Boussinesq equation, a simplified form of

Laplace's equation, has also been used to predict the surface of the beach groundwater table. Parlange et al. (1984) applied the non-linear one-dimensional Boussinesq equation to calculate the unconfined groundwater flow induced by tidal variation. Nielsen (1990) used an analytical solution to the Boussinesq equation and assumed that the beachface slope was a constant to show that the groundwater table fluctuations became negligible with increasing the shoreward distance. Baird et al. (1998) showed that the groundwater flow could be explained by the one-dimensional Boussinesq equation.

$$\frac{\partial h}{\partial t} = \frac{K}{S_y} \frac{\partial}{\partial x} \left(h \frac{\partial h}{\partial x} \right) \quad (\text{Eq. 3.1})$$

where h is the groundwater table elevation, K is the hydraulic conductivity of the beach, S_y is the specific yield (also described as a dimensionless parameter called porosity), x is horizontal cross-shore distance, and t is time. The assumption of applying this equation is that the Dupuit-Forchheimer (D-F) approximation describes the groundwater flow. The D-F approximation assumes that the groundwater flow is horizontal and changes in the hydraulic head with groundwater depth are negligible. In this case, the surface slope of the groundwater table is assumed to be relatively small (e.g. Kirkham, 1967, Baird et al., 1998).

Raubenheimer et al. (1999) applied a non-linear one-dimensional Boussinesq equation (Eq. 3.1) and the linear form (Eq. 3.2).

$$\frac{\partial h}{\partial t} = \frac{KD}{S_y} \frac{\partial^2 h}{\partial x^2} \quad (\text{Eq. 3.2})$$

where D is the averaged-aquifer thickness. They showed that using a variable aquifer depth (rather than constant) and linear (rather than non-linear) solution had only a minor effect on the modeled water table. Previous studies carried out by Nielsen (1990) had shown that the linear solution with constant saturated aquifer thickness (Eq. 3.2) could be used if the ratio of the tidal range to the aquifer thickness is small. In this equation, the density gradients are assumed to be negligible and horizontal flows are much greater than vertical flows. The study carried out by Raubenheimer et al., (1999) showed that under their model assumptions, the horizontal flows on a

beach are usually much larger than vertical flows. Li et al. (2006) also applied the 2D form of the Boussinesq equation (in horizontal cross-shore and alongshore directions) showing that their model was sensitive to the ratio of K/Sy .

Although the relationship between the groundwater and the beachface volume has been studied previously, very few people have modeled the beach profile changes caused by groundwater variations. For instance, Li et al. (2002) presented a numerical model to simulate the interaction between the wave motion, the groundwater, the swash sediment transport and changes in beach profiles. The model solved the Laplace equation for saturated flow in the aquifer, and was coupled to a sediment transport morphological model to predict profile variations including formation of a bar and berm. However, they noted that the model needed to be validated using field experiments.

The objectives of this Chapter are two-fold: Firstly, to study the correlation between the groundwater seepage line (*GWSL*), surfzone morphology (*SM*) and the intertidal beachface volume (*Vo*) on a gently-sloping beach (Muriwai Beach) to see to what degree the alongshore variation in the beach morphology is related to the alongshore changes in the *GWSL* and *SM*. Secondly, to present a numerical model based on the Boussinesq formula to study the effect of the beach properties and seaward water level conditions on changing the groundwater seepage line across the beach profile. The model is used to explain the correlations observed in the field by investigating the sensitivity of the seepage line to beach hydraulic conductivity, beachface slope, tide variations and wave set-up. The outcome of this study will be a better understanding of the processes that control hot-spot occurrence on beaches and lead to better models for predicting lower beachface volume hazards.

3.2 Field data

3.2.1 Site description

As it mentioned in the first Chapter, Muriwai beach is a meso-tidal gently-sloping beach located on the west coast of New Zealand's North Island, approximately 35 km west of Auckland and 48 km south of Kaipara Harbour entrance (Figure 3.1). The study area is the 2.5 km stretch located between Okiritoto Stream and Otakamiro Point. The beachface has an average slope of 0.01 and generally consists of fine black sands with the mean diameter of 0.25 mm (Brander and Short, 2000). The groundwater seepage face, which generally appears between the shoreline (*SL*) and the groundwater seepage line (*GWSL*) during the retreating tide, is clearly exposed as a glassy surface, and so could be obtained using standard surveying techniques.

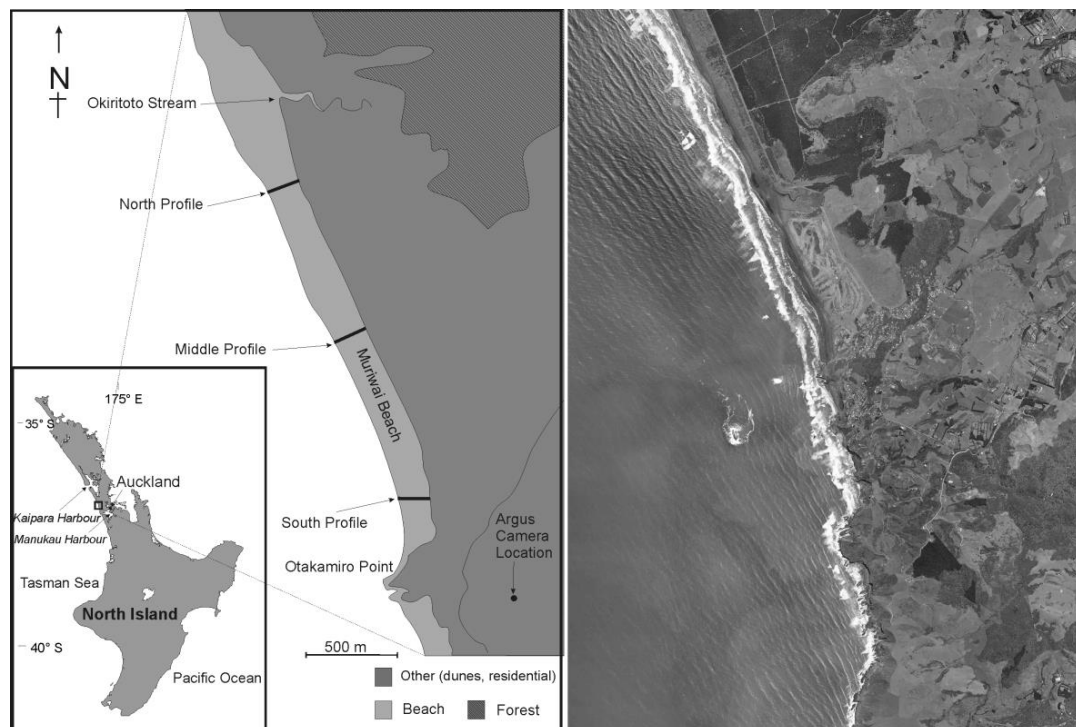


Figure 3.1 Left panel: Location of the field site on the northwest coast of the North Island of New Zealand; Right panel: Aerial image of the Muriwai Beach and the studied zone (Image retrieved from Land Information, New Zealand).

3.2.2 Surveying data

In 2003, Amy Robinson surveyed the beachface and the seepage line using an RTK-GPS (the real time kinematic global positioning system), which was fixed to a quad bike and collected points continuously with 10 m intervals and 1 s frequencies. These surveys were repeated every 3 months for one year, giving five datasets. In December 2002 and October 2003, full beach surveys were collected at 20 m cross-shore intervals. In addition, the *GWSL* was surveyed by driving the bike along the edge of the saturated-unsaturated boundary. One *GWSL* survey was taken in December and one in October. During February, May and August 2003, surveys were taken every 30 minutes between the high and the low tide following the retreating groundwater seepage line. Three shore-normal beach profiles entitled "South", "Middle" and "North" (Figure 3.1), which are 330, 1280 and 2150 m from Otakamiro Point respectively, were surveyed in five months (Robinson, 2004).

In this study alongshore variation of the intertidal beachface volume was calculated by gridding the RTK-GPS data on a 5 m (alongshore) by 1 m (cross-shore) grid. The surveying positions were transformed into an alongshore and cross-shore aligned coordinate system. This was accomplished by defining a common baseline shoreline, and calculating the perpendicular distance between each surveyed data point and this baseline. The beach was re-gridded onto this coordinate system, and the volumes calculated using an area-preserving gridding routine. This transformation caused the beach to be straightened. The surveyed seepage line was also transformed to the same coordinate system. Figure 3.2 shows an example of the straightened beach in February 2003. The gridding scheme interpolated outside the region where the data was collected (data collected by Amy Robinson, 2003, 2004). In the analysis, only the beach volume in the intertidal region was calculated. Smith and Bryan (2007) showed that the changes in intertidal beachface volume could be a representative of the total beach volumetric change. The intertidal zone is shown as the region between the high tide and the low tide elevation contours (Figure 3.2 red dash-dot and red dash line, respectively). Black dots indicate four *GWSL* surveys carried out between the high

tide and the low tide. The de-coupling of the lowest groundwater seepage line, surveyed at low tide, from the low tide elevation is evident.

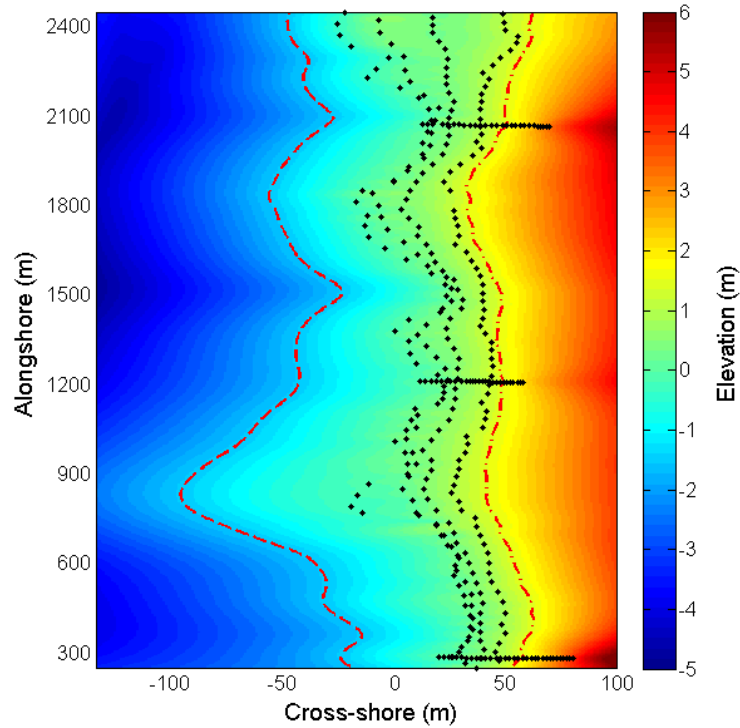


Figure 3.2 Surveying data in February 2003 including four groundwater seepage line measurements and three beach profiles (the profiles are three lines that run perpendicular to the beach). The area between red dashed line and red dashed-dot line indicates the intertidal beach zone.

3.3 Methods

3.3.1 Video images

As rip currents can also have a significant effect on beach cross-shore changes (e.g. Thornton et al., 2007), surfzone morphology was quantified using an ARGUS video imaging system located at the top of the hill in the southern end of Muriwai Beach near Otakamiro Point (Figure 3.1). Collected data consist of three different images: single snapshot, time-averaged and variance images. There is a correlation between light intensity in the time-averaged images and the location of submerged sand bar crests, as demonstrated by Lippmann and Holman (1989). In time-averaged images, areas with low intensity, which appear darker, show rip currents. Sand bars are often intersected by cross-shore rip channels and appear lighter in time-averaged images (e.g. Holman and Stanley, 2007, Lippmann and Holman, 1989). In this study, time-averaged images (which are the average of 10-minutes of video footage at Muriwai Beach) were rectified and then the alongshore variation of the pixel intensity was extracted (Figure 3.3). The pixel intensity was extracted as a cross-shore average in the surfzone area. It is assumed to be an indicator of the influence of surfzone morphology and so hereafter is referred to as “surfzone morphology (*SM*)”. The *GWSL* can be also extracted from time-averaged images (Huisman et al., 2011), although in this study I used surveyed *GWSL*.

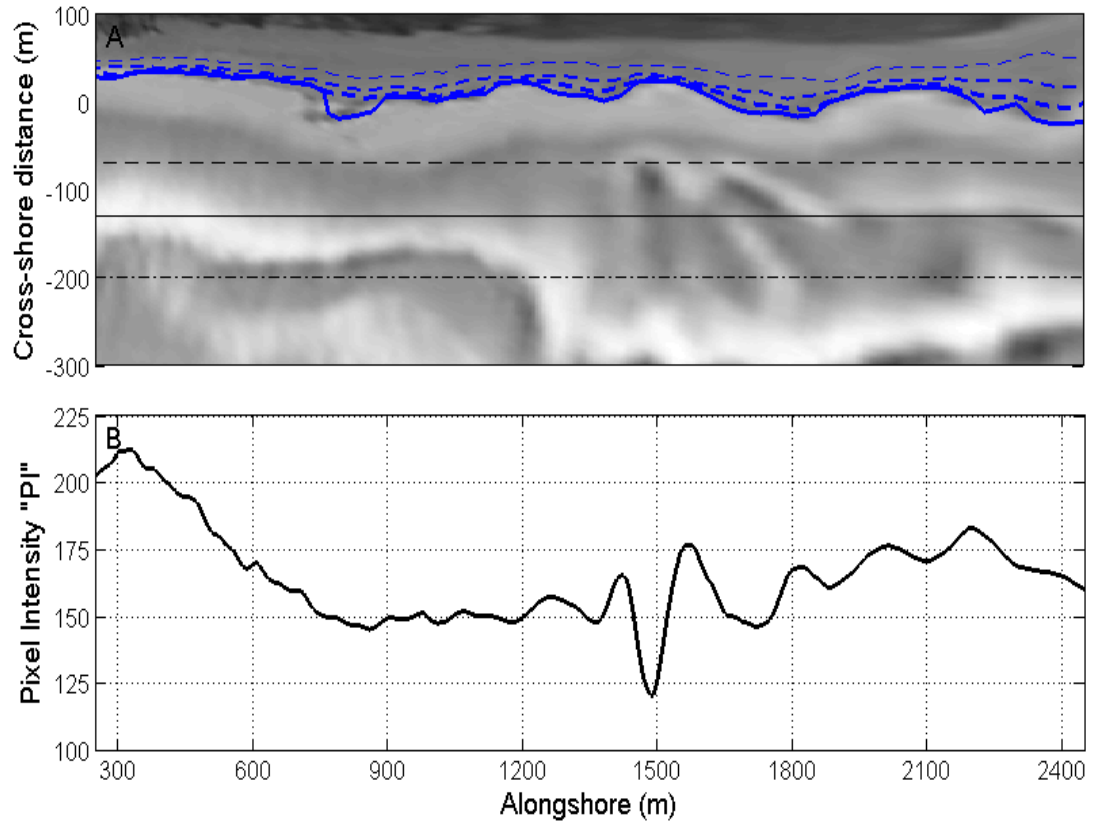


Figure 3.3 Panel A: Straightened and interpolated time-averaged image in February 2003 (taken at low tide). The area between the horizontal black line and dash line indicates the inner zone; and the outer zone is specified between the black line and the dot-dash line. In the top of the image, ticker blue line shows the lower seepage line among four observed seepage lines. Panel B: Variations of the pixel intensity versus alongshore distance.

3.3.2 Statistical methods

The variation in the intertidal beachface volume (V_o) was regressed against the groundwater seepage line ($GWSL$) and surfzone morphology (SM) using five regression models. Three linear regression and two nonlinear regression models were considered:

$$\text{Model 1: } V_o = a_1 + a_2 \times GWSL \quad (\text{Eq. 3.3})$$

$$\text{Model 2: } V_o = a_1 + a_2 \times SM$$

$$\text{Model 3: } V_o = a_1 + a_2 \times GWSL + a_3 \times SM$$

$$\text{Model 4: } V_o = a_1 + a_2 \times GWSL + a_3 \times SM + a_4 \times GWSL \times SM$$

$$\text{Model 5: } V_o = a_1 + a_2 \times GWSL + a_3 \times SM + a_4 \times GWSL^2 + a_5 \times SM^2 + a_6 \times GWSL \times SM$$

where a_i are the regression coefficients. The regression analysis was performed using sliding windows, where the window was moved alongshore to provide alongshore continuous estimates of the regression coefficients (values for the r-square and F-statistic). A range of window sizes (20-200 points) was trialed with the objective of maximizing statistical significance of the model results for each of five datasets and five regression models (19 windows=475 runs). This made it possible to identify the window size with the highest r-square combined with the highest statistical significance level. To determine the statistical significance level within each data block, I could not use every point of the V_o , SM and $GWSL$ time series, because the points are auto-correlated and not independent (the number of points is subjectively chosen in the gridding). Hence, the number of independent points was calculated using the autocorrelation (so, for example, if the points de-correlated at 20m, then only every fourth point is independent, and the degrees of freedom for a 50 point window should be approximately 12 points). The F-statistic value was compared with two F-statistics values ($\alpha=5$ and 10%, where α is the statistical significance level), to determine if the results were significant.

3.3.3 Numerical modelling

The statistical analysis can detect correlation but not establish causation. Therefore, to interpret the results of the analysis, I tested the sensitivity of the seepage line to beach hydraulic conductivity, beachface slope, tide variations and wave set-up. The horizontal shore-normal groundwater flow through an aquifer can be explained by Boussinesq equation (Eq. 3.2). According to the Krumbein and Monk formula (1942), the hydraulic conductivity (K) can be calculated based on the mean grain size and grain sorting characteristics (Eq. 3.4a) (e.g. Turner, 1995; Baird and Horn, 1996).

$$K = \frac{760.g.d_m^2.e^{1.31\phi}}{\nu} \times 0.987 \times 10^{-12} \quad (\text{Eq. 3.4a})$$

where, g is the acceleration due to gravity, d_m is the mean grain size (mm), ϕ is the standard deviation of grain size (mm) and ν is the kinematic viscosity of the beach groundwater ($\text{m}^2.\text{s}^{-1}$). Sediment porosity was also estimated from Vukovic and Soro (1992) (Odong, 2007):

$$n = 0.255 \left(1 + 0.83 \frac{d_{60}}{d_{10}} \right) \quad (\text{Eq. 3.4b})$$

where, d_{10} and d_{60} are the grain diameter in (mm) for which 10% and 60% of the sample are finer, respectively. In this study, 74 sediment samples collected over five months along the north, middle and south profiles were used to calculate the hydraulic conductivity (Robinson, 2004). The estimated hydraulic conductivity using ranged from 0.00016 to 0.00059 m/s at different alongshore and cross-shore locations. The average calculated porosity (Eq. 3.4b) was 0.45.

The numerical model developed for this study used a standard explicit finite difference method to solve the governing equation (Eq. 3.2), based on forward differencing in time and central differencing in the cross-shore position. A small time and distance step ($\Delta t = 0.5$ minutes, and $\Delta x = 1$ m) were used in the model to ensure the stability of the numerical solution. Figure 3.4 shows an example of the modeled groundwater profile during a tidal cycle of 3.2 m. The thicker lines show the

groundwater profile at low tide. Two months (August as an indicator of winter in New Zealand and February for summer) were studied.

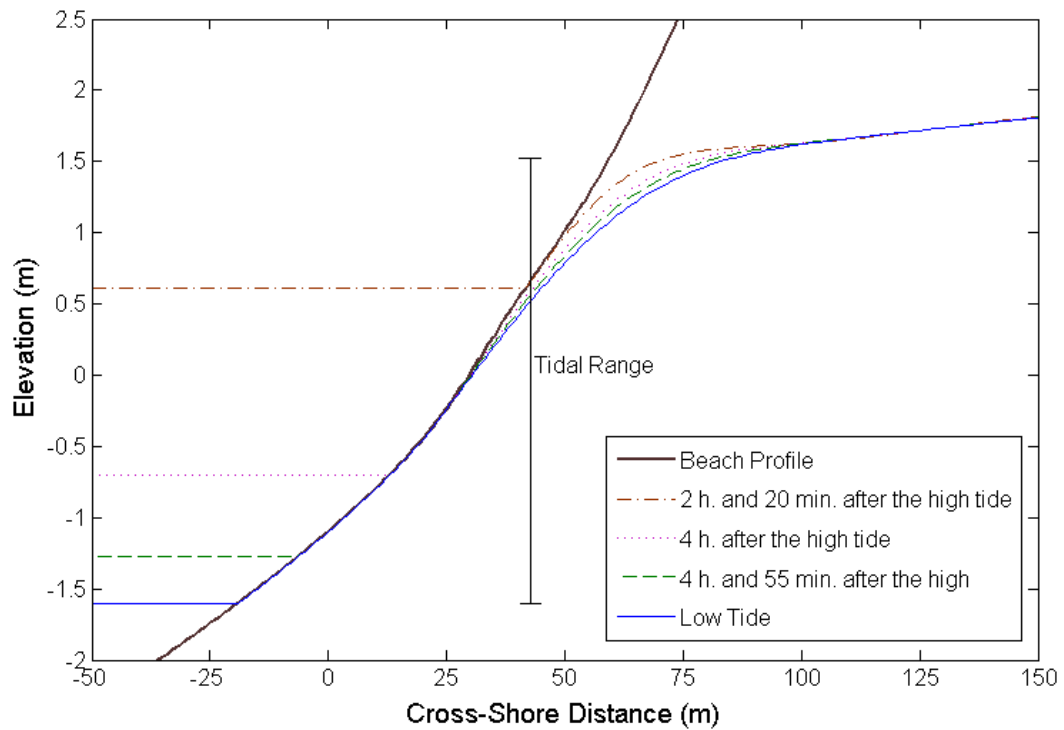


Figure 3.4 Beach groundwater profile during a tidal cycle (example for a beach profile in February)

The landward boundary condition of the model was set to the inland groundwater table (assumed to vary between 1 and 4 m above the mean sea level). When simulating observed groundwater seepage line, this was used as a fitting parameter. The seaward boundary was also set to the tide elevation with or without adding an offset to simulate the wave set-up. The tidal range was selected according to the NIWA tide model forecast for each survey date, and varied between -1.55 and 1.54 on 18thFebruary and between -1.37 and 1.52 on 28thAugust 2003.

The wave set-up was approximated using Bowen et al. (1968) formula for these months. However, the wave set-up varying between zero and one was used in sensitivity analysis.

$$\eta_{set-up} = \frac{3}{8} \gamma^2 \frac{(h_b + h_{tide})}{(1 + \frac{3}{8} \gamma^2)} \quad (\text{Eq. 3.5a})$$

$$h_b = \frac{H_{rms}}{\gamma} \quad (\text{Eq. 3.5b})$$

$$H_{rms} = \frac{H_S}{\sqrt{2}} \quad (\text{Eq. 3.5c})$$

where h_b is the height of the breaking wave, H_{rms} is the root mean-square wave height, H_S is significant wave height, h_{tide} is tidal level, γ is the wave breaking coefficient, and η_{set-up} is the wave set-up height. A γ of 0.55 was assumed, which is consistent with other studies (e.g. Bryan et al., 2007). Considering the mean significant wave height of 2.57 m in August and 1.87 m in February (retrieved from the NOAA global wind cast (<ftp://polar.ncep.noaa.gov/pub/history/waves>, 2003), the average wave set-up heights of 0.53 and 0.43 m were obtained in these months respectively.

3.4 Field data analysis and results

Figure 3.5 shows the results of statistical model 3, where V_o was regressed with independent values of $GWSL$ and SM . The r-square value of the regression model usually decreases with an increase in the number of points used in the sliding window (Figure 3.5A). For all five datasets, the highest r-square values are obtained using a window size of 20 points. The second panel shows the statistical significance, which was calculated based on the number of independent points (adjusted degrees of freedom) in each of the sliding windows. Statistically significant results (with a 95% confident level) were obtained for 4 of the datasets (August, February, May and October) using a window size of 50 points (equal to 250 m alongshore). No window size provided statistically significant results in December.

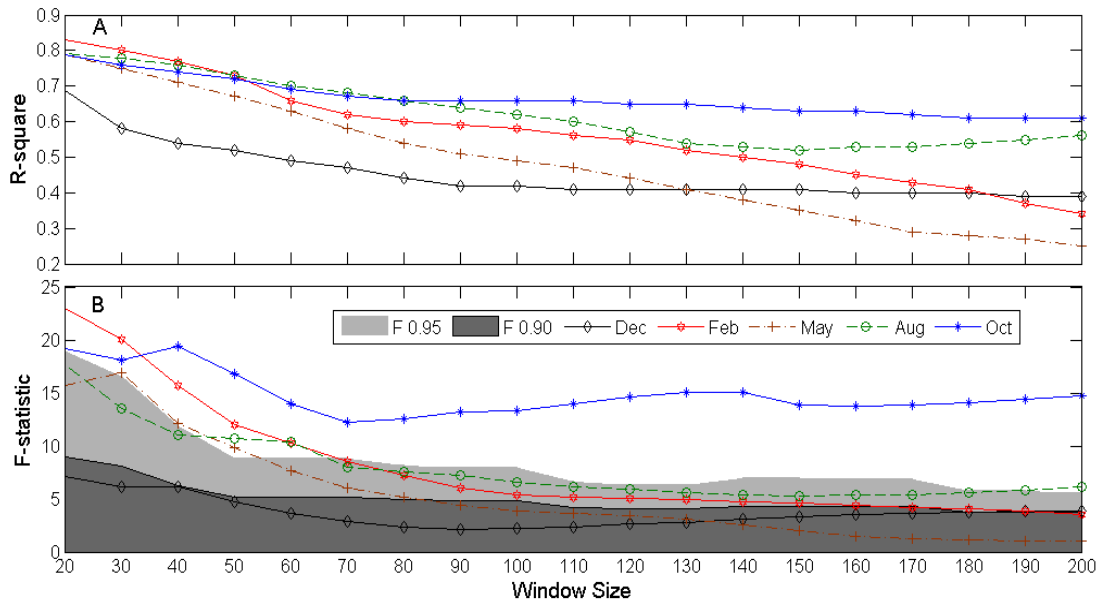


Figure 3.5 Panel A: the variation of the r-square values for model 3 ($V_o = a_1 + a_2 \times GWSL + a_3 \times SM$) versus window sizes in 5 months. Panel B: the variation of the F-statistic with window size and the zone of statistically significant results (at $\alpha=5$ and 10%).

Figure 3.6 shows the difference between r-square values for the five different models for each of the five datasets. Although the r-square increases with adding the cross-terms, the results obtained using the more complex models 4 and 5 are not significant, and model 3 (with *GWSL* and *SM*) provides the best r-square improvement.

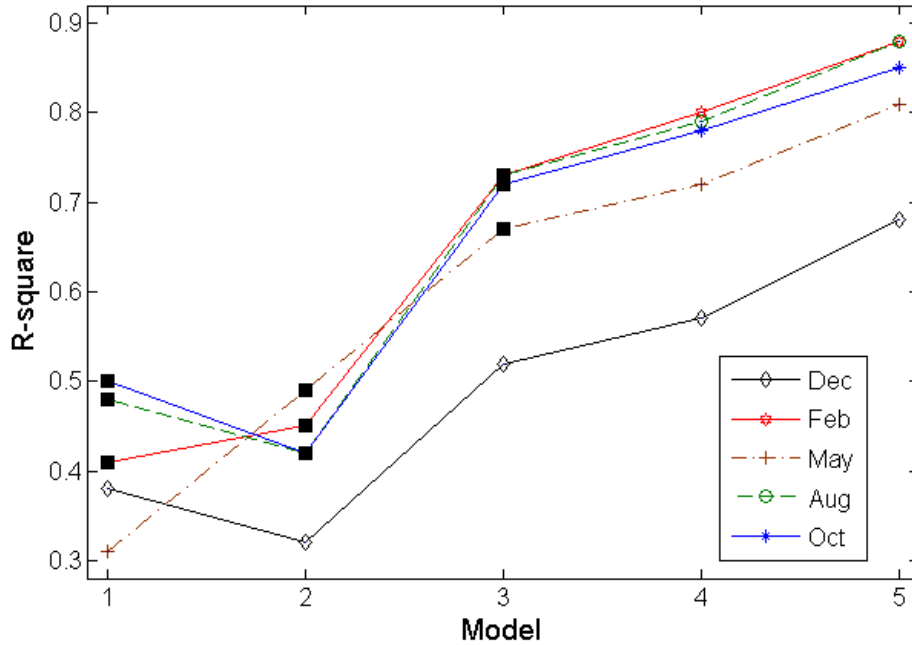


Figure 3.6 Variation of the alongshore-averaged r-square versus different models in five months. The black squares show the statistically significant results at $\alpha=5\%$.

Figure 3.7 shows the variation of V_o , *GWSL* and pixel intensity (*PI*), and the r-square of the regression models versus alongshore distance for February. In this Figure, the lowest *GWSL* observed in February and the pixel intensity averaged over the surfzone (an indicator of the surfzone morphology) are shown. Sliding the regression analysis windows along the beach made it possible to differentiate regions of the beach where the intertidal beachface volume was correlated with the *GWSL* elevation and *SM* from areas where it was not. In most regions of the beach, there is some correlation between V_o and *GWSL*, with an elevated *GWSL* correlating with a reduced V_o . At some parts of the Muriwai Beach, areas with high *PI* were correlated with lower V_o . In all datasets, the gradient of the regression line between the

alongshore variation of V_o and SM was not always negative. This often occurred in middle of the beach.

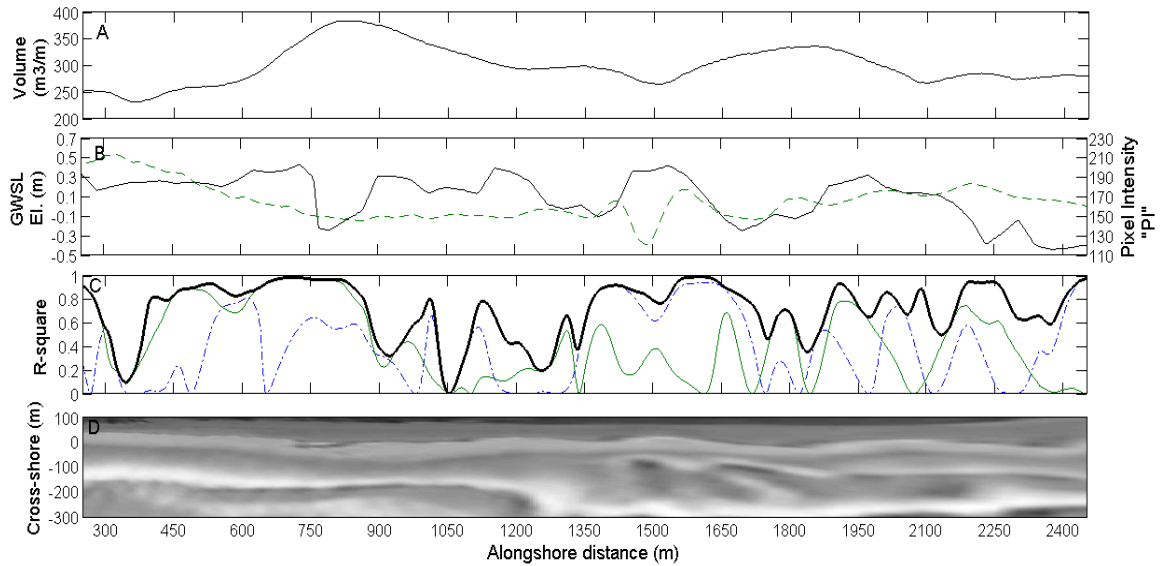


Figure 3.7 Panel A: The alongshore variation of the intertidal beachface volume. Panel B: The groundwater seepage line elevation (solid black line) and the pixel intensity (dashed green line). Panel C: Regression r-square values. Dashed blue line: using just groundwater seepage line (model 1), green line: using just pixel intensity - or surfzone morphology- (model 2) and thicker black line: using a regression model with both groundwater and surfzone morphology (model 3). Panel D: The rectified averaged video image of Muriwai Beach in February 2003. Shoreward is at the top and seaward at the bottom. This is taken from the Argus video network by R. A. Holman (<http://cil-www.oce.orst.edu/>)

The change in the correlation between $GWSL$ and V_o varied during the tidal cycle (more than one measurement per tidal cycle were collected in three of the datasets). For example, Panels A and B of Figure 3.8 show the alongshore variation of V_o and $GWSL$ elevation for February 2003. At low tide, the intertidal beachface volume usually increased with decreasing seepage line, although there is not high correlation between V_o and $GWSL$ at high tide. Panel C shows that r-square of the relationship between V_o and $GWSL$ for August, February and May datasets at low tide is higher

than the r-square at high tide, and a descending trend of r-square from low tide to high tide is clear. For instance, in February, the r-square falls from 0.41 at low tide (with mean groundwater seepage elevation of 0.01m) to 0.34 at high tide (with mean elevation of 1.07m). This figure also shows that in winter (August) the low-tide GWSL is more related to the beach volume than in late summer.

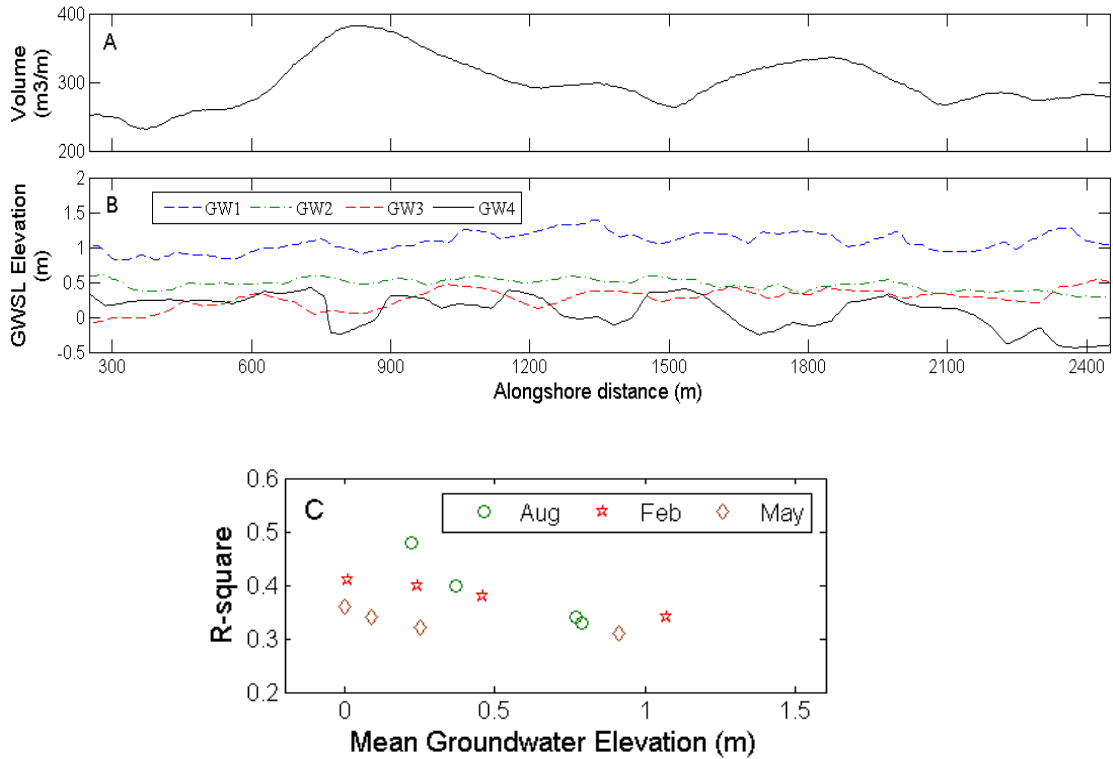


Figure 3.8 Panel A and B: The alongshore variation of intertidal beachface volume and different groundwater seepage measurements in February 2003. Panel C: Variation of r-square versus different mean groundwater elevations in 3 months. The r-square values are only for the regression between volume and groundwater (model 1).

3.5 The numerical model results

Theory indicates that the groundwater seepage rate should be inversely proportional to beach slope, and so it may be that the correlation with beach volume is not an indicator of lower beachface volume but of sensitivity to slope. The sensitivity of the cross-shore location of *GWSL* to various environmental parameters was studied using Eq. 3.2. Firstly, the hydraulic conductivity was assumed to be constant and the variation of the *GWSL* due to the changes in landward and seaward boundary conditions was studied for a specified beach profile. It was found that the effect of changing the seaward boundary water level is greater than changing the landward conditions. Although, the *GWSL* elevation increases with a rise of the inland groundwater table elevation (*WT*), tide elevation (*TR*) and wave set-up (*S-U*), wave set-up causes a larger effect on the *GWSL*. Figure 3.9 shows that on average, a 100% change in wave set-up causes a 113% change in the *GWSL* elevation, however 100% changes in *WT* and *TR* cause 81% and 72% variation in *GWSL* elevation, respectively.

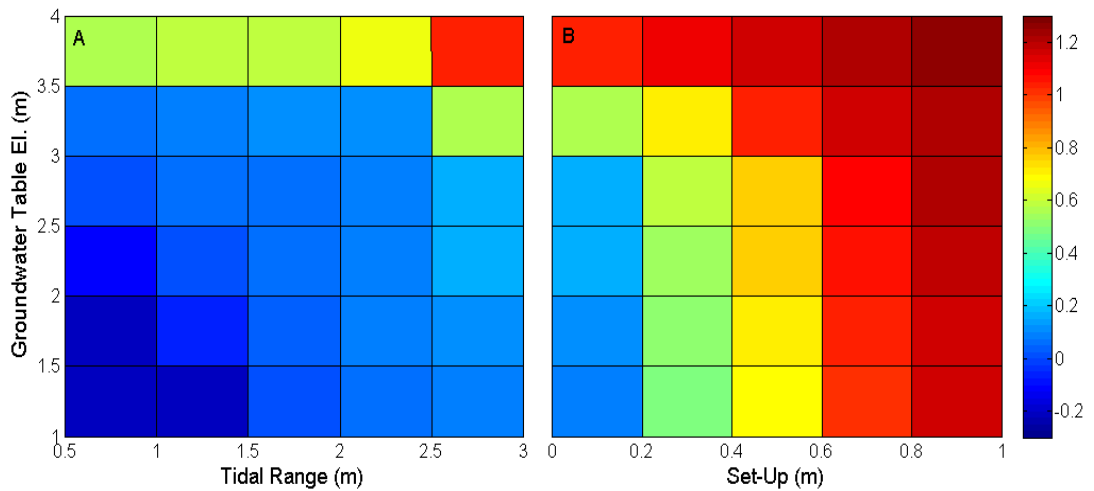


Figure 3.9 Variation of the groundwater seepage line elevation versus the inland groundwater table, tide elevation and wave set-up

Secondly, to study whether the distribution of the observed hydraulic conductivity (K) and the beachface slope (S) could cause the observed distribution of $GWSL$ elevation, WT , TR and $S-U$ were assumed to be constant, and the K and S were varied. The range of the hydraulic conductivity at Muriwai Beach was calculated using the range of alongshore sediment textures (Figure 3.10 Panel D). The measured slope along profiles were also used in the model (Panel E). The range of the observed $GWSL$ (Panel A) was compared with the range of model results (Panel B and C). Panel B, shows the model results, which were calculated with different values of K , and the mean slope (solid line) and the range of beach slope (the 10 and 90 percentile). The modeled $GWSL$, which was obtained with different values of S is also shown in panel C. In this panel, each curve indicates the hydraulic conductivity associated with the mean observed hydraulic conductivity and the range (10 and 90 percentile). The $GWSL$ elevation depends on either K or S , has a descending trend and the $GWSL$ calculated by Boussinesq formula is in the range of the observed groundwater seepage data. In my study, for the average of S (0.028), the $GWSL$ elevation is reduced by 50 cm when K is tripled; while, for the mean of observed K , when S is tripled the $GWSL$ elevation is reduced by around 170 cm, indicating a stronger sensitivity to slope than hydraulic conductivity on Muriwai Beach.

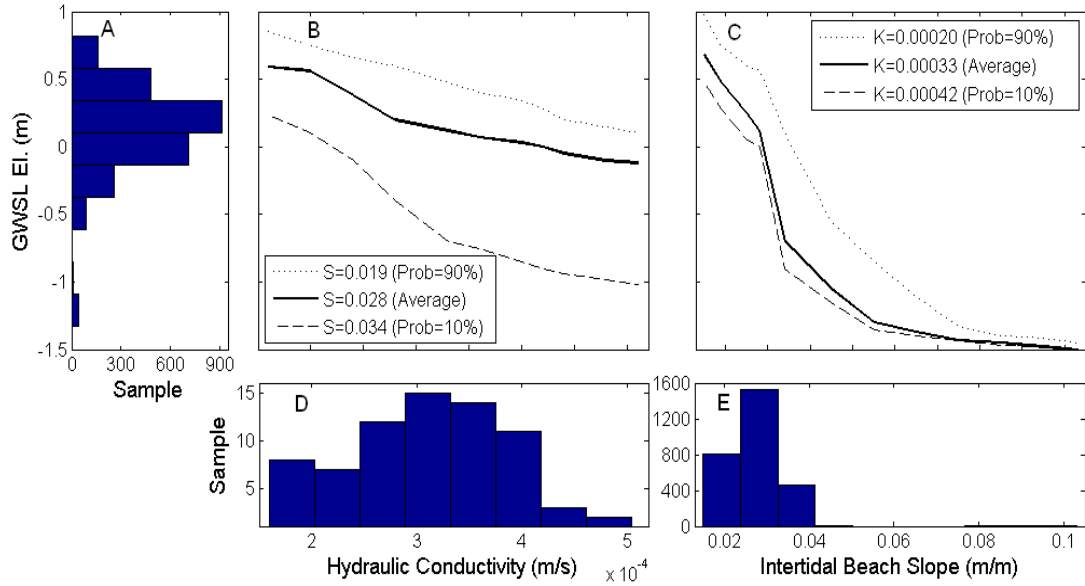


Figure 3.10 Observed Groundwater seepage line (GWSL) and variation of the numerical model results versus hydraulic conductivity (K) and intertidal beach slope (S). Panel A: The observed GWSL elevation collected at Muriwai Beach. Panel B: The model results, which were calculated with different values of K . Each curve indicates a specified S . Panel C: The modeled GWSL, which was obtained with different values of S . Panel D: The histogram of K , which was calculated based on the field sampling. Panel E: The histogram of S obtained from the beach survey.

The model could also be used to determine the sensitivity to unknown set-up and inland water table elevations, by using known S and K , and determining how much remaining variability was controlled by these two remaining factors. Profiles were extracted from the straightened beach (Section 2.2) at 10 m alongshore intervals for two different months (February and August as indicators of summer and winter conditions, respectively). Figures 3.11 and 3.12 (Panels A and B) show the alongshore variation of the observed groundwater seepage line and the calculated seepage line based on the Boussinesq equation (Panel A shows results 2 hours after the high tide, and panel B shows results just before the low tide). The model results were obtained using the tidal range on the day of sampling, and the optimized inland

groundwater elevation and wave set-up height (optimized to provide the best fit of model and observations). Panel C shows the variation of the optimized wave set-up.

In summer, the numerical model results are completely consistent with observation at 2 hours after the high tide (Figure 3.11A). At the low tide, modeled results are not fully comparable with observations, especially in the middle of Muriwai Beach (Figure 3.11B). In winter, the model results, which were obtained at 2 hours after the high tide are consistent with observations apart from the southern end of the beach (Figure 3.12A). At the low tide, modeled results are compatible with observations, apart from the middle of the beach (Figure 3.12B).

To determine what factor has the greatest control on the alongshore variability observed at Muriwai Beach, the parameters that contribute to the model, were varied sequentially. Among the factors in the model, S and K were obtained from the field survey and tide variation was extracted from NIWA tide model forecast (section 3.3); hence, I analyzed the sensitivity of the model to other parameters. Panel (D and E) show the correlation between the modeled and the observed $GWSL$ two hours after the high tide and just before the low tide, respectively (Figure 3.11 for summer and 3.12 for winter). Black circles indicate the model results when WT and $S-U$ are held constant. The effect of adding alongshore variability to $S-U$ is shown with crosses, and squares show the model results when the effect of variability in both WT and $S-U$ were considered together. The oblique line shows the 1:1 line of the perfect fit. Table 3.1 shows the r-square of the regression between the observed $GWSL$ and the calculated $GWSL$. In this table, Model A shows the results when WT and $S-U$ are constant. The effect of changing $S-U$ is shown with Model B, and Model C indicates results when the effect of the WT and $S-U$ are considered.

Table 3.1. The R-square and the root mean-squared error (RMSE) of the regression between the model results and observed field data: Model (A): “K”+”S”, Model (B): “K”+”S”+”S-U”, Model (C): “K”+”S”+”S-U”+”WT”.

	R-Square of the Regression			RMSE		
	Model A	Model B	Model C	Model A	Model B	Model C
Aug. H.T. + 2hrs	0.68	0.96	0.98	0.31	0.13	0.11
Aug. L.T.	0.49	0.89	0.91	0.20	0.10	0.09
Feb. H.T. + 2hrs	0.12	0.87	0.94	0.25	0.06	0.04
Feb. L.T.	0.51	0.65	0.69	0.36	0.19	0.17

The results show that with considering constant values of the inland groundwater elevation and the wave set-up, the root mean-squared error between model results and observed data is between 0.20 and 0.36 m. The error can be reduced by changing *WT* and *S-U*. The table also indicates that the results of models B and C are closer to each other than model A. It means my model is more sensitive to *S-U* rather than *WT*. Model C, which considers *S-U* and *WT*, shows compatible results with observations at high tide (r-square of 0.98 and 0.94 in winter and summer, respectively). However, the r-square decreases to 0.91 and 0.69 for low tide in winter and summer, respectively. It is concluded that my model results are more compatible with observations at high tide rather than low tide.

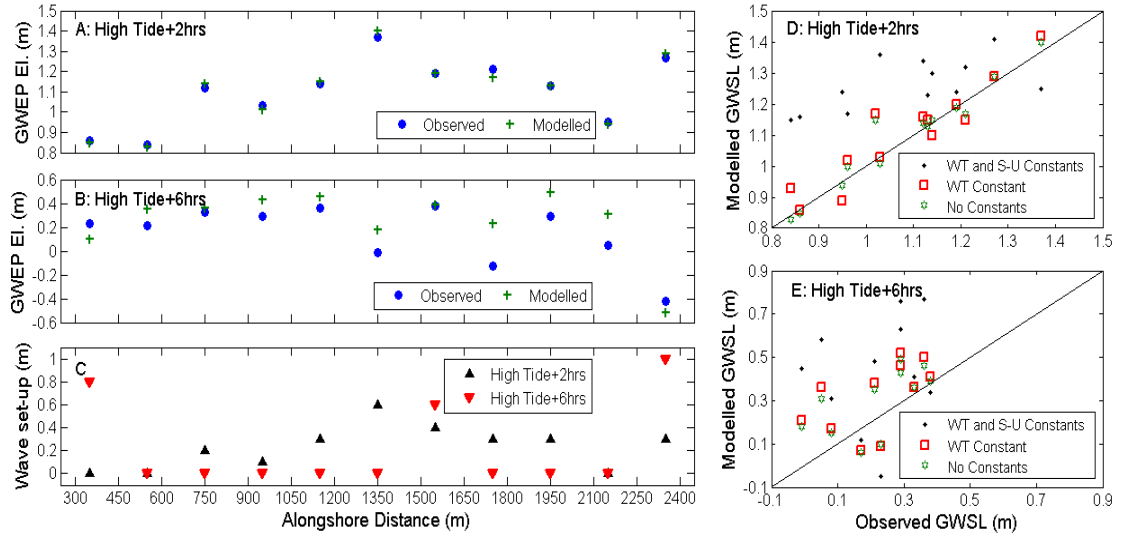


Figure 3.11 Panels A and B: Alongshore variation of the numerical model results and observed groundwater seepage line in February, at 2 and 6 hours after the high tide, respectively. Panel C: Alongshore variation of the optimized wave set-up. Panels D and E: Relation between the modelled and observed GWSL at 2 and 6 hours after the high tide, respectively.

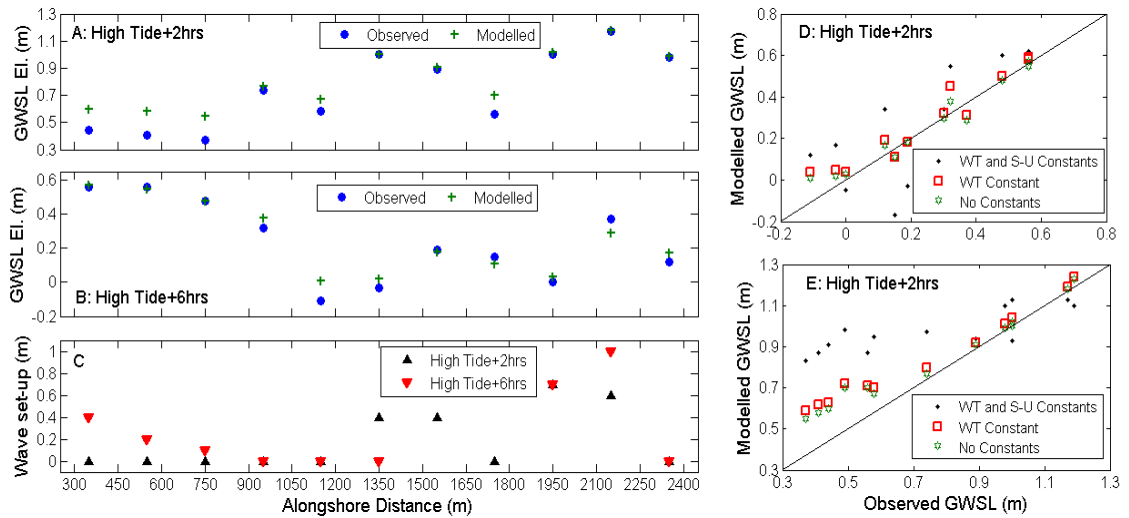


Figure 3.12 Panels A and B: Alongshore variation of the numerical model results and observed groundwater seepage line in August, at 2 and 6 hours after the high tide, respectively. Panel C: Alongshore variation of the optimized wave set-up. Panels D and E: Relation between the modeled and observed GWSL at 2 and 6 hours after the high tide, respectively.

3.6 Discussion

Previous studies have shown that higher water tables influence the swash sediment transport by causing saturation and as a result, beachface volume decreases (Grant, 1948; Duncan, 1964; Eliot and Clarke, 1988; Turner, 1995; Turner and Leatherman, 1997). My results show that in most regions of the beach, there is a clear correlation between V_o and $GWSL$, with an elevated $GWSL$ causing a reduction of V_o . This inverse correlation occurred in all datasets, consistent with other studies (e.g. Duncan, 1964; Eliot and Clarke, 1988; Turner, 1995; Turner and Leatherman, 1997). The seasonal analysis shows that $GWSL$ in winter is more correlated with V_o than summer (e.g. Figure 3.6). The higher inland groundwater table in winter (caused by higher winter rainfall) likely causes more exfiltration on the beachface and, subsequently, lower beachface volume. The field results also indicate that V_o is more correlated with $GWSL$ at low tide rather than high tide (Figure 3.8, panel C), consistent with theory. Increasing hydraulic head at low tide causes stronger seepage flow and greater potential for sediment remobilization. Hence, $GWSL$ has a greater effect lower on the beach, and beachface volume reduction is more influenced by the low tide $GWSL$. The schematic in Figure 3.13 shows a patterned beach morphology inversely correlated with the seepage line, as observed at Muriwai Beach.

Turner (1993) showed that the groundwater exit point ($GWEP$ is where $GWSL$ intersects a beach profile) elevation decreases with increasing K and S and even small changes in S and permeability characteristics cause large differences of the $GWEP$ location. Baird et al., (1998) and Raubenheimer et al., (1999) indicated that the groundwater table fluctuations and the seepage face width depend on the ratio K/n . Li et al., (2008) also showed that for a constant beach slope, smaller K or larger tidal fluctuations increase the seepage face width and $GWEP$ elevation. Confirming previous studies, our modelling results show that $GWSL$ elevation decreases with increasing K and S . Variation of the seaward boundary of the numerical model (tide elevation plus wave set-up) has more influence on changing $GWSL$ than varying the landward boundary condition (inland water table).

The correlation between the V_o and SM is not as easy to interpret as V_o and $GWSL$. My results showed that SM has much the same effect as $GWSL$ on changing V_o . The correlation between V_o and SM (characterized using pixel intensity measurements) indicates that unlike the $GWSL$, which always has negative correlation with V_o , the slope of the regression line between the pixel intensity (PI) and V_o is sometimes negative and sometimes positive. I defined two different process pathways for the SM effect on changing V_o . In the first pathway, there is a positive correlation between V_o and PI as V_o generally decreases with decreasing PI . My statistical results show that in winter, the beach follows this pattern (Figure 3.13A). This is likely due to rip currents causing sediment movement offshore, so that the beach is scoured out landward of the rip current. This often occurred at the middle of Muriwai Beach, which was a region of strong rip current activity (areas with low PI in time-averaged images). Previous studies have showed that the alongshore variation of the lower beachface volume was correlated with the alongshore variation in rip currents (e.g. Thornton et al., 2007). In the second pathway, there is a negative correlation between V_o and PI where V_o decreases with increasing PI . From the statistical results, the beach follows this pattern in summer (Figure 3.13B). In this case, I suggest two mechanisms are responsible: the presence of oblique bars; and the influence of the surfzone morphology on wave set-up. The alongshore variation in PI does not differentiate between oblique bars and rip currents. With oblique sandbars, the shoreline is steeper where the bar is closer to the shore (e.g. 400m-750m in Figure 3.7D). Thus, an in-phase coupling between bar and shoreline due to the sediment exchange between the bar line and beachface can promote lower beachface volume. This in-phase coupling has been reported by Castelle et al. (2010). Double sandbar systems are a common morphological pattern on sandy, meso-tidal beaches with high wave energy (e.g. Ruessink et al., 2003; Castelle et al., 2007; 2010), such as Muriwai Beach. In a double sandbar system, inner-bar rip channels are often smaller and more variable – in alongshore direction – than the outer-bar (Castelle et al., 2010). At Muriwai Beach, the inner bar often exhibited these variably-oriented rip channels. The schematic in Figure 3.13B shows the beach morphology negatively correlated

with the surfzone morphology. In this case, lower beachface volume hot spots tend to occur in the areas with high pixel intensity.

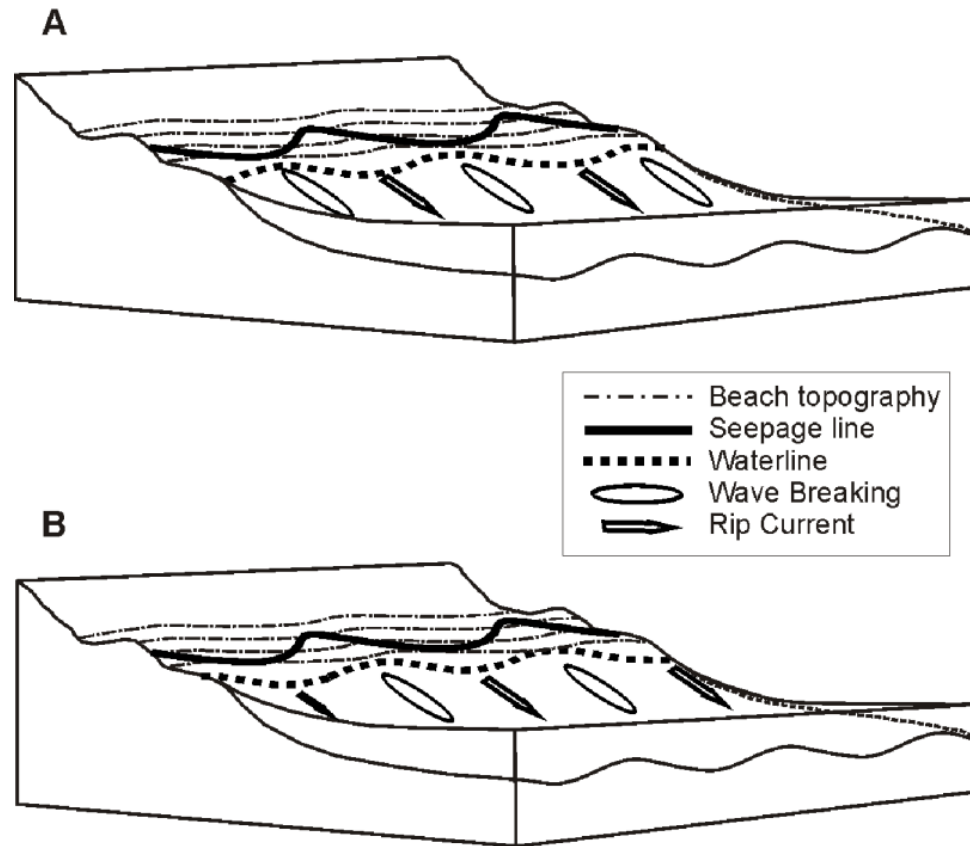


Figure 3.13 Schematic of the beach, and the effect of the groundwater seepage line and surfzone morphology on changing the intertidal beachface volume. (A) for the winter pattern, where surfzone morphology and beach volume are positively correlated; (B) for the summer pattern, where surfzone morphology and beach volume are negatively correlated.

Previous studies showed that the wave set-up varied with the surfzone similarity parameter, which is a function of the height and length of the approaching wave to the beach and the beach slope (e.g. Holman and Sallenger, 1985) and there was a linear relationship between the set-up and wave height (e.g. Lentz and Raubenheimer, 1999). The offshore bar patterns and changes in the bathymetry also affect the set-up

at low tide (e.g. Holman and Sallenger, 1985; Raubenheimer et al., 2001). Laboratory studies carried out by Haller et al. (2002) showed that wave set-up may vary up to 20% of the root mean-square wave height (H_{rms} , which is a function of significant wave height). In this study, wave set-up, especially in high tide, reached nearly 40% of H_{rms} in few alongshore locations, however the average was still around 20% to 30%. Raubenheimer et al. (2001) also indicated that at low tide more set-up was expected than high tide, as dissipation is much stronger over the shallow bar crest than in deep water. My results (e.g. Figures 3.11C and 3.12C) show that the role of the wave set-up in changing the beach groundwater seepage line is more significant at the low tide than high tide in both summer and winter patterns.

Results of this Chapter suggest a potential morphological feedback loop, where morphology influences the seepage line both through slope effects and set-up effects, which drive lower and higher beachface volume, which influence morphology. Furthermore, SM , which was used in the statistical analysis, was not good representation for the location of rips and surfzone morphology changes. Also in modeling Section, inland groundwater table and wave set-up were assumed to be varied between 1 and 4 and between 0 and 1 metre, regarding lack of field data in Muriwai beach. In next Chapters, the numerical model will be applied in Ngarunui beach using field experiment to obtain the key components, which might force the change in the groundwater seepage line across the beachface and provide a better understanding of the interaction between water table and morphology.

In this Chapter, a one-dimensional linear Boussinesq equation was used to predict the beach groundwater behaviour. In Chapter 6, the two-dimensional model will be developed based on both linear and non-linear Boussinesq equation to study the effect of non-linearity of the aquifer depth and hydraulic conductivity, which both were remained constant in linear form. The equation will be solved in both alongshore and cross-shore direction to consider the effect of alongshore groundwater flow in the model.

Chapter 4 : The Use of the Video Imagery to Extract the Groundwater Seepage Line and Shoreline at Ngarunui Beach

4.1 Introduction

Monitoring beach changes through the time has been is of essential interest to coastal engineers because it underpins definitions of coastal hazard zones. One of the cheapest and automated approaches for beach observation is video imagery (Smith and Bryan, 2007). Video-based techniques can be used to determine the location of the shoreline and sand bars (Lippmann and Holman, 1989, 1990) and to extract the wet-dry boundary across the beachface (Huisman et al., 2011). Shoreline can be determined as the bright narrow part of the shore break, which can be defined using time-averaged video images. This technique is based on the difference between the colour or contrast of the dry sand, and the wet sand (Plant and Holman, 1997; Aarninkhof et al., 2003). There are several different approaches to the shoreline mapping method using video images, which were described in Chapter 2. Additionally the wet-dry boundary can be found using time-averaged images, and this line has been shown to be closely associated with groundwater seepage face (Huisman et al., 2011).

Although shoreline detecting from video images has been widely studied, most of these works have been focused on using time-averaged images. Furthermore, there is not much work on extracting the groundwater seepage line from video images on gently sloping dissipative beaches. In this study the images taken by Cam-Era video system at Ngarunui beach were used to extract the shoreline and groundwater seepage line. Every half-hour during daylight conditions, an on-site computer collects a snapshot image, a time-averaged image and a variance image, which described in Chapter 2. Time-averaged images were used to extract the groundwater seepage line at Ngarunui beach. Furthermore, beach shorelines were extracted from variance images and then compared with the surveyed data to evaluate the accuracy of using variance images in shoreline detecting.

4.2 Field data

4.2.1 Site description

As it described in the first Chapter, Ngarunui beach is a dissipative beach, located near Raglan on the west coast. The beach is approximately 1.8 km length, and is almost 4 km south-west of Raglan town (Figure 4.1). There is a steep dune to the east of the beach. To the north, the beach turns into Whaingaroa Harbour. Ngarunui is a black sandy beach with an average slope of 1:70 (Huisman et al., 2011). The spring tide ranges between 2 and 3 m and neap tide is 1.5-1.8 m (Walters et al., 2001).

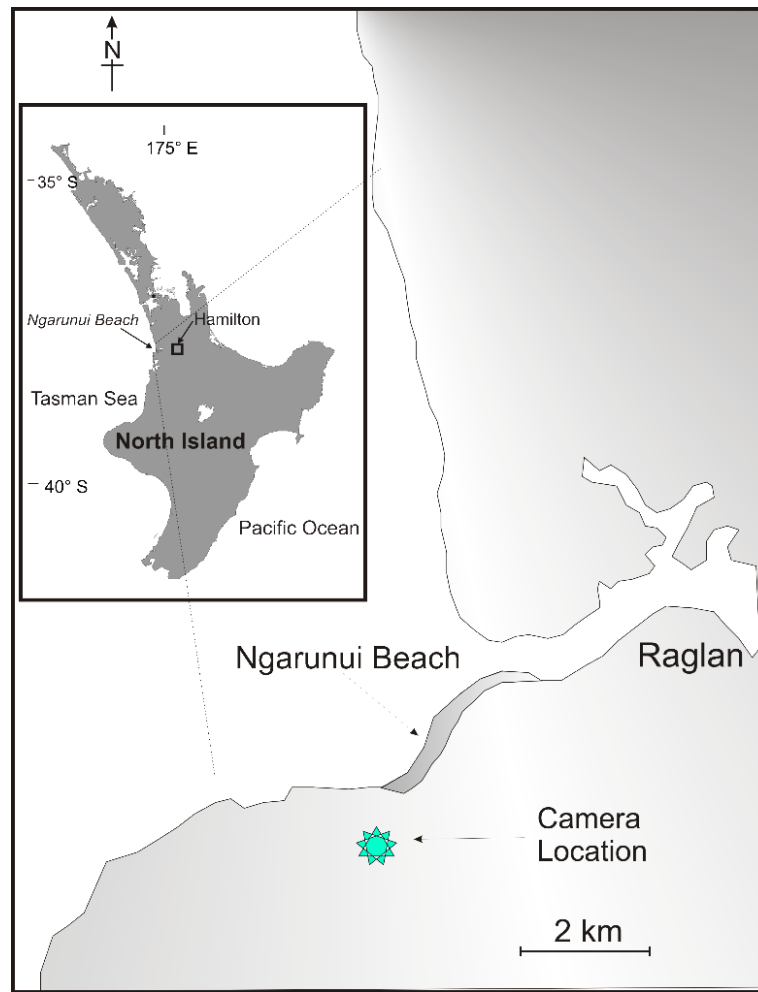


Figure 4.1 Location of the Ngarunui beach on the west coast of the North Island

4.2.2 Video images

Raglan Beach has been monitored since August 2007 by a Cam-Era video system owned by Waikato Regional Council and operated by NIWA (e.g. Almar et al., 2008). The video unit includes a Lumenera LE 375 7.7 mm color CCD video camera with a 25.5 mm fixed-focal-length lens (Huisman et al., 2011). Cameras are located on top of the hill at the south of the beach at 94 m above mean sea level. Every half-hour during daytime, the camera system takes a snapshot image and prepares a time-averaged and a variance image. The difference between time-averaged and variance images is that variance images are produced from the standard deviation of a 10-minute sequence of images, while time-averaged (Timex) images are the time-mean of the same sequence of images. As variance images show the areas of greatest change, they have been mainly used to define the surfzone and the area, which waves break. In this paper the application of these type of images in extracting shoreline is described. Figure 4-2 (upper panel) shows Raglan video cameras (Camera A and B) located on the top of the Bryant home at Ngarunui beach. Lower panels show time-averaged images provided at high tide and low tide.

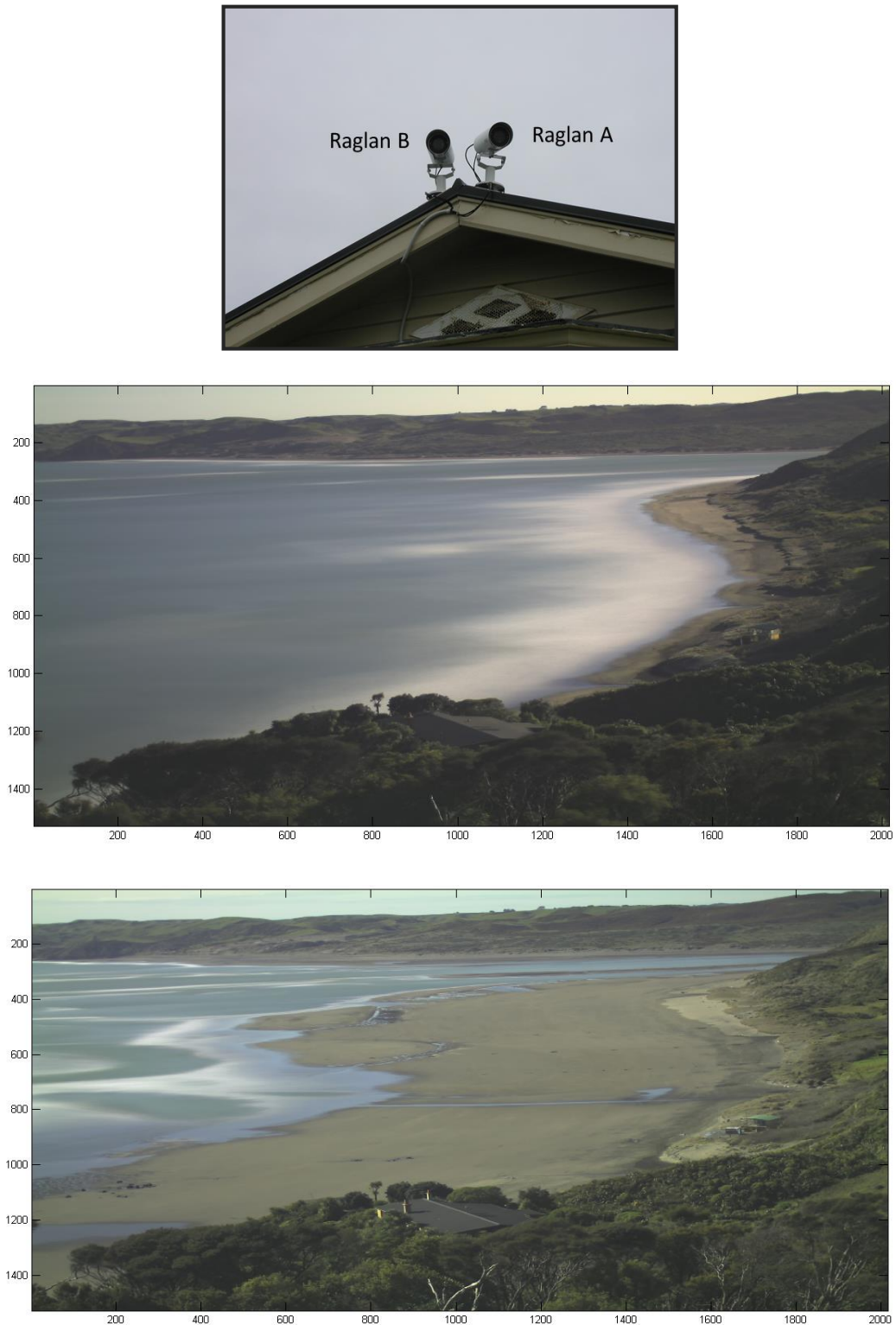


Figure 4.2 Upper panel: Video cameras placed on the top of the home at Ngarunui beach. Lower panels: Time-averaged video images at Ngarunui Beach at high tide and low tide

4.2.3 Survey data

The beach surveys were carried out by Dirk Immenga (UoW) using the RTK GPS mounted on a quad bike recording points every 5 metres. The first survey was carried out in 8th November 2010 between 5:10 pm and 6:10 pm around low tide time. An alongshore extent of almost 650 m was surveyed. Alongshore surveyed lines were 15 to 20 m apart from each other and they cover the area between dune toe to the shoreline. The second survey was conducted by Cliff Hart (NIWA) in 9th November 2010 between 7:00 pm and 9:30 pm (Guedes, 2010).

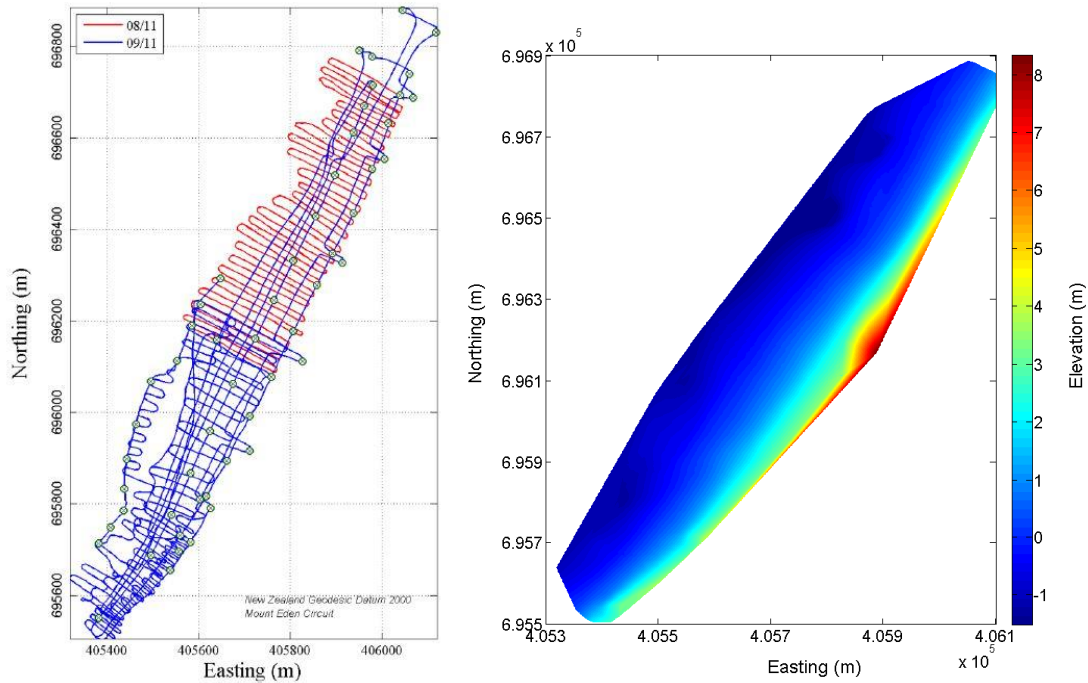


Figure 4.3 Left panel: Survey tracks (Guedes, 2010). Right panel: Surface map obtained from the beach surveys.

4.3. Methods

Rectified time-averaged images and variance images collected on the 8th of November 2010 were used to detect the groundwater seepage line (*GWSL*) and the shoreline (*SL*), respectively. Extracted shorelines were then compared with the surveyed data to evaluate the accuracy of the extracting method in both incoming and outgoing tide. In the sampling day, the tide elevation increased from -1.61 m (at 6:10 am) to 1.51 m (at 11:40 am) and then decreased to -1.59 m (at 5:40 pm). Every half an hour between 7:10 am and 3:40 pm (daylight time) a time-averaged and a variance image were collected.

4.3.1 Extracting Seepage line from time-averaged images

In order to extract the wet–dry boundary, known here as the seepage line, the RGB (Red–Green–Blue) time-averaged images (9 images during incoming tide and 9 images during outgoing tide) were converted into *HSV* (Hue–Saturation–Value–space) using the Matlab function called `rgb2hsv`. This algorithm calculates the value (V) as the maximum of the red, green, and blue intensities at each pixel (Smith, 1978). Value (V) was found to be one of the most accurate measurements, which detected the wet-dry boundary in all tested weather conditions (Huisman et al., 2011). Hence, the value was used as the threshold to differentiate between the dry and wet sand.

For each of the time-averaged images, two alongshore lines were defined (one across the ocean and one across the dry beachface). These lines force the processing software to stop searching for the groundwater outcropping points in areas that rarely include the seepage line (e.g. dune grasses or far offshore). Between these lines, the processing software extracts the value (V) in each row in the selected image with 1m space interval. The seepage line detection algorithm starts searching from the boundary line across the beach and finds the first pixel of the selected image, where the value (V) is greater than a threshold value. In this study the threshold set as 0.6. The above process was repeated for all rows of the selected image with 1m space interval between rows. Figure 4.4 shows an example of the extracting the seepage line from time-averaged images taken at Ngarunui beach. Panel A shows the variation of the Value (V) in a single row of pixels from a time-averaged image (696400 Northing in New Zealand Geodesic Datum ‘NZGD2000’). The threshold of 0.6 for the V was used to determine the location of the groundwater seepage line. This threshold was chosen by a trial and error process of extracting the seepage line from different images taken in different times during outgoing and incoming tide. It means that the seepage line can be find at a V , which is 60% of V of the dry beach and 40% of V of the sea. Panel B shows the selected pixel on the image where was considered as the groundwater outcropping point or seepage exit point.

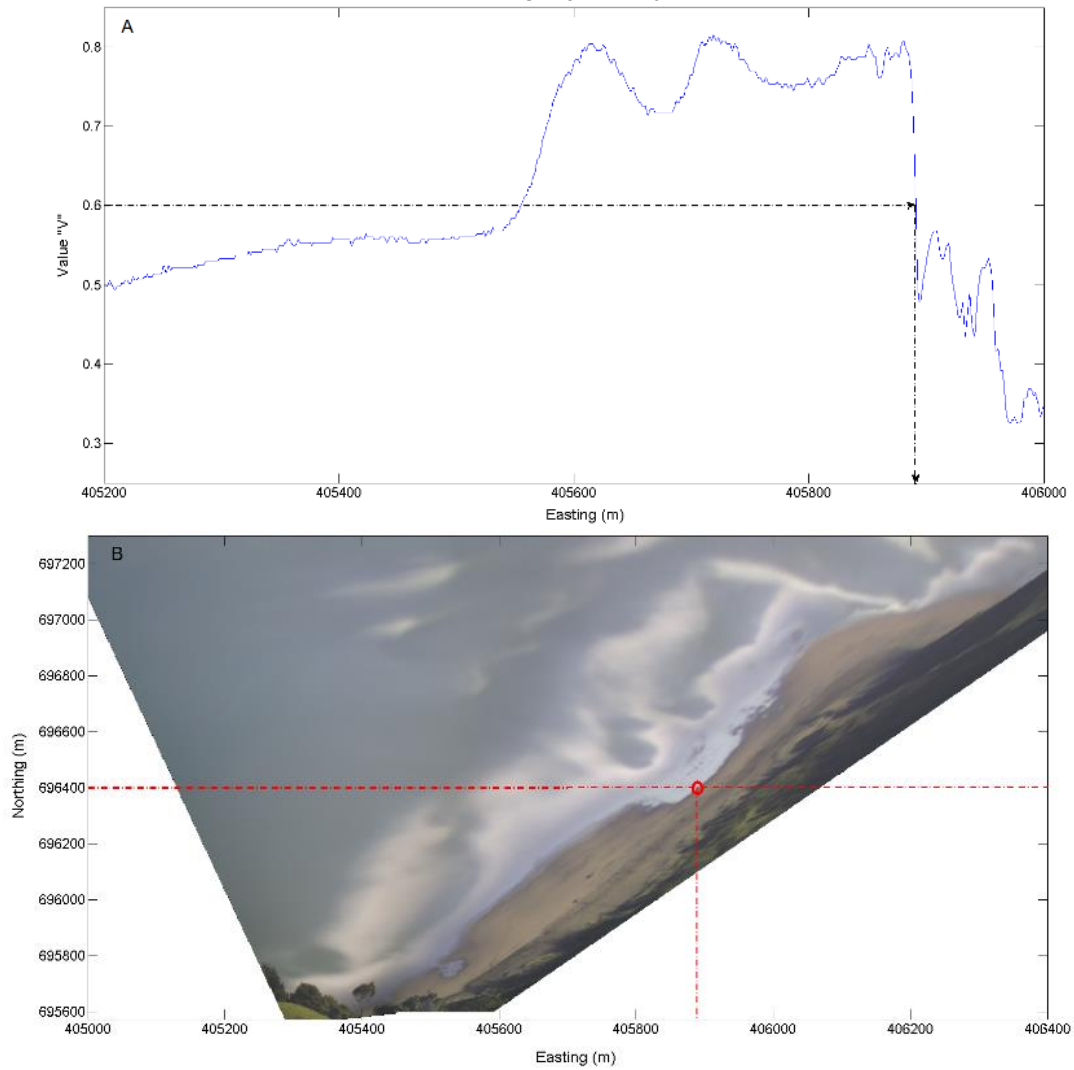


Figure 4.4 Panel A: an example of the value (V) variation in a single pixel row of a time-averaged image. The threshold used for detecting the seepage line is indicated with a horizontal black dash-dot. The vertical line shows the cross-shore location of the groundwater exit point. Panel B: a time-averaged at 7:10 am on 8th November 2010. The horizontal red dash-dot shows the selected pixel row for V variation and the circle indicates the exit point on the alongshore seepage line.

4.3.2 Extracting Shore line from Variance images

As it described in Chapter 2, the time-averaged images have been widely used to extract the shoreline. In this study the variance images were used to extract the shoreline and test the accuracy of these images in detecting shoreline in a gently sloping dissipative beach. This is because the time-averaged shoreline is not generally detectable on the background of black sand. To detect the line from the variance images, the intensity (I) was calculated as the average of the red, green, and blue pixel intensities of a RGB variance image. Intensity was found to be one of the most accurate measurements in algorithms to detect the shoreline (Plant et al., 2007).

For each of the variance images, two alongshore lines were defined, as is described in the previous Section. These lines force the processing software to stop searching for the shoreline points in areas where rarely include shoreline. Between these lines, the processing software extracts the intensity (I) in each row in the selected image with intervals of 1m spacing. The shoreline detection algorithm starts searching from the boundary line across the beach and finds the point, which intensity drops after reaching the first maximum. The above process was repeated for all pixel rows of the image. Figure 4.5 shows an example of the extracting the shoreline from a variance image taken at Ngarunui beach. Panel A shows the variation of the intensity (I) in a single row of pixels from a variance image. The threshold set as the sharp drop after the first maximum of the intensity, which is shown in this panel. Panel B shows the selected pixel on the image where was considered as the shoreline. The shoreline, which was extracted from this algorithm was considered to be the average position of the shoreline, so another shorelines can be expected more landward than this position, especially at low tide. The threshold for extracting the average position of the shoreline was obtained by a trial and error process of extracting the shoreline from different images taken in different times during outgoing and incoming tide. Although as it will be discussed in the Discussion, this threshold cannot precisely predict actual shoreline at the low tide.

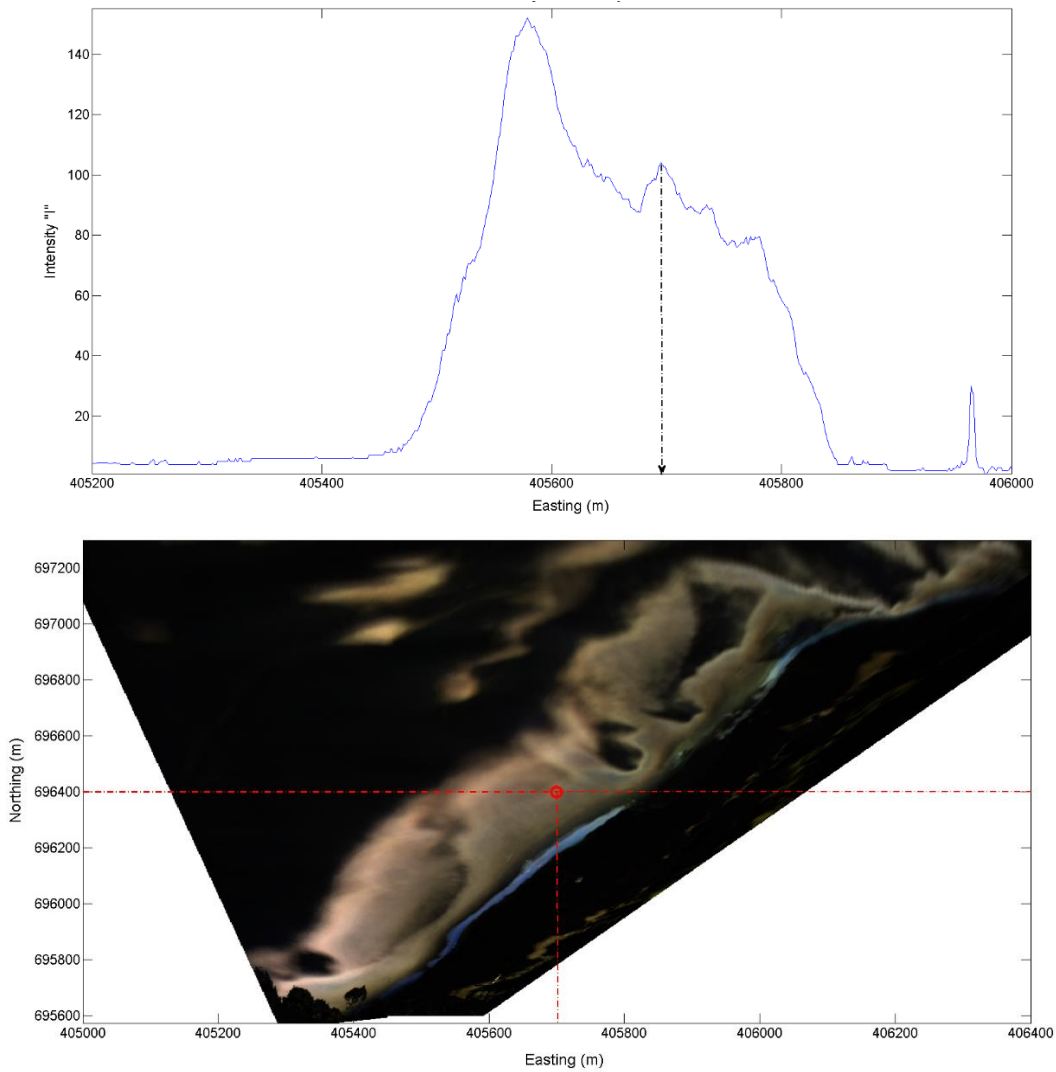


Figure 4.5 Panel A: An example of the Intensity (I) variation in a single pixel row of a variance image. The vertical dash-dot line shows the cross-shore location of the average shoreline. Panel B: variance image at 7:10 am on 8th November 2010. The horizontal red dash-dot shows the selected pixel row for I variation and the circle indicates the shoreline position.

4.4. Results

4.4.1 Groundwater seepage line detected at Ngarunui beach

The method described in Section 4.3.1 was used to extract the seepage line from time-averaged images at Ngarunui beach. In each image, the processing software extracts the groundwater seepage point in each pixel row of the image with 1m spaced intervals between rows. The results were then smoothed using a moving-average smoothing algorithm. Smoothing removes the effect of people or driftwood on the beach. This process was repeated for different images, which were provided every 30 minutes. Nine time-averaged images between 7:10 am and 11:10 am during incoming tide and nine images between 11:40 am and 3:40 pm during outgoing tide were used. Figures 4.6 and 4.7 show the time-averaged images and detected groundwater seepage lines (yellow lines) during incoming and outgoing tide on 8th November 2010 at Ngarunui beach.

Chapter 4: The Use of the Video Imagery to Extract the Groundwater Seepage Line and Shoreline at Ngarunui Beach

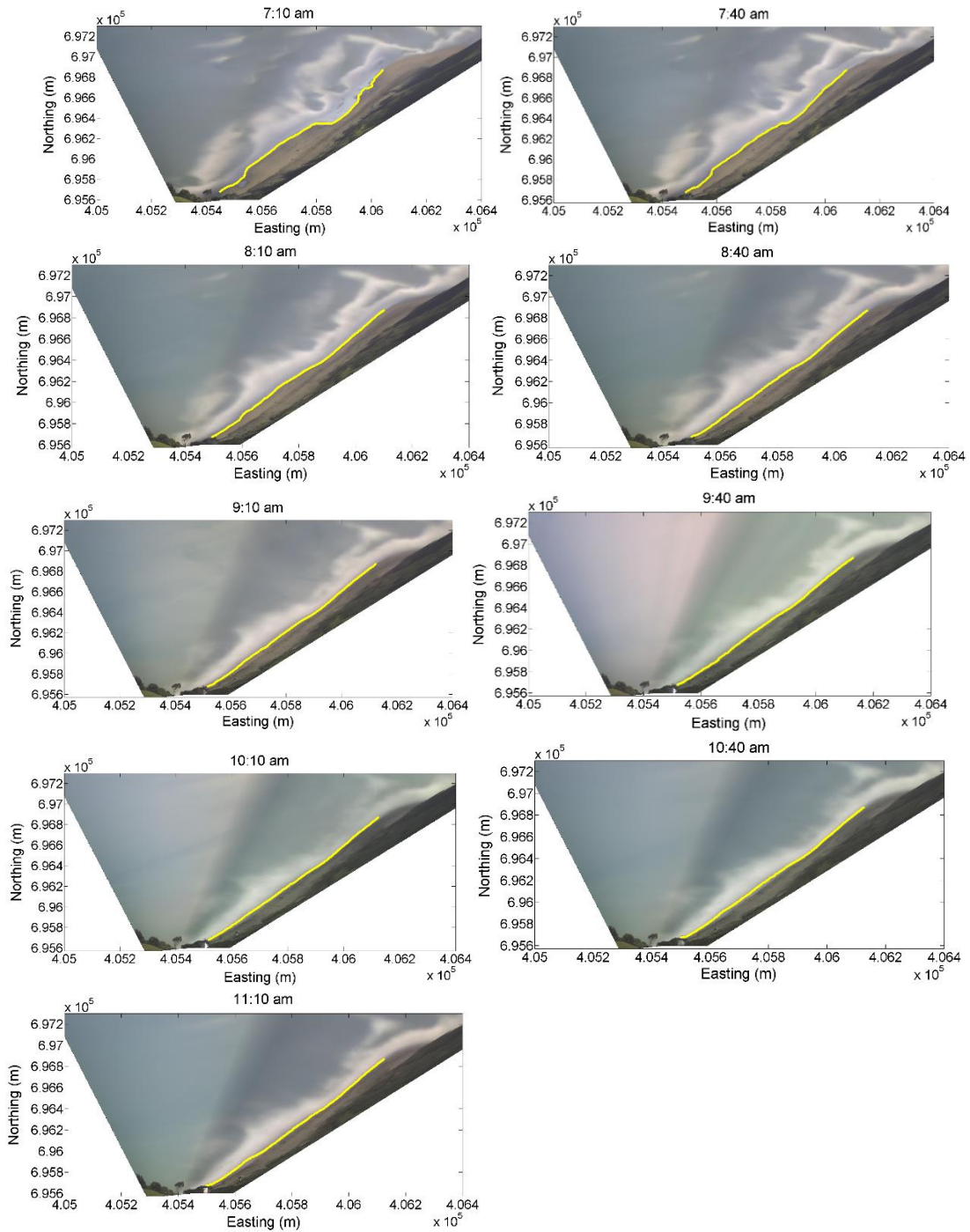


Figure 4.6 Detected groundwater seepage lines (yellow lines) from time-averaged video images at Ngarunui beach during rising tide on 08/11/2010

Chapter 4: The Use of the Video Imagery to Extract the Groundwater Seepage Line and Shoreline at Ngarunui Beach

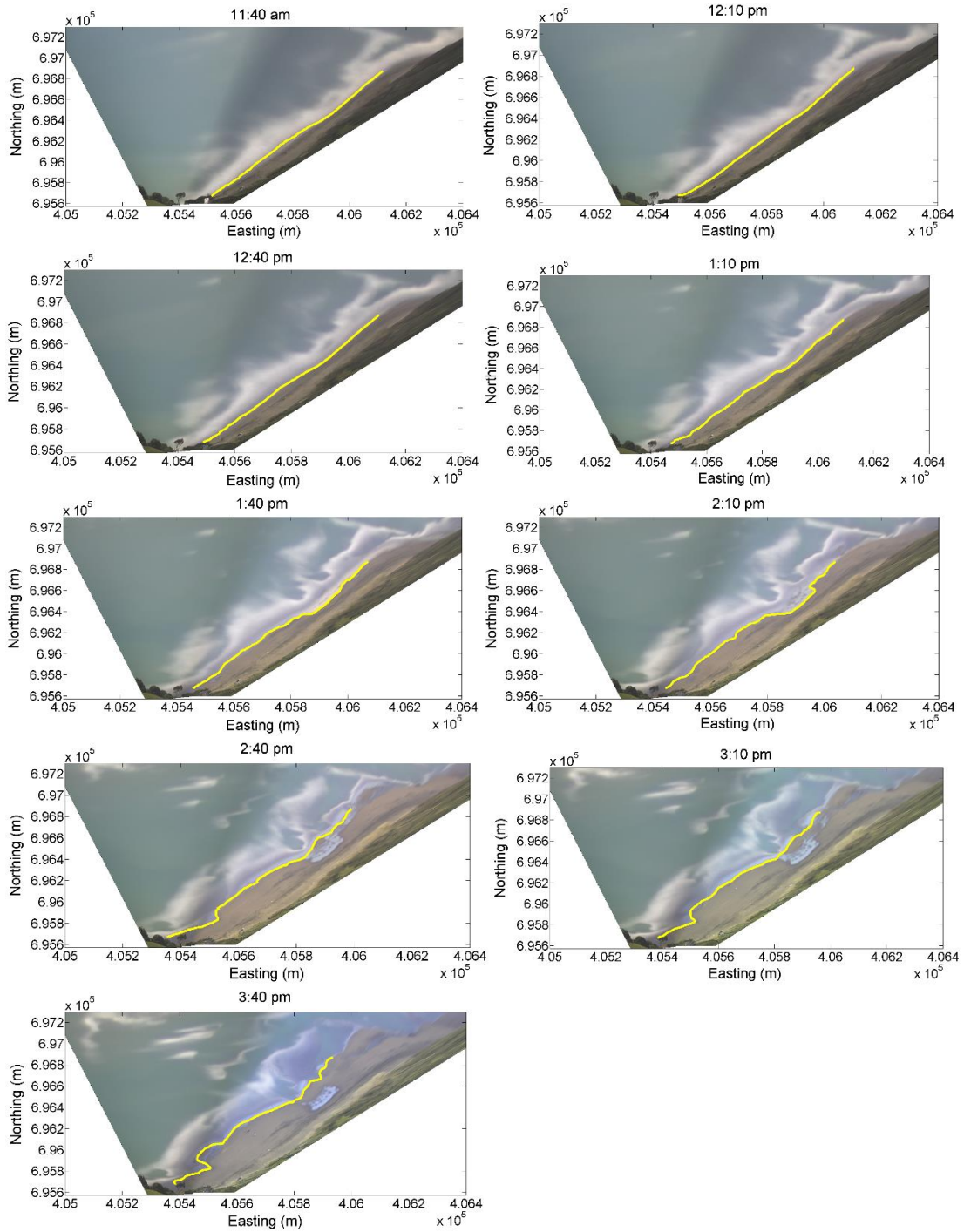


Figure 4.7 Detected groundwater seepage lines (yellow lines) from time-averaged video images at Ngarunui beach during falling tide on 08/11/2010

4.4.2 Shoreline detected at Ngarunui beach

The method described in Section 4.3.2 was used to detect the shoreline from variance images at Ngarunui beach. The results were smoothed using a moving-average smoothing algorithm. This process was repeated for different images, which were provided every 30 minutes. Nine variance images between 7:10 am and 11:10 am during incoming tide and nine variance images between 11:40 am and 3:40 pm during outgoing tide were used. Figures 4.8 and 4.9 show the variance images and detected shorelines (red lines) during incoming and outgoing tide on 8th November 2010 at Ngarunui beach.

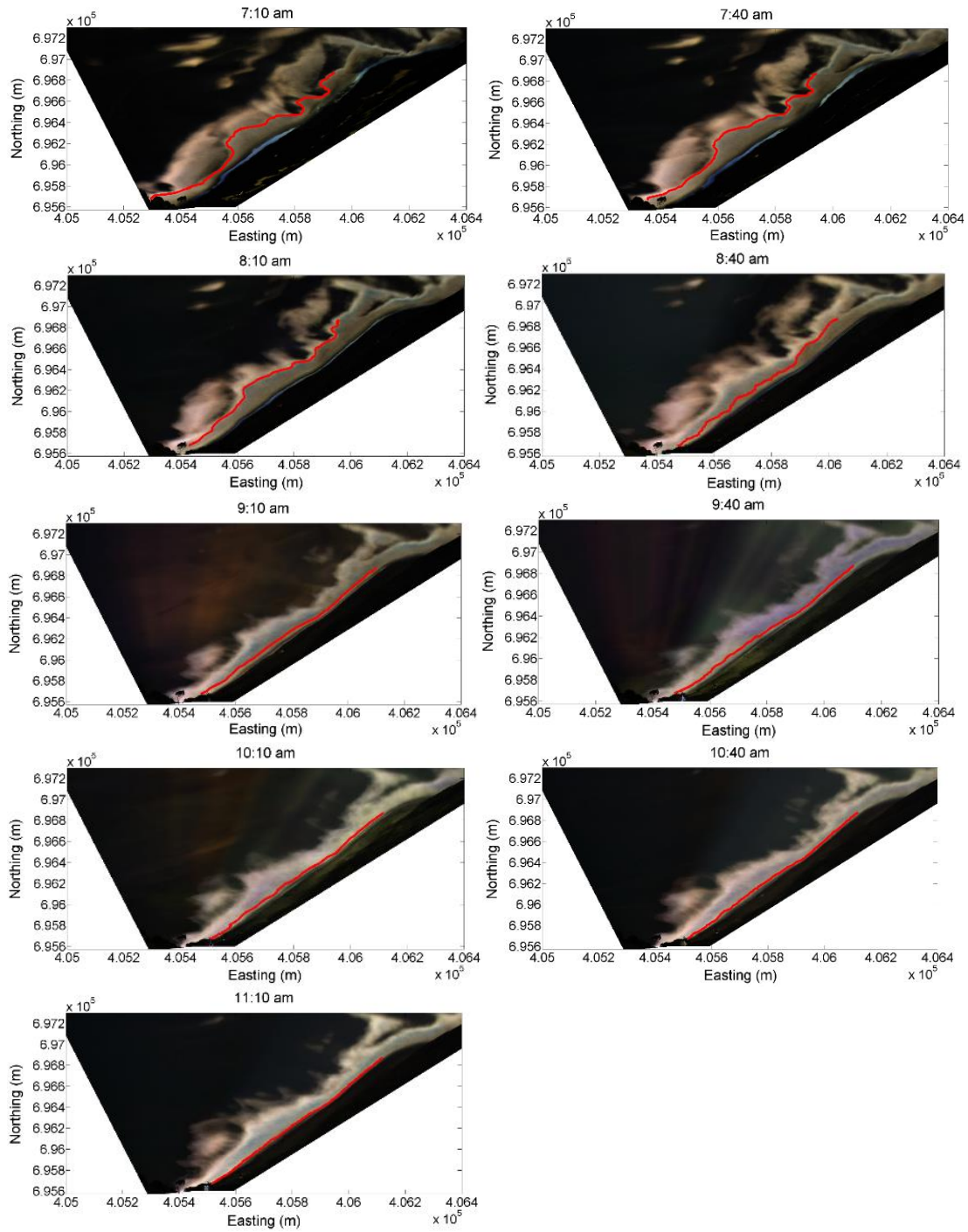


Figure 4.8 Detected shorelines (red lines) from variance video images at Ngarunui beach during rising tide on 08/11/2010

Chapter 4: The Use of the Video Imagery to Extract the Groundwater Seepage Line and Shoreline at Ngarunui Beach

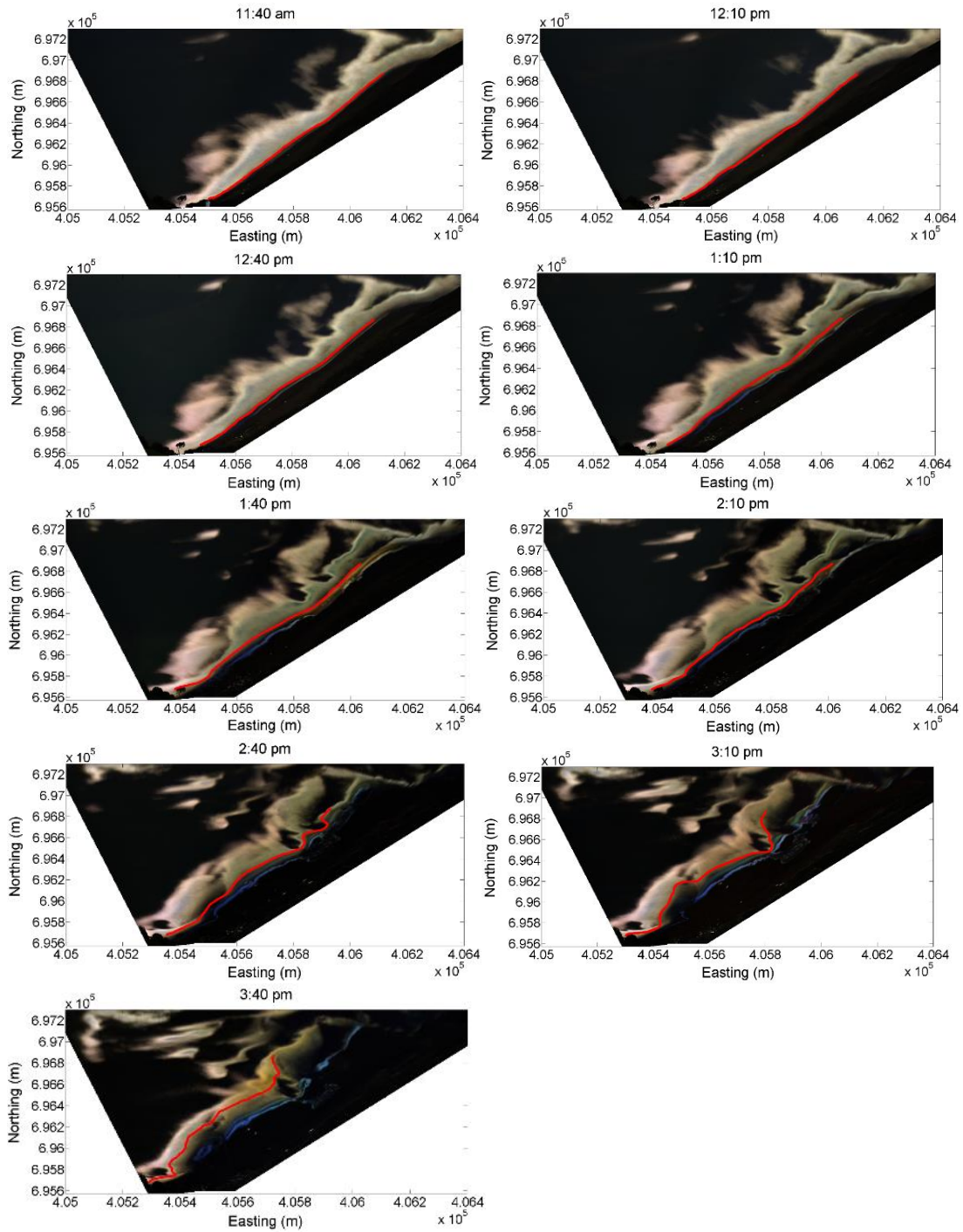


Figure 4.9 Detected shorelines (red lines) from variance video images at Ngarunui beach during falling tide on 08/11/2010

4.4.3 Decoupling between the groundwater seepage line and the shoreline

Decoupling between the shoreline and the seepage line at Ngarunui beach was studied using extracted lines from video images. Figures 4.10 and 4.11 show how the groundwater seepage line was decoupled from the shoreline during the incoming and outgoing tide respectively. According to these figures, at high tide, the groundwater seepage line was just located a few metres onshore of the shoreline (Figure 4.10 last panel and Figure 4.11 first panel). During falling tide, as the beach drains more slowly than the tide falls, the groundwater seepage face will appear between the shoreline (*SL*) and the groundwater seepage line (*GWSL*) because of the groundwater exfiltration. Around the low tide the seepage face width reaches to its maximum because of the decoupling between *SL* and *GWSL* (Figure 4.10 first panel and Figure 4.11 last panel).

The process described here was based on the seepage line extracted from time-averaged video images and shoreline extracted from variance images. In Chapter 6 of this thesis, the groundwater seepage line along the Ngarunui beach will be determined using a numerical model based on the Boussinesq equation and decoupling between the calculated seepage line and the field-based shoreline (according to the tide level at the beach) will be discussed more.

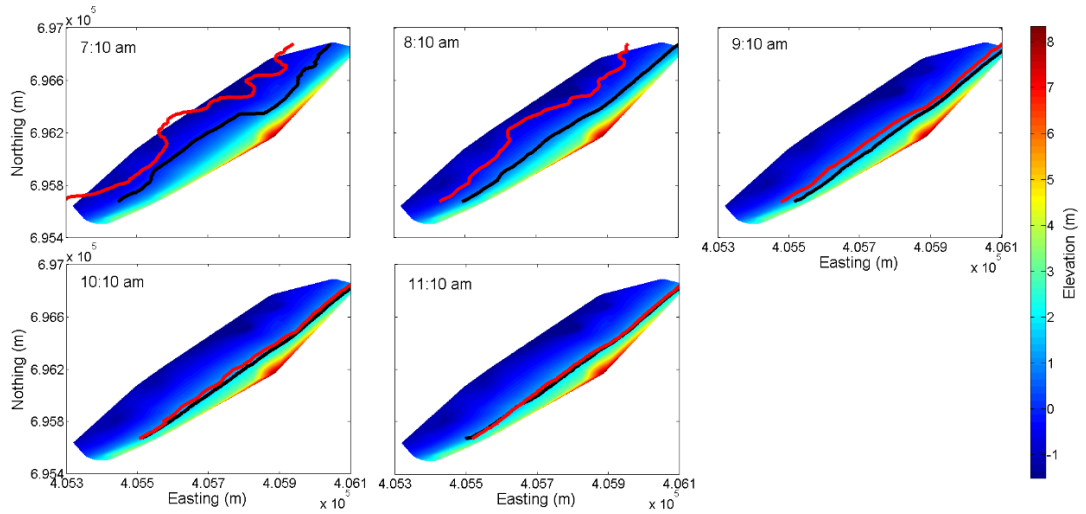


Figure 4.10 Decoupling between the groundwater seepage line extracted from time-averaged images (black line) and the shoreline detected from variance images (red line) during rising tide on 8th November 2010. The surface map obtained from the beach surveys carried out on 8th and 9th November (Guedes, 2010) is also shown in the background.

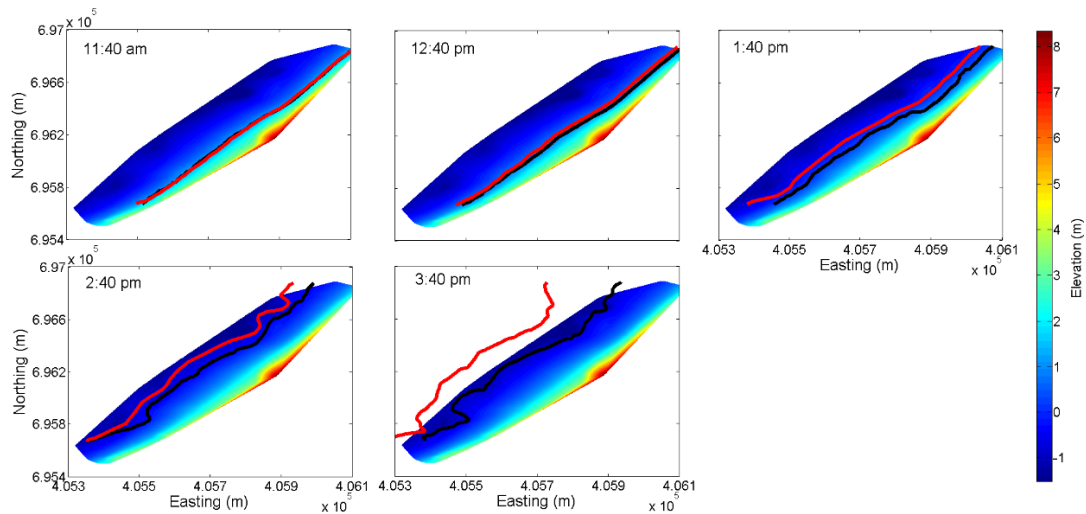


Figure 4.11 Decoupling between the groundwater seepage line extracted from time-averaged images (black line) and the shoreline detected from variance images (red line) during falling tide on 8th November 2010. The surface map obtained from the beach surveys carried out on 8th and 9th November (Guedes, 2010) is also shown in the background.

4.5. Discussion

As described in this Chapter, the groundwater seepage line can be extracted from time-averaged images using the value (V) of the *HSV* (Hue-Saturation-Value) images. Huisman et al. (2011) showed that the wet-dry boundary, which called seepage line, could be found using the time-averaged images. Although their threshold was not same as the V threshold, which I found in this study. My results showed that the seepage line was located at a pixel (on a row of an image) where V reaches to 0.6. This threshold was found by a try and error process using a wide-range of different V . Although Huisman et al. (2011) found that the threshold between 0.4 and 0.45 could be used for extracting seepage line. The threshold chosen in this study leads to more accurate seepage line rather than the threshold in previous study, according to the video images taken at the beach. For example with the threshold V of 0.4, the seepage line locates almost 80 metre landward of my chosen seepage line (Figure 4.4 A). This position is in toe of the dune (Figure 4.4 B), which is unlikely possible, because the selected image was taken almost 1.5 hours after low tide.

As described in Chapter 2 and early in this Chapter, many studies have been carried out on extracting shoreline from time-averaged images (e.g. Lippmann and Holman, 1989, 1990; Plant and Holman, 1997; Aarninkhof et al., 2003; Plant et al., 2007; Smith and Bryan, 2007; Huisman et al., 2011). These studies have mostly focused on the difference between the colour and contrast of the dry and wet sand. In this study, the use of variance images in detecting shoreline was tested. To determine the accuracy of the shoreline detecting method, the extracted shoreline was compared with the beach survey. Two surface maps were obtained using the p -colour Matlab code on detected shorelines (section 4.4.2) during the incoming and outgoing tide. Figure 4.12 (Panel A) shows the surface map obtained from the beach surveys carried out on 8th and 9th October 2010 (Guedes, 2010). Panel B and C present the calculated surfaces map based on detected shorelines during the rising tide and falling tide, respectively. Comparison between three panels show that the algorithm used in detecting shorelines from variance images is not very precise at low tide. The

elevation contours (blue areas in panels B and C) indicate that in both incoming and outgoing tide, the variance images could not work well in predicting low tide shoreline, which is consistent to the recent finding by Simarro et al. (2015). Figure 4.13 also shows the difference between the surveyed surface map and calculated surface map (based on detected shorelines) during incoming and outgoing tide. In both panels, extracted shorelines from variance images are shown. During the incoming tide, the shoreline is located mostly seaward at low tide (black thick line in Panel A) and moves landward as tide rises. Shorelines are more widely-spaced near between low tide and mid tide compared to between mid tide and high tide. This is because the intertidal beach slope is steeper in upper beach than the lower beach. In the outgoing tide (Panel B) the shoreline is located most landward (high tide shoreline at 11:40 am) and moves seaward with falling tide. The same pattern could be seen here, as tide covers narrower area in upper intertidal area rather than lower area.

The figure indicates that the beach surface, which was determined using the extracted shorelines from video images, are different from the surveyed beach. In the incoming tide (Panel A) the elevation of the calculated beach surface is lower than the surveyed beach surface in some part of the beach. The difference is as great as 0.6 m in the southern and northern parts of the beach. In the middle parts of the beach, the calculated beach surface is higher than the surveyed beach surface (up to -0.6 m). In the outgoing tide (Panel B) the calculated beach surface is always higher than the surveyed beach surface. The difference is between 0 and -1.2 m. Both panels show that the difference between the survey data and the video based data is much lower in upper intertidal beach than lower part of the beach indicating that the video extracting algorithm works better at high tide rather than low tide. The difference between the beach survey and the calculated beach surface based on the extracted shorelines could be either caused by the inaccuracy of the survey, which was carried out in 8th and 9th November 2010 or the extracting method to obtain shorelines from variance video images.

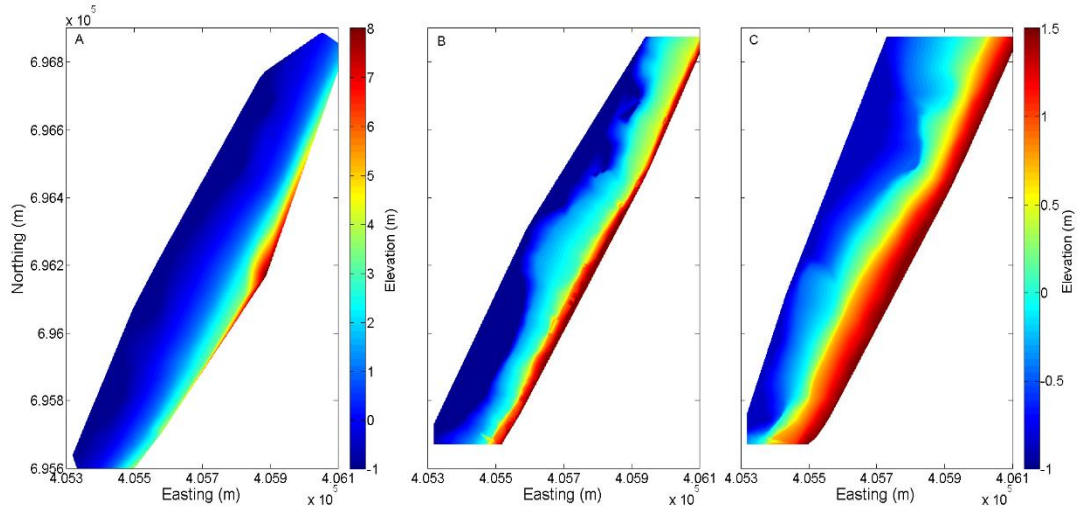


Figure 4.12 Panel A: Surface map obtained from the beach surveys. Panel B: Calculated surface map (using detected shorelines from variance images) during incoming tide. Panel C: Calculated surface map during outgoing tide.

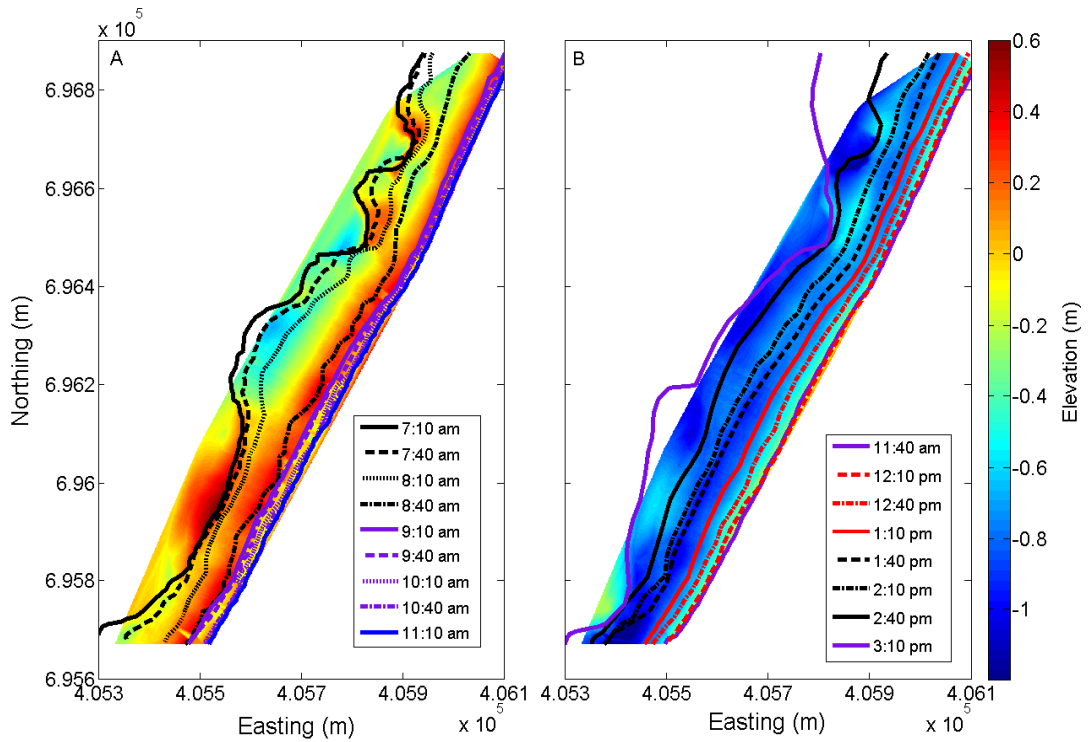


Figure 4.13 Difference between the surveyed surface map and calculated surface map (based on detected shorelines) during incoming tide (panel A) and outgoing tide (panel B). Shorelines, which were extracted from variance images every half hour, are shown in both panels.

Figure 4.14 also shows the error of the shoreline extracting method. In this figure, dots indicate the difference between the elevation of the surveyed beach and extracted shoreline in the same position. It was measured at different times between high tide and almost low tide (red for incoming tide and blue for outgoing tide). The solid lines also show the average error. The average error of shoreline extracting technique is between -0.1 and 0.25 metre in incoming tide and between -0.25 and -0.8 metre in outgoing tide. As described in Section 4.3.2, the extracted shorelines using my algorithm on variance images was considered to be the average position of the shoreline, so another shorelines can be expected more landward than this position, especially at low tide. It can be concluded that according the survey data, the algorithm of extracting shoreline from variance images could be time-dependent algorithm. It means that in a dissipative sandy beach like Ngarunui beach, the shoreline detecting method is more precise at high tide rather than low tide. Simarro et al. (2015) noted that Ngarunui Beach is an unusual case regarding it is very dissipative beach with black sand, and this situation may explain why shorelines detecting algorithm using time-averaged images did not work in all cases. They also explained that variance images were found useful to extract shoreline, but the method did not precisely work when run-up happened in the groundwater seepage face area.

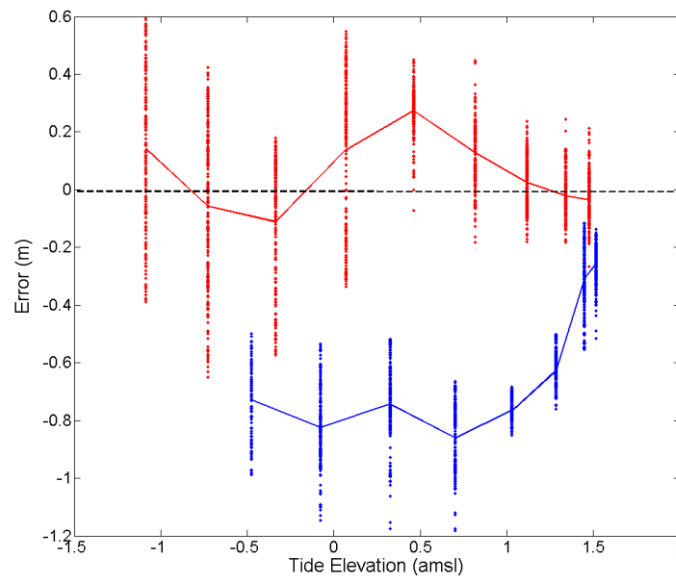


Figure 4.14 The error of the extracting shoreline method from variance video images at Ngarunui beach.

Decoupling between the beach groundwater seepage line (*GWSL*) and shoreline (*SL*) was studied carefully using the extracted *GWSLs* from time-averaged images and the detected *SLs* from variance images taken at Ngarunui Beach. During rising tide, the infiltration from the tidal wave causes the water table rise, although beach groundwater level increases much more quickly than rising tide. Comparing panels of figure 4.10 already indicate that it happens in Ngarunui beach, however in the next Chapter this issue will be tested using groundwater level recorded by Solinst piezometers deployed in the beach. This may causes the groundwater seepage line decouples from the shoreline more quickly on the lower part (less steep intertidal beachface) rather than the steeper upper part of the beach profile (Figure 4.10). On high tide, there is not much decoupling between the groundwater seepage line and the shoreline, which supports previous studies (e.g. Li et al., 1997; Turner, 1998; Huisman et al., 2011). In this case, the groundwater seepage line is located a few metres onshore of the shoreline. During falling tide, the groundwater seepage line starts to decouple again from the shoreline. As the beach drains more slowly than the tide falls, the groundwater seepage face appears between the *SL* and the *GWSL* because of the groundwater exfiltration. Same as the incoming tide, in the outgoing tide, groundwater seepage line decouples from the shoreline more slowly on the upper part (steeper intertidal beachface) rather than the less steep lower part of the beachface (Figure 4.11). This decoupling process shows that Ngarunui Beach fills more rapidly than tide rise and drains more slowly than tide falls. As it mentioned, this issue was studied precisely using my field data collected from the Solinst piezometers, and manual water detectors at Ngarunui Beach in September 2013 (next Chapter).

Another important finding of this study is how the seepage face (*SF*) width is greater or less along the beach. Figure 4.15 shows the *GWSL* extracted from time-averaged images and *SL* detected from variance images at 7:10 am (1.5 hours after the low tide) and 11:10 (almost at high tide). The left panel show the decoupling between *GWSL* and *SL* 1.5 hours after the low tide. It clearly presents that the seepage face width is much greater in north and middle of the beach rather than south part. The field work carried out in September 2013, which is explained in the next Chapter,

helped to understand the alongshore variation of the groundwater seepage line. The study area is shown in the panels. As it will be described in Chapter 5, three transects was chosen to study the groundwater level and wave data using different instruments. The first transect in north, the second in the middle and the third transect in the south of the study area are also shown in Figure 4.15. Figure 4.16 also shows photo taken at Ngarunui Beach at low tide. The lower panel shows that the southern part of the beach (left side of the photo) has much less seepage face width rather than the north part.

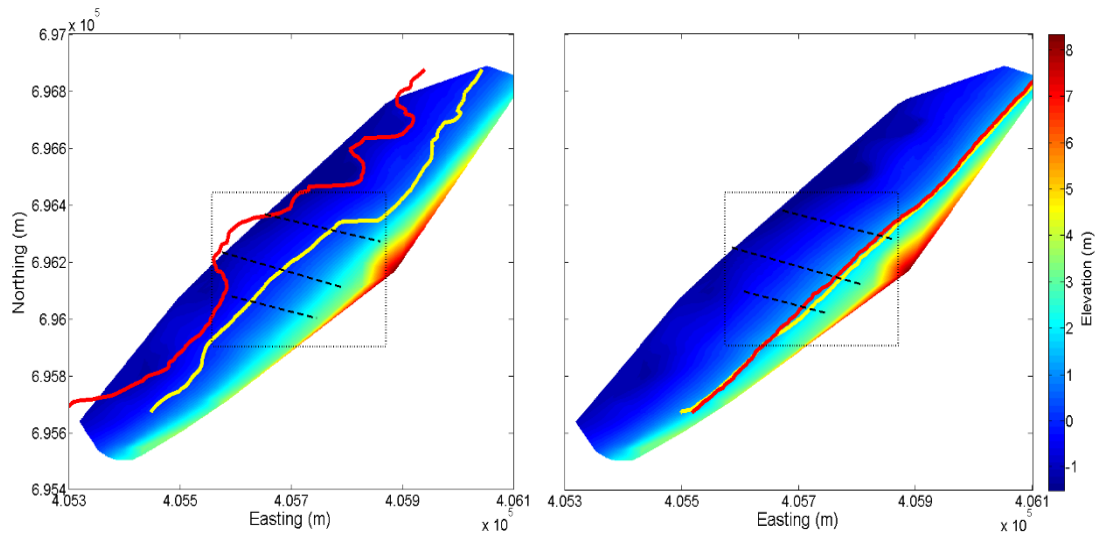


Figure 4.15 Decoupling between GWSL extracted from time-averaged images and SL detected from variance images (left panel at low tide and right panel at high tide). The rectangular shows the study area for the field work and dash lines indicate three transects (Chapter 5).

According to the field data, the beach hydraulic conductivity is much higher in the south than the middle and north of the study area. The intertidal beachface is also steeper in south than other parts of the beach (Chapter 5). A steeper beach profile and higher hydraulic conductivity are two important factors in decreasing the groundwater exit point elevation and shortening the seepage face width across the south of the beach (As it described in Chapter 3 and will be explained more in

Chapter 6). Transect 3 in south of the beach located in the part of the beach with rip currents. The rips can be seen in time-averaged images (e.g. Figure 4.4). The rip current in south of the beach may have an effect on lowering the groundwater exit point and shortening the seepage face width.

The decoupling between the *GWSL* and *SL* will be discussed more in Chapters 6 using the field data (Chapter 5) and a numerical model based on the two-dimensional linear and non-linear Boussinesq equation.



Figure 4.16 Photo taken on 15th August 2015 at 4pm (at low tide) at Ngarunui Beach. Upper panel shows a panorama view of the beach. Lower panel shows the study area.

Chapter 5 : Ngarunui Beach Field Data Collection

5.1 Introduction

This Chapter describes three days fieldwork carried out in Ngarunui beach in September 2013. This work included a beach survey, groundwater seepage line survey, beach groundwater measurements, groundwater table measurement behind the beach dune and wave data collection in the swash zone. Beach survey data and groundwater measurements were used as input data to the numerical model (next Chapter). Beach seepage line observations were also used for numerical model calibration and to compare with model results.

As it described in the first Chapter, Ngarunui beach is a dissipative beach, located near Raglan on the North Island. The study area is a part of the beach located 200 m north-east of the Raglan surf club and extended approximately 400 m in alongshore direction. Three transects, which are almost 150 m apart from each other were defined along the beach (Figure 5.1).

Transect T1 (northern), T2 and T3 (southern) are represented by the green, red and blue lines respectively in Figure 5.1. On 17th September 2013, two Solinst piezometers were deployed in each transect. These two piezometers (*SHT*, and *SLT* in Figure 5.1) were located at the high and low tide positions and measured the variation of beach groundwater elevation automatically every 10 seconds for 48 hours. On 18th September, manual groundwater measuring was done using dipwells located between high tide and low tide Solinst piezometers. Furthermore, to obtain the wave height and direction, three *ADV*s were deployed in the swash zone (black dots in Figure 5.1). To predict the long term variation of the water table, the *ISD* station, which consisted of a piezometer buried behind the dune, was also used. Figure (5.2) shows a profile schematic of the cross-shore transect and deployed instruments.

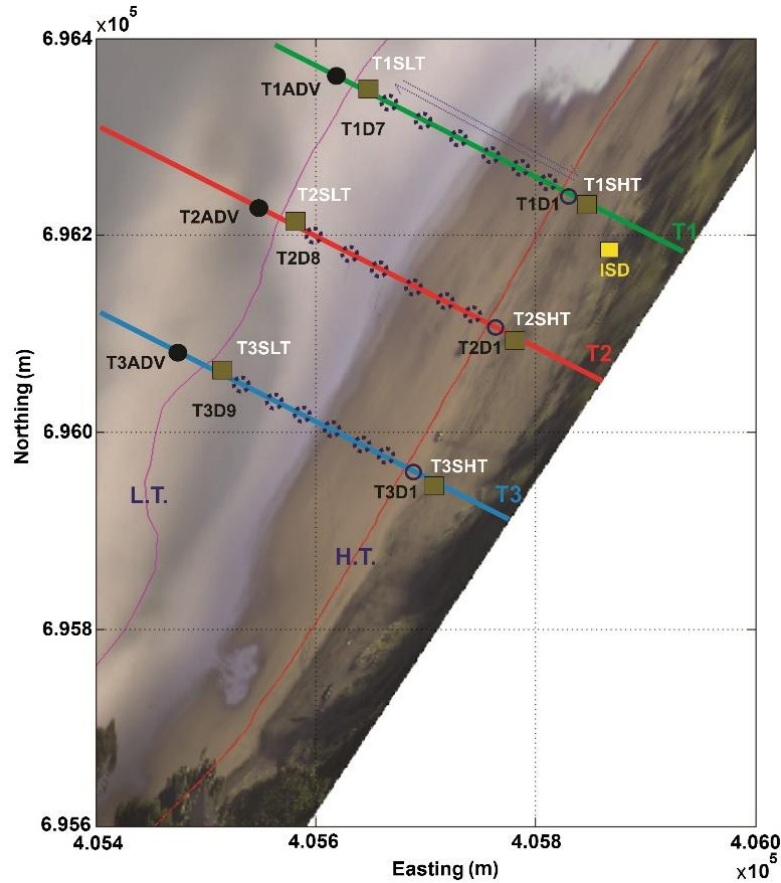


Figure 5.1 Upper panel: Studied area on the rectified time-averaged image. High tide and low tide Solinst piezometers are shown with squares (e.g. T1SHT, T1SLT). Circles and dashed circles show dipwells (e.g. T1D1, ..., T1D7). Black circles indicate ADVs (e.g. T1ADV). Yellow square shows the ISD station. Three cross-shore transects (T1, T2 and T3) and approximate shoreline at high tide and low tide are also shown. Lower panel: photo taken in Ngarunui beach, showing three transects (from right to left: T1, T2 and T3).

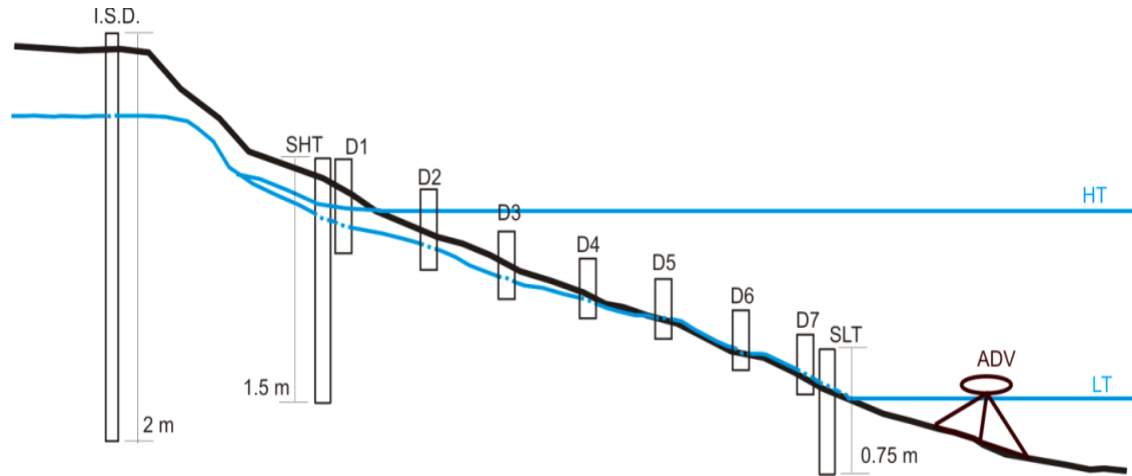


Figure 5.2 A schematic cross-shore transect showing the relative position of deployed instruments along each of the 3 transects. ISD: long-term water table recorder (only one ISD behind the dune). SHT: The high tide Solinst piezometer, which was a piezometer located at high tide, measuring short-time beach groundwater variations). SLT: The low tide Solinst piezometer, which was a piezometer located at low tide. ADV: The Acoustic Doppler Velocimeter, which was a device deployed in swash zone for measuring wave characteristics. D1, 2, etc: Dipwells for manual groundwater detection.

5.2 Field data

5.2.1 Survey data

The beach survey was carried out on 18th and 19th September 2013 using GPS laser scanner. An alongshore distance of almost 400 m was surveyed. Alongshore surveyed lines were 20 m apart and they covered the area between dune edges and the shoreline. Cross-shore surveyed lines were approximately 20 to 25 m apart and covered the area of three transects (Figure 5.3). The groundwater seepage line was surveyed four times on Wednesday 18th and Thursday 19th, between mid tide and low tide, using a GPS laser scanner (Figure 5.4). The survey data were then rotated anti-clockwise to convert the data from the northing-easting to alongshore-cross-shore system. Some of the photos taken in 18th and 19th September 2013, when the full beach survey and *GWSL* detecting were done, are shown in the Appendix A-1.

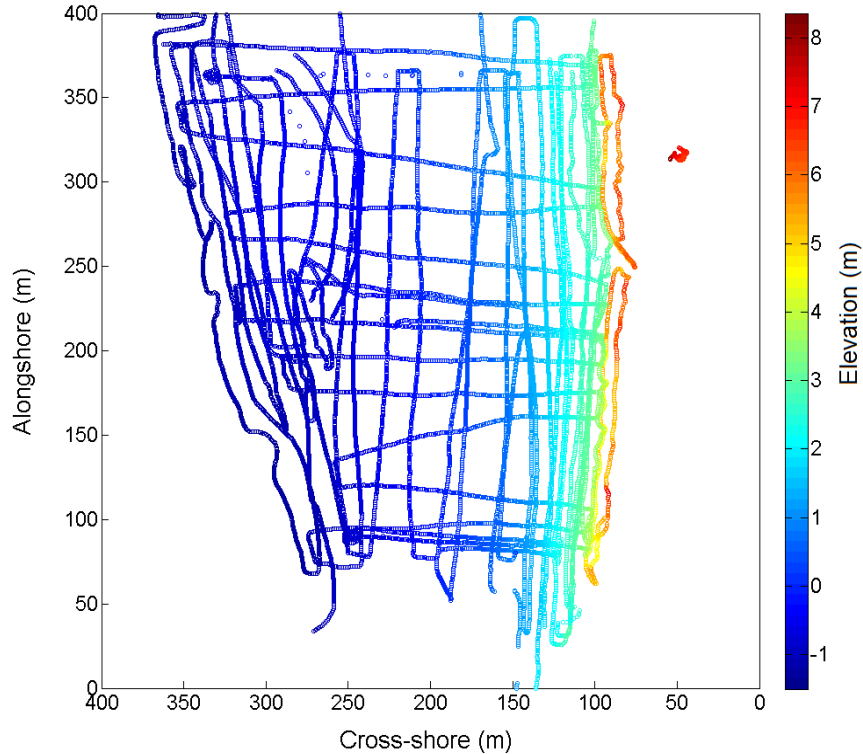


Figure 5.3 Survey data from Ngarunui Beach, 18 and 19 September 2013

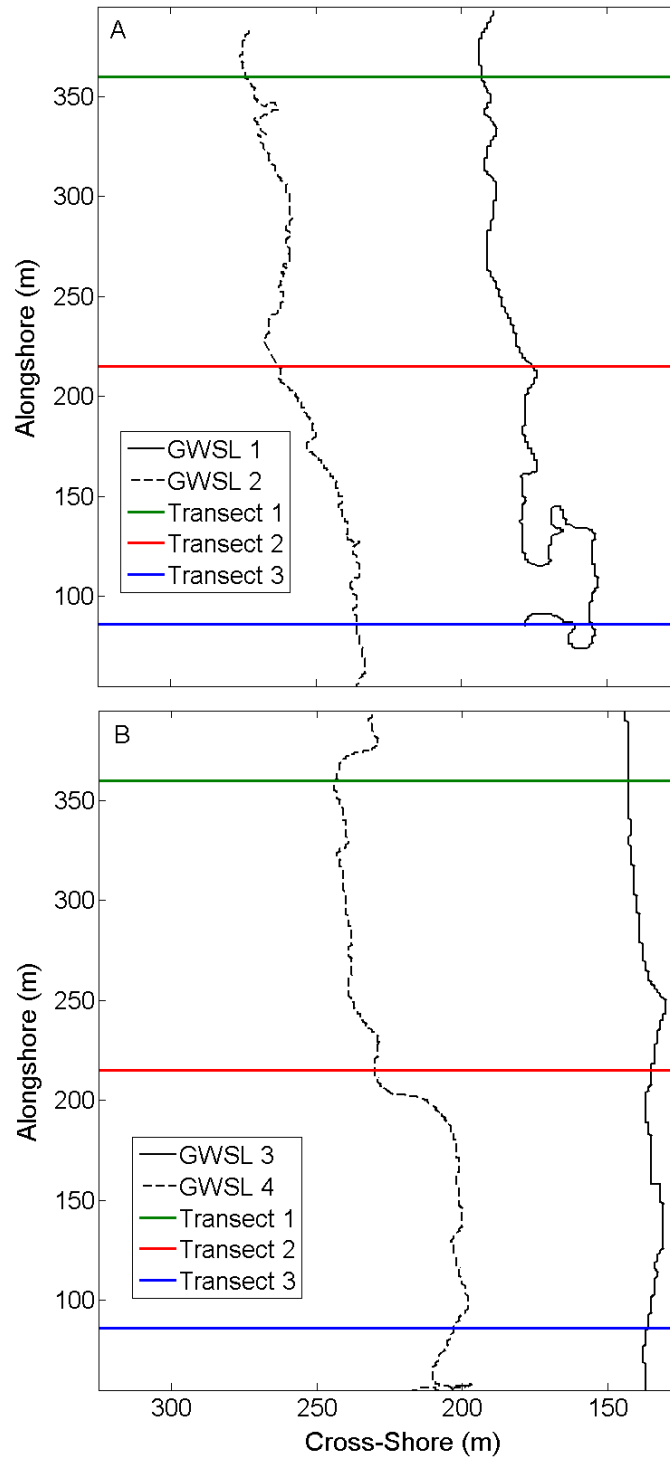


Figure 5.4 Panel A: surveyed groundwater seepage line (GWSL) from 18th September 2013 at 11:35 am (mid tide) and 12:25 pm (1 hour after mid tide) (GWSL 1, and 2). Panel B: GWSL on 19th September at 10:45 am (1.5 hour after high tide) and 01:10 pm (1 hour after mid tide) (GWSL 3, and 4)

5.2.2 Sediment sampling and hydraulic conductivity

Sediment samples were collected on 18th September at Ngarunui Beach. Eight samples were collected along each transect. Samples were analyzed in the laboratory for particle distribution (using a Malvern mastersizer) from which porosity and hydraulic conductivity were calculated. Hydraulic conductivity was obtained using Kozeny-Carman formula (1956). This equation is one of the most widely accepted estimations for hydraulic conductivity of medium sands with average grain sizes of less than 3 mm (Odong, 2007).

$$K = \left(\frac{\rho \cdot g}{\mu} \right) \left[\frac{n^3}{(1-n)^2} \right] \left(\frac{d_{10}^2}{180} \right) \quad (\text{Eq. 5.1})$$

where, ρ is flow density, g is gravity acceleration, μ is dynamic viscosity and d_{10} is the grain diameter for which 10% of the sample is finer, respectively. Porosity (n) was also calculated from Vukovic and Soro (1992) (Odong, 2007) (Eq. 3.4b).

Although the chosen hydraulic conductivity in Muriwai Beach was calculated based on the Krumbein and Monk formula (1942) (Eq. 3.4a) (estimated by Robinson, 2004), in Ngarunui Beach the Kozeny-Carman formula (1956) (Eq. 5.1) was used to calculate the hydraulic conductivity in the dune and the beachface. The estimated hydraulic conductivity by Krumbein and Monk formula has shown to be ineffective especially in dune sands. In the other hand, Kozeny-Carman formula works well in estimating the hydraulic conductivity in both beachface and dune sands (Lopez et al., 2015). The value of K estimated by Equation 5.1 was then applied in the numerical model to obtain the groundwater profile starting under beach dune and outcropping the beachface.

Figure 5.5 shows three transect profiles and the variation of the hydraulic conductivity in each of them. It shows that in Ngarunui beach the sediment permeability of the lower beachface is always bigger than permeability of the upper beachface and dunes. Furthermore, south of the beach (indicated with transect 3) generally has much greater hydraulic conductivity than the middle and north of the beach.

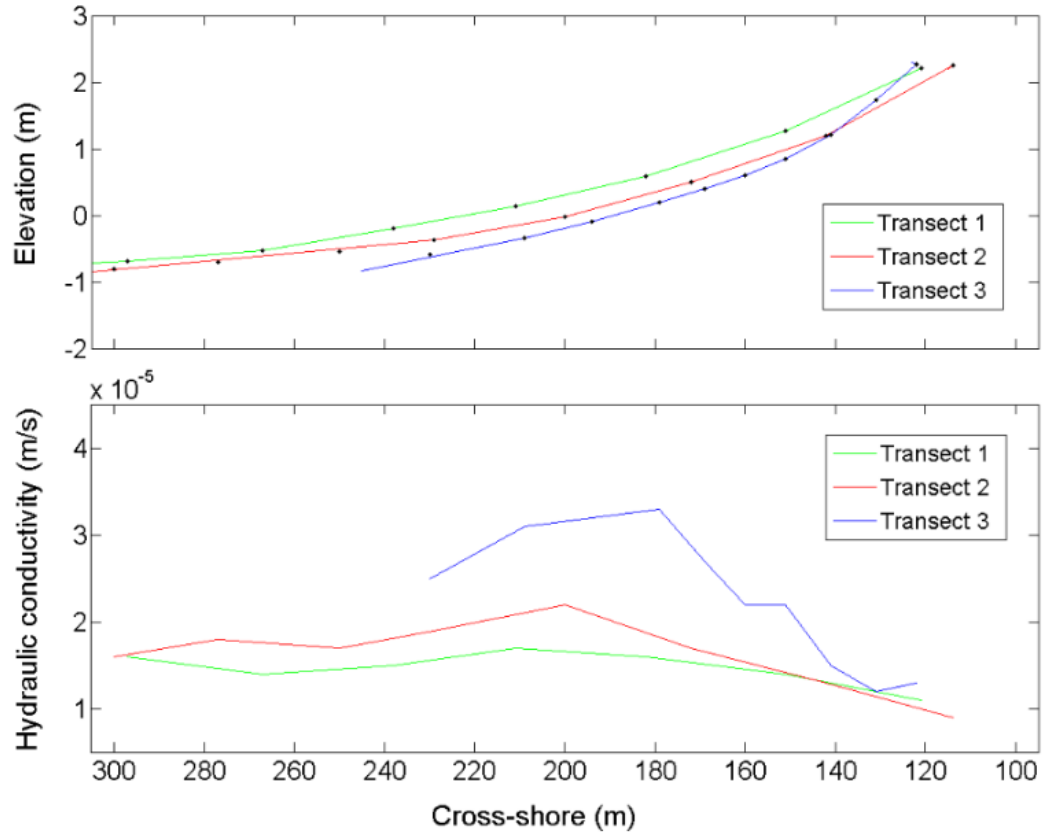


Figure 5.5 Upper panel: location of sediment samples along the three transects. Lower panel: sediment hydraulic conductivity variation along the three transects.

5.3 Methods, instrument data and results

5.3.1 ISD deployment and long-term water table variation

The ISD station was situated in the swale behind the dune, near the first transect (Figure 5.1, upper panel). The location was selected in order to minimize the effect of tidal and wave variations on groundwater measurements, and so should only measure the effects of passing weather patterns. The station consisted of a two metre tube with a sensor at the bottom connected to ISD logging station. Some of the photos taken from 27th August and 4th September 2013 during the ISD deployment are shown in the Appendix A-2. The ISD station recorded the water table over three months (September, October and November 2013) providing the longer-term variation of the water table needed to contextualize the experiment. Figure 5.6 shows that the beach water table ranged between 4.6 and 5.3 metres. The graph shows that when the water level is above 5.1 m, the behaviour of the following rainfall is different than when it is below 5.1 m. So at lower levels of the water table, there is a rapid rise in water level during a rain event. When the rain stops, the water drain away through the ground, producing a characteristic hydrograph curve rapidly rising leading edge and exponentially decaying trailing edge. However, at high water table levels, the rain cannot infiltrate into the ground and floods the swale. If there is sufficient water, it breaches the low point at the far end of the picture, forming a channel to the beach and rapidly draining off the surface water. Due to wind blown sand, the channel gets blocked up again. So there is a rapidly rising leading edge as the rain falls. This continues to rise as the surface floods, and then there is a rapid fall when the channel forms and drains the surface water away. Then the ISD records the exponential decay as the ground water drains through the dune to the beach.

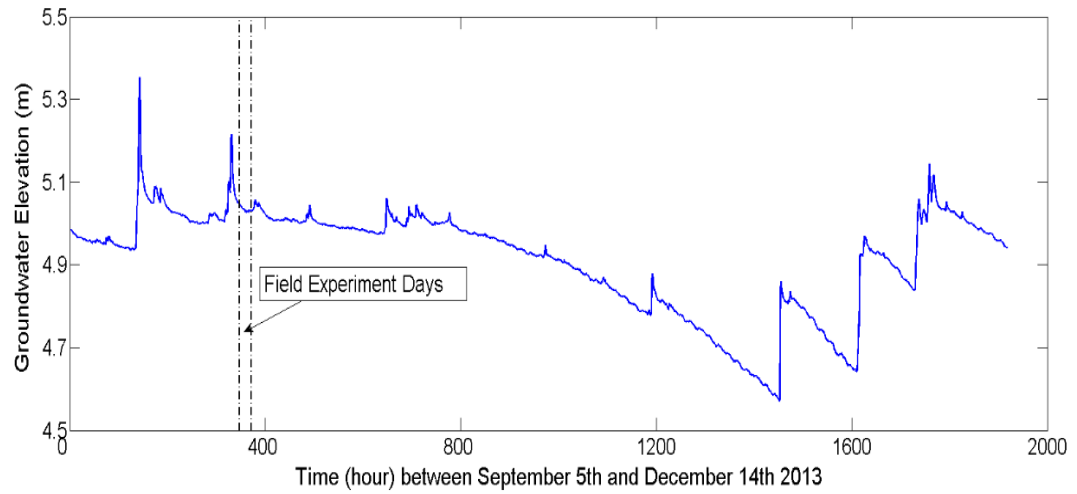


Figure 5.6 Water table variation on Ngarunui Beach during the 3 month time period.

5.3.2 Solinst piezometers deployment and short-term beach groundwater variation

As described in Section 5.1, three cross-shore transects were defined in the studied area. Along each transect, two Solinst piezometers were deployed (one at the elevation of the high tide, named *SHT*, and one at the elevation of the low tide named *SLT*, Figure 5.1). On the 17th September, holes were dug at the deployment locations within which 150 cm and 75 cm length tubes were placed at *SHT* and *SLT* respectively, at the bottom of which the sensors were placed. Some of the photos taken from piezometers deployment are presented in Appendix A-3.

These six piezometers recorded the beach groundwater variation between 18th September at 00:00 and 19th at 16:00. The time interval of recording was 10 seconds, giving 14,400 groundwater values over 40 hours for each piezometer. Raw piezometers data were then converted the water table depth using the simple formulas:

$$D = L - E - X \quad (\text{Eq. 5.2a})$$

$$E = El_1 - El_2 \quad (\text{Eq. 5.2b})$$

$$X = X_1 - X_2 \quad (\text{Eq. 5.2c})$$

$$GW_{El.} = El_2 - D \quad (\text{Eq. 5.2d})$$

where string length (L), the beach surface elevation (El_2), the elevation of top of the tube (El_1) were measured. The barometric pressure (X_2) was measured at the site using the sampling interval as the piezometer data (X_1). Using these data, the groundwater depth (D) and consequently the groundwater elevation of mean sea level ($GW_{El.}$) were calculated every 10 seconds for a 40 hour time period. Figure 5.7 shows the schematic of the piezometer deployed in the beach. Figure 5.8 shows the groundwater variation recorded by the three high tide and two low tide piezometers. Unfortunately the low tide piezometers in the third transect failed to record, because of sand infiltrating the pipe.

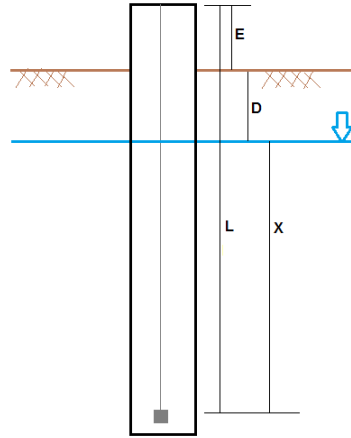


Figure 5.7 Schematic of the Solinst piezometer deployed in Ngarunui Beach. The brown line is the beach surface and the blue line represents the water table. Symbols are the same as used in Eq. 5.2.

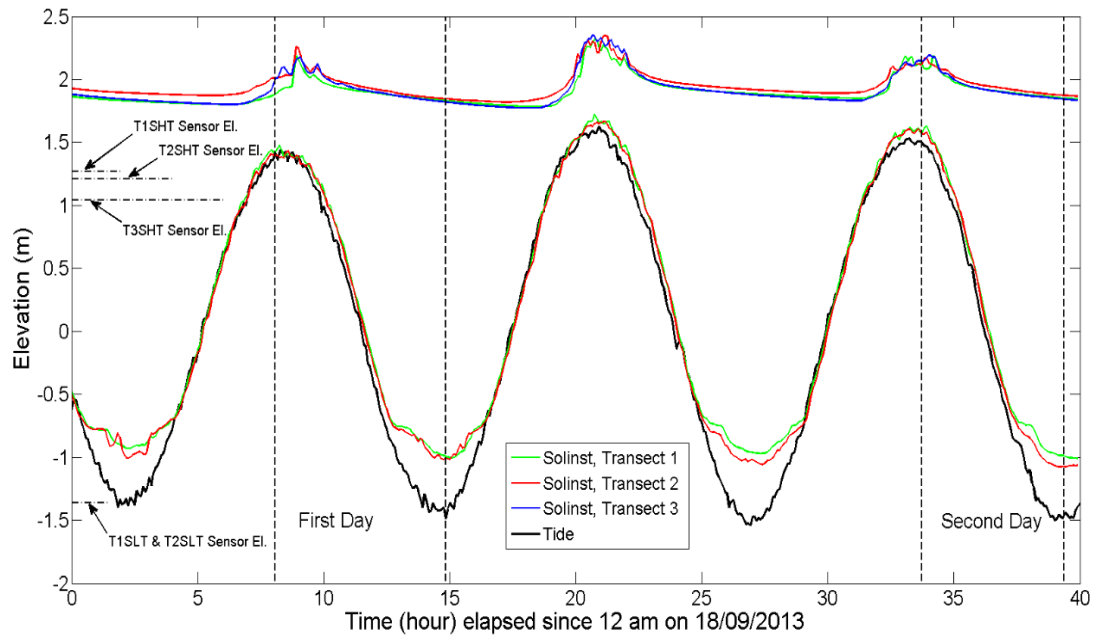


Figure 5.8 Short-term beach groundwater variation measured by the Solinst piezometers. The three upper lines represent measurements from the high tide locations on each transect (T1SHT, T2SHT, and T3SHT) and the two lower lines show measurements at the low tide locations (T1SLT and T2SLT). The thicker black line shows tide variation. The daylight hours during the experiment (18 and 19th September 2013) are indicated in the figure.

5.3.3 Dipwells and manual beach groundwater level detecting

During the outgoing tide in both days, the groundwater level was measured manually using water detectors lowered into the dipwells. After high tide, the groundwater level was measured following the tide seaward so that the number of sampling points and their spatial coverage seaward increased with time). In Appendix A-4 photos of measuring beach groundwater level within the dipwells and their location are shown.

Figure 5.9 shows the location of dipwells in both Northing-Easting coordinate system (GPS laser scanner coordinates) and alongshore-cross shore system (rotated coordinate system). Measured groundwater elevation in dipwells are also presented in this figure. The dipwell data was then applied to calibrate the numerical model (next Chapter) using comparison between the calculated groundwater profiles and the measuring data.

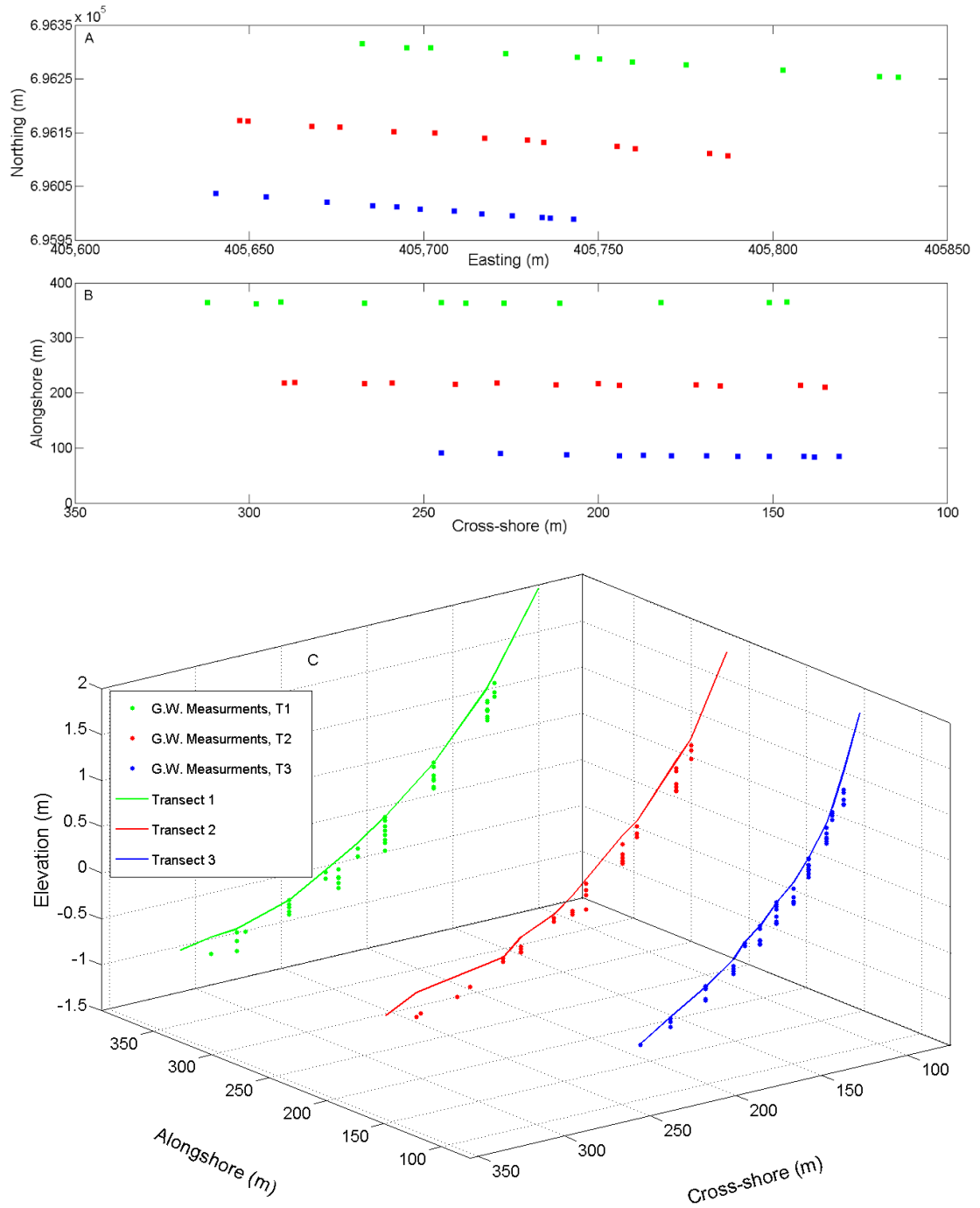


Figure 5.9 Panels A and B: the location of dipwells along three transects in Northing-Easting and alongshore-cross shore coordinate systems. Panel C: groundwater elevation measured in dipwells during the falling tide. The lines represent the beach surface elevation.

5.3.4 ADV deployment and wave data

Along each transect, an Acoustic Doppler Velocimeter (*ADV*) was deployed in the swash zone. The *ADV* was placed a few metres offshore of the low tide Solinst piezometer (*SLT*). Installing *ADV*s along the three transects was difficult as the *ADV* was placed in the low tide area and the time when this part of the beach was not covered by waves and swash was limited. For installing the *ADV*, a hole was dug close to the *SLT* in each transect. A tube was then inserted into the hole to prevent wet sand entering the hole. The *ADV* and its metal frame were inserted and the surrounding tube was removed. To ensure the stability of the frame, it was secured by four anchors with strong metal chains (~3-4m) extending outwards from the arms of the frame. The chains and anchors were then buried Appendix A-5 shows photos of the installation.

The three *ADV*s recorded wave data between 17th September at 2 pm and 19th September at 4 pm, giving 50 hours continuous data. The *ADV*s' average interval sampling (Burst) was set to 30 minutes giving 100 bursts in total. Within each burst, the *ADV*s recorded the wave-induced velocity in alongshore and cross shore directions (U_w and V_w) and pressure (P) for 20 minutes. It did not record any data for the rest of the time (10 minutes). Sampling frequency was set to 4 Hz giving 4800 samples (P , U_w , and V_w) in each burst. Furthermore, mean pressure and average of velocities were calculated each burst.

Figures 5.10, 5.11 and 5.12 show an example of the wave data measured by *ADV*s along transects 1, 2 and 3 respectively at high tide and around mid-tide. In these figures panel A shows the water depth variation over 20 minutes of *ADV* recording during one burst. It changes between 1.2 and 2.2 metres (above mean sea level) at high tide in all transects, however transect 1 has higher elevation than 2 and transect 2 is slightly higher than 3. Panel B shows that wave-induced velocities varies between -100 and 100 cm/s approximately. Panel C shows that the cross-shore wave-induced velocity (U_w) is generally greater than alongshore velocity (V_w) in transect 1 and smaller than V_w in transects 2. In transect 3 they almost vary in the same range. It

indicates that wave is faster and stronger in cross-shore direction in the first transect, while in the second transects, the wave-induced velocity is much bigger in alongshore direction. The different shapes of dot clouds (Figures 5.10-5.12 Panel C) could be caused by the different orientation of the shoreline with respect to the incoming wave. Unfortunately the rectified image (Figure 5.1) does not provide sufficient information for describing this issue.

To show how power of the wave signal is distributed over the different frequencies, the power spectral density (*PSD*) of the wave was studied. *PSD* was obtained using autocorrelation function in Fourier series of the wave signal (the square of the Fourier transform module, divided by the integration time). *PSD* describes at which frequencies wave energy dominates and at which frequencies it is less important. Panel D (of figures 5.10.1, 5.11.1 and 5.12.1) show that the wave is always much stronger in low frequencies (less than 0.2 Hz) than high frequencies (bigger than 0.2 Hz).

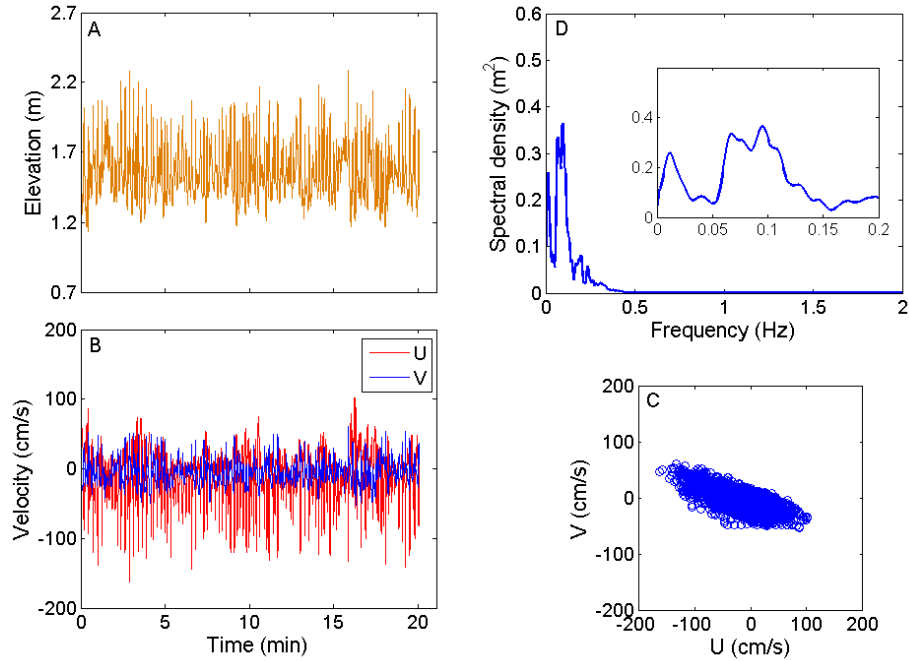
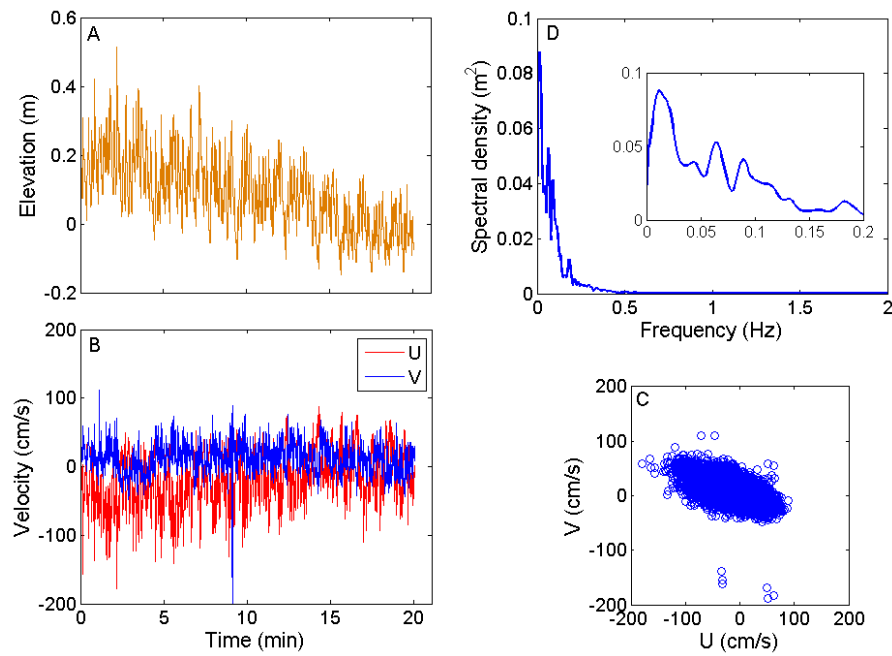


Figure 5.10 (1): ADV 1 at high tide. Panel A: water depth (ADV pressure in metres, relative to mean sea level) within one burst (20 minutes). Panel B: variation of wave-induced velocities in cross-shore and alongshore direction (U_w and V_w). Panel C: V_w versus U_w . Panel D: variation of the wave spectral density (modified periodogram spectral estimation using Welch method) versus frequency.



(2): ADV 1 at mid-tide.

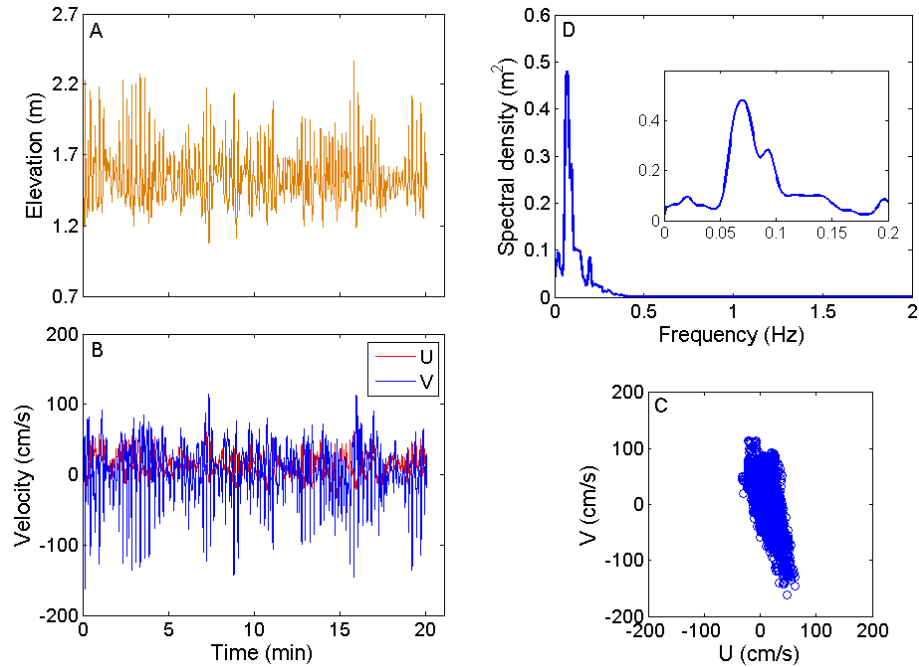
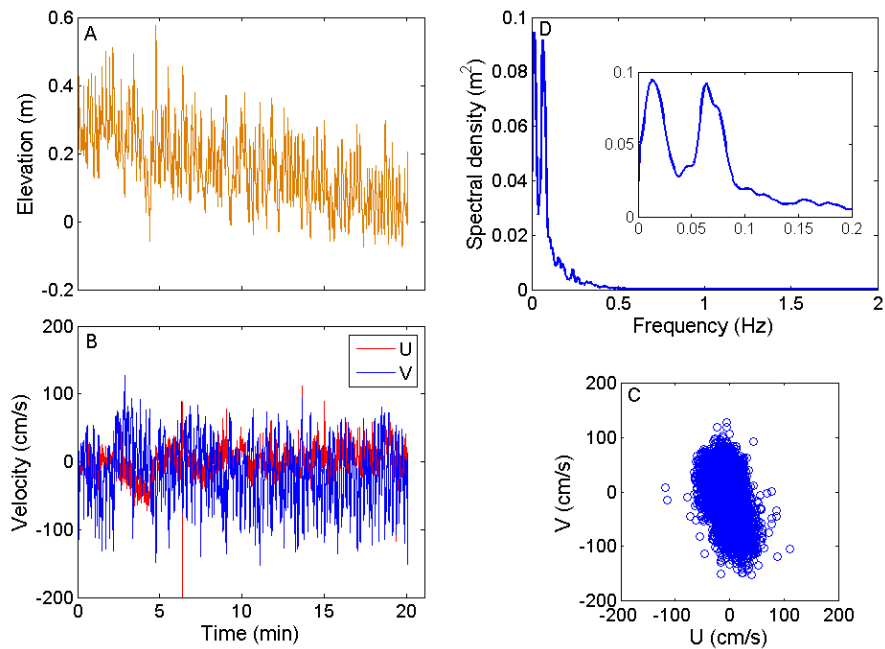


Figure 5.11 (1): ADV 2 at high tide. Panel A: water depth (ADV pressure in metres, relative to mean sea level) within one burst (20 minutes). Panel B: variation of wave-induced velocities in cross-shore and alongshore direction (U_w and V_w). Panel C: V_w versus U_w . Panel D: variation of the wave spectral density (modified periodogram spectral estimation using Welch method) versus frequency.



(2): ADV 2 at mid-tide.

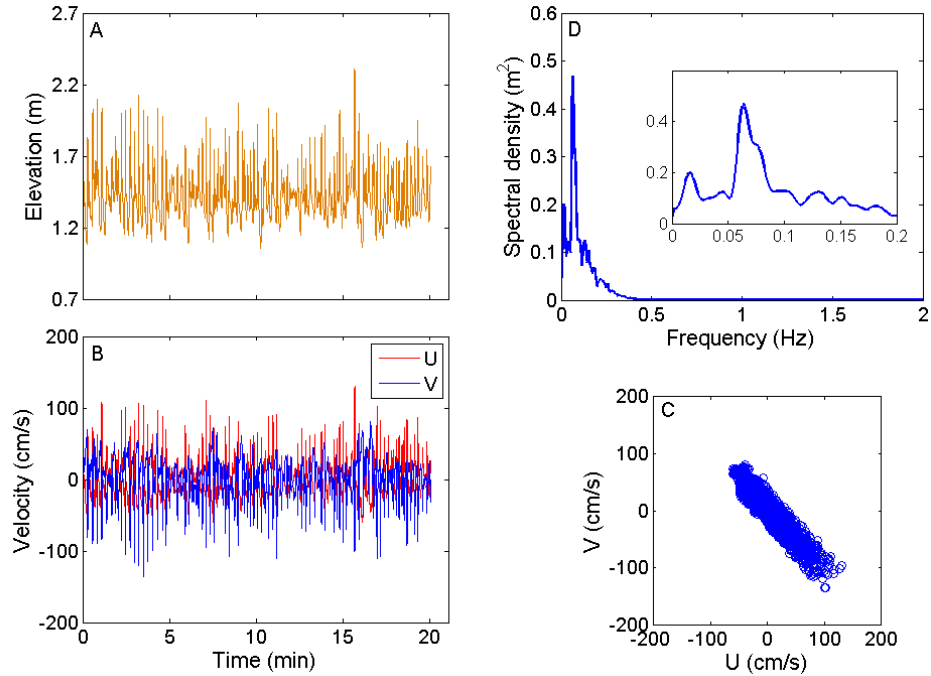
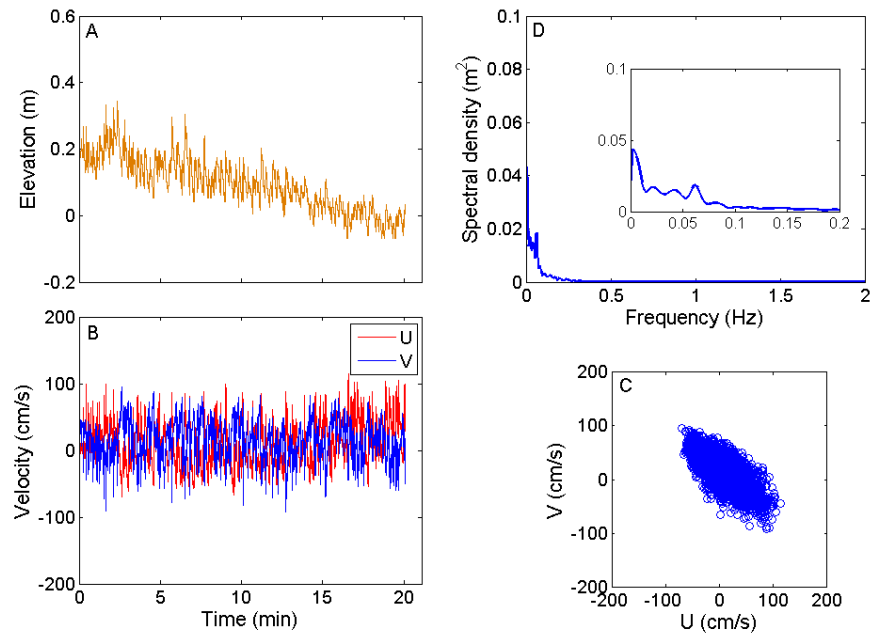


Figure 5.12 (1): ADV 3 at high tide. Panel A: water depth (ADV pressure in metres, relative to mean sea level) within one burst (20 minutes). Panel B: variation of wave-induced velocities in cross-shore and alongshore direction (U_w and V_w). Panel C: V_w versus U_w . Panel D: variation of the wave spectral density (modified periodogram spectral estimation using Welch method) versus frequency.



(2): ADV 3 at mid-tide.

Figure 5.13 shows the variation of the modified power spectral density (PSD) for different frequencies over all bursts. The wave energy distribution in transect 3 (panel D) shows different pattern in comparison with other two transects (panels B and C). The existence of the rip in the third transect probably causes this pattern difference. It also shows that high energy waves occur at high tide at both incident ($0.05-0.12$ Hz) and infragravity (<0.05 Hz) frequency ranges. It also indicates that in the first day (18^{th} September) waves are stronger than the second day (19^{th}).

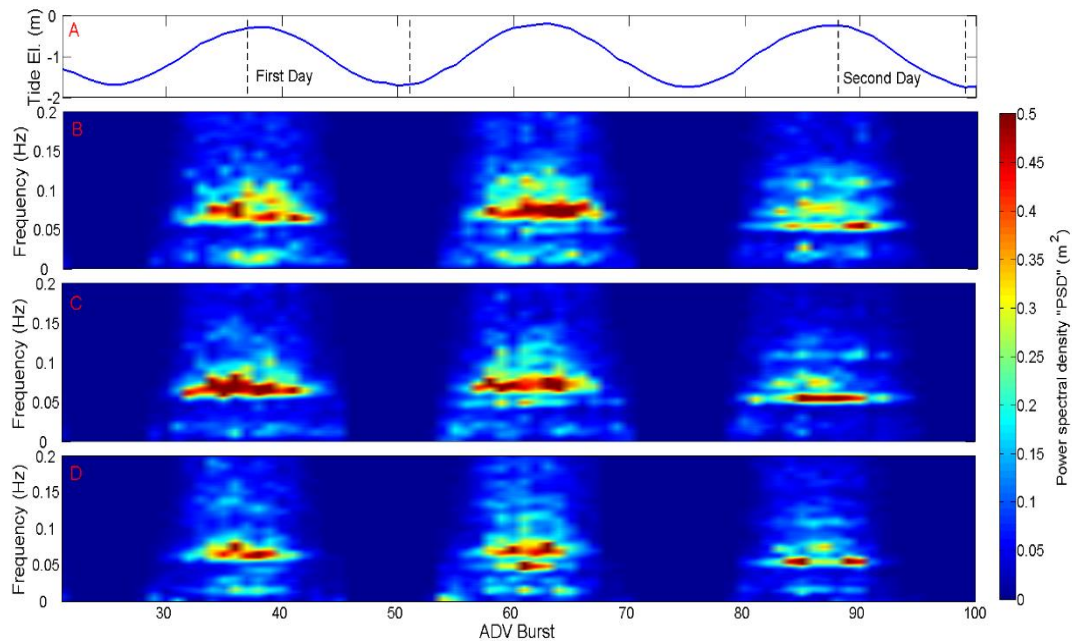


Figure 5.13 Panel A: Tide variation in 18^{th} and 19^{th} September 2013 at Ngarunui Beach. Panels B, C and D: Variation of the modified power spectral density (PSD) versus different wave frequencies over all ADV bursts along transects 1, 2 and 3 respectively.

Figure 5.14 shows the variation of the total PSD versus ADV burst for all three $ADVs$. The total PSD was defined as the summation of the modified PSD values of each frequency in one specific burst. In this figure PSD of the wave is studied separately in terms of incident wave and infragravity wave. Infragravity waves are waves, which forced by difference interactions in the wave frequency and have lower

frequencies than incident waves. The frequencies of infragravity waves are between 0.005 and 0.05 Hz, and the frequencies of incident waves are greater than 0.05 Hz. In figure 5.14, the *threshold of 0.05 Hz was used to differentiate infragravity waves from incident waves*. This figure shows that in general, transects 1 is more influenced by incident waves than transects 2 and 3. The existence of rip may cause less effect of incident wave on transect 3. However transect 3 is more affected by infragravity waves.

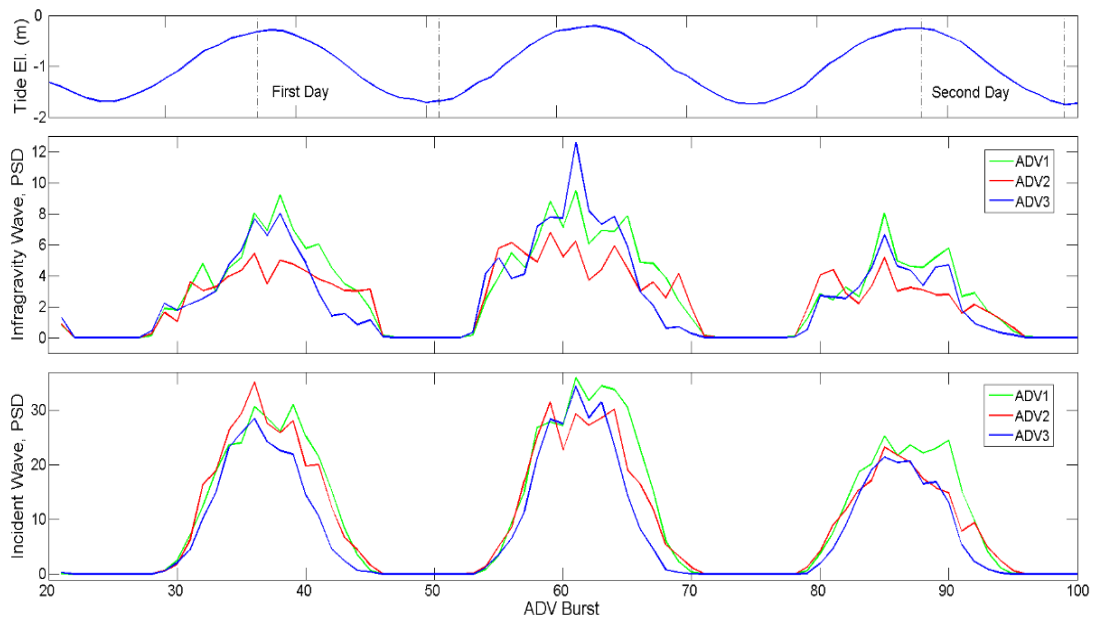


Figure 5.14 Panel A: Tide variation in 18th and 19th September 2013 at Ngarunui beach. Panels B and C: Variation of the modified power spectral density (total PSD values) over ADV bursts for infragravity and incident waves.

Furthermore, mean pressure and average of velocities of each burst were calculated. Figure 5.15 shows the variation of the average ADV pressure (water depth) and variation of the cross-shore and alongshore wave-induced velocities versus time. Transect 3 shows smaller water elevation (ADV pressure) than other two transects. The figure also indicates that, in general, alongshore velocity is much bigger in transects 2 and 3 than transect 1.

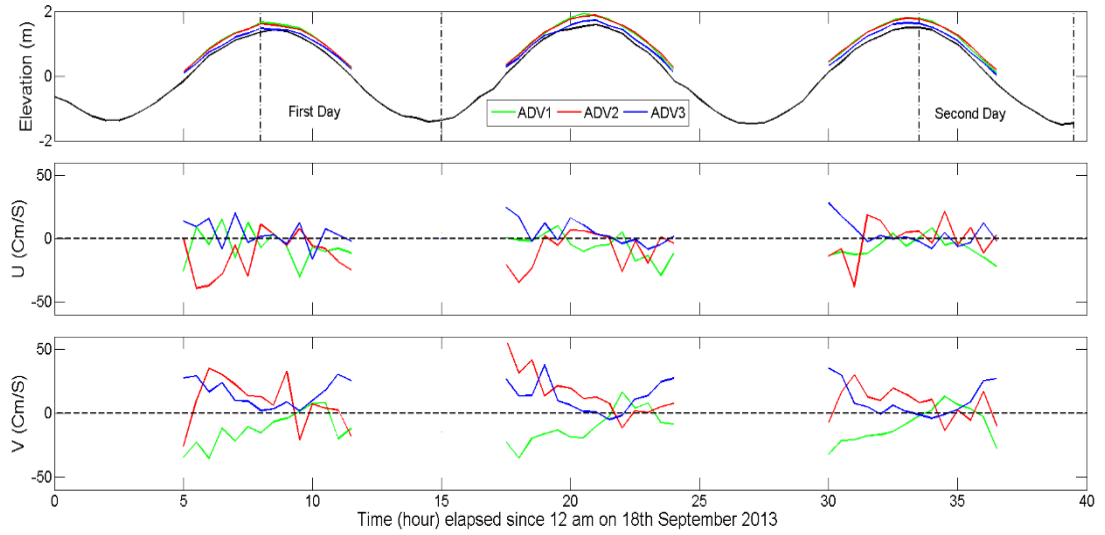


Figure 5.15 Panel A: variation of the average ADV pressure (water depth) and tide (black line) versus time elapsed from 12 am on 18th September 2013. Panel B and C: variation of the cross-shore and alongshore velocities versus time, respectively.

5.4 Discussion

To study the groundwater (*GW*) behavior at Ngarunui Beach, the variation of the groundwater level was measured using Solinst piezometers and manual dipwells for 2 days in September 2013. Figure 5.16 shows the location of dipwells, the elevation of the measured *GW* in them, the location of the high tide and low tide piezometers and the changes in the recorded *GW* level along the three transects.

The *GW* elevation varies between 1.8 and 2.3 metre above the mean sea level in high tide Solinst piezometers “*SHT*” (upper horizontal line in all panels), and clearly shows the effect of beach discharge and dewatering within a tidal cycle. Previous studies showed that the beach groundwater fluctuates with tide (e.g. Duncan, 1964; Eliot and Clark, 1986, 1988; Hegge and Masselink, 1991; Turner, 1993; Li et al., 1999; Nielsen, 1999; Horn, 2006). The beachface acts as a non-linear filter and make the beach groundwater level increase rapidly and decrease slowly in comparison with the tide variation. The delay time for groundwater response to tide could vary from minutes to hours (Weixing Guo, 1997; Horn, 2002, 2006).

Our results show that the *GW* level drops more slowly than tide drops, so the *GW* is decoupled and exits at a higher elevation. At low tide, the *GW* level does not reach to its minimum elevation and keeps decreasing for a few hours within the incoming portion of the tidal signal. There is a delay of 4 to 5 hours between low tide and the minimum in *GW* elevation. When the tide turns, the *GW* continues to fall, and converges towards the rising tidal elevation. When they finally converge at the same elevation, the *GW* is coupled with the tide and rises with only a minor lag until the high tide (Figures 5.8 and 5.16).

Our results indicate that Ngarunui Beach fills more easily than it drains. This finding is also supports previous studies, which indicated that the rate of the rising groundwater is considerably greater than the rate of the drop due to the gravitation force (e.g. Hegge et al., 1991; Horn, 2006).

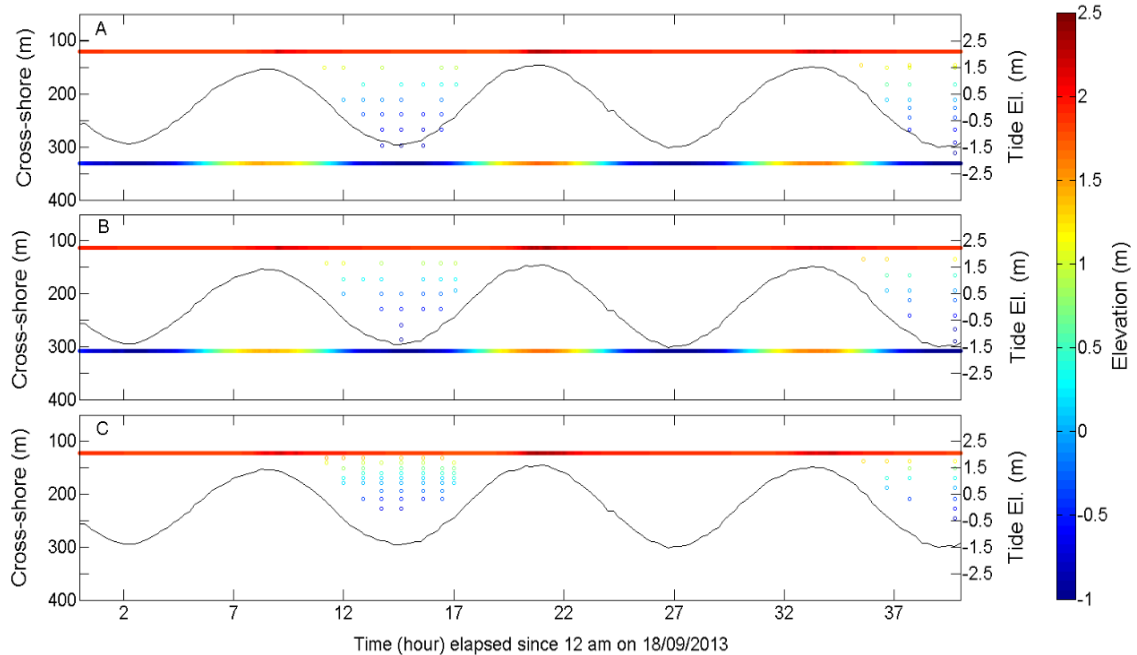


Figure 5.16 Instrument deployment results. Upper horizontal line shows the high tide Solinst piezometers and lower line shows the low tide piezometers. The black line presents tide data and circles indicates the location of dipwells and groundwater elevation measured in them. (Panel A, B and C: transects 1, 2 and 3 respectively).

The low tide Solinst piezometers were located in the lower part of the beachface near to the low water shoreline. Variation of the groundwater level in low tide piezometers “*SLT*” (lower horizontal line in two panels of Figure 5.16) is compatible with the tide variation. There is only a small difference between the *SLT* water level and tide level, which seems to be caused by the effect of the wave set-up, as the piezometer records the actual water level, which includes tide level plus wave set-up. At the low tide, the difference is greater than high tide and reaches up to 40 cm (Figure 5.8). This difference could not be the set-up effect (this is justified in more detail with a set-up calculation for Ngarunui beach in the next Chapter). The *ADV* water depth variation (Figure 5.15) also shows this difference at low tide. The difference may be due to an imprecise understanding of the location of the low tide piezometer and *ADVs*. The cross-shore location of the low tide piezometers were selected according to the shoreline shown in the video images. This work was done

before instrument installation in the beach, so Solinst piezometers positions may not exactly be at the same low tide elevation. SLTs and *ADV*s were probably located more onshore than the true location of the low tide waterline across the beach. This can make the water level measured by the instruments higher than the actual tide level plus set-up.

Manual water detection in the dipwells (circles in Figure 5.16) also shows how groundwater level changes during time cross the beach. In a specific cross-shore location, *GW* elevation declines with tide fall and increases with tide rise. The rate of fall and rise are the same as the pattern for Solinst piezometers. *GW* level in upper dipwells (circles located in cross-shore location less than 200) increase rapidly and decrease slowly in comparison with the tide variation. In fact, *GW* elevation variation is much smaller than the tidal elevation changes. In a constant time, *GW* has a descending trend in cross-shore direction (which is well-known).

Figure 5.17 shows the variation of the beach groundwater elevation versus time along the three transects. Regarding the duration time of the recorded data, the *GW* variation was studied during outgoing tide and then incoming tide in the first day of the field work (panels A, B and C, low tide marked with a vertical dashed line). On the second day (19th September 2013), this study included only the falling tide (panels D, E and F). This figure indicates that the groundwater elevation decreases in the cross-shore direction (up to down in all panels).

The *GW* decreases very slowly compared to the rate at which the tide falls. This variation is shown in panels A, B and C between 11:00 am and 2:50 pm in the first day and panels D, E and F between 11:30 am and 3:25 pm in the second day. Groundwater elevation in dipwells continued to decrease for few hours after low tide according to the delay between the low tide and the minimum of *GW* elevation (after 2:50 pm in the first day).

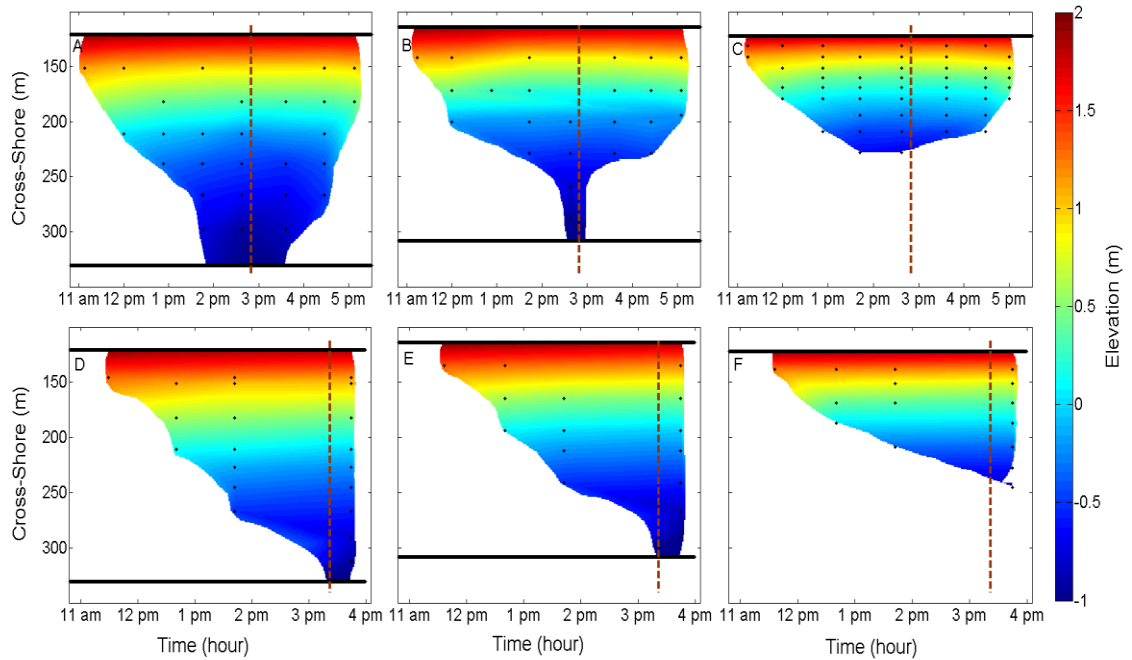


Figure 5.17 Variation of the beach groundwater elevation (measured in dipwells and gridded) versus time in three transects. Black horizontal lines show the location of the Solinst piezometer and black dots indicates the dipwell locations. Panels A, B and C shows the results in the first field work (18th September 2013) in transects 1, 2 and 3 respectively. Panels D, E and F presents results from the second field work (19th September 2013) along the three transects.

Another analysis was carried out to investigate how the measured groundwater elevation depended on the morphology. It was done by subtracting the two GW matrix collected. The gridding processes (the results of which is the GW matrix for each specific transect) includes all groundwater elevation measured in dipwells and groundwater level calculated by the high tide and low tide Solinst piezometers. Panels A and C show the GW elevation difference between transects 1 and 2, on the first and second day respectively. Panels B and D also indicate the GW difference between transects 2 and 3, on these two days. In general the difference between the beach groundwater elevation in transects 1 and 2 is greater than the difference between transects 2 and 3.

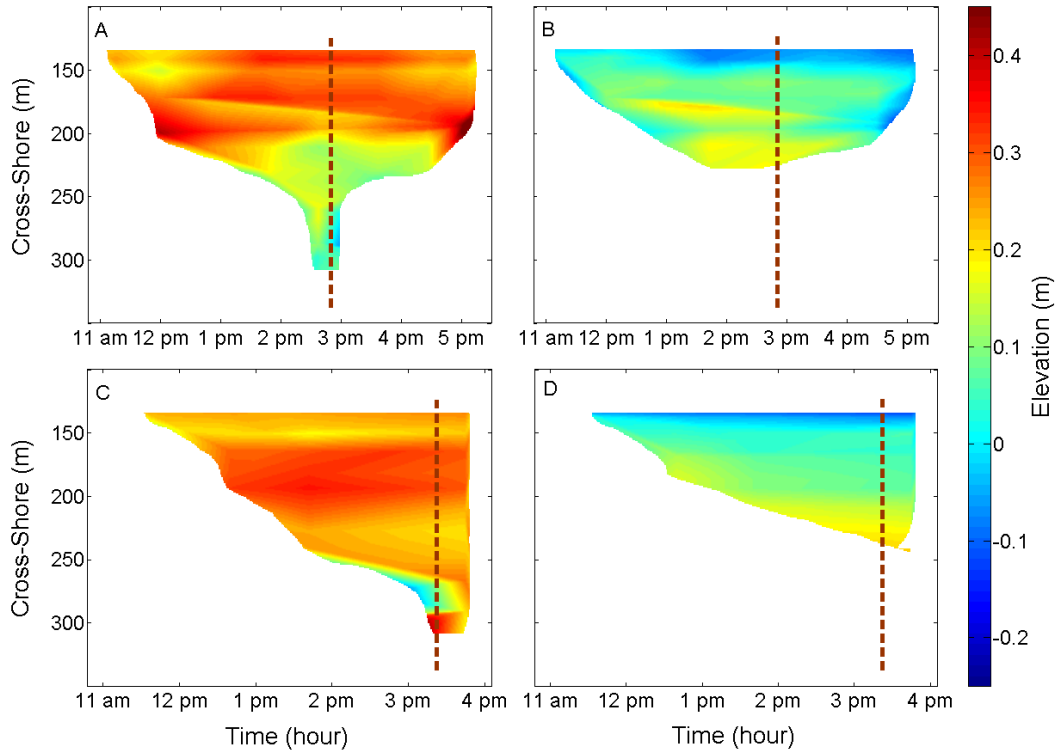


Figure 5.18 Difference between the groundwater elevation between two transects. Panel A, C: between transects 1 and 2 in the first and second day respectively. Panel B, D: between transects 2 and 3 in these two days.

It could be concluded that transect 1 in the north part of the beach shows highest groundwater elevation over most of the tidal cycle. Transect 3 in the south part of the study area has a lower groundwater level than transect 2 on the lower part of the beach, but a higher level than transect 2 on the higher part of the beach. Assuming that the coordinate system is absolutely perpendicular to the shoreline, this shows that there is a depression in the groundwater table, which is likely between transects 2 and 3. Such a dip in the groundwater table could also be caused by the beach being indented at transect 2, or transect 2 have higher hydraulic conductivity, or a steeper slope. The reverse in this pattern at low tide could be caused by a surf zone effect such as the influence of rip currents. Figure 5.15B shows that the offshore currents on the incoming tide at transect 2 are greater than at transects 1 and 3, and there are more

infragravity waves at transects 1 and 3 (Figure 5.14B). These may cause higher groundwater level at transect 2 on the lower part of the beach.

These preliminary observations of the difference in groundwater level across the beach will be studied in more depth using a two-dimensional numerical model in the next Chapter. The beach survey data and inland water table will be used to force the numerical model. The groundwater seepage line detected on the beach and the measured groundwater elevation will be also used for the model calibration.

**Chapter 6 : The Use of the 2D Boussinesq
Equation to Analyse the Groundwater Seepage
Line on Ngarunui Beach**

6.1 Introduction

As it described in Chapter Two, the Boussinesq equation, a simplified form of Laplace's equation, can be used to analyze the seepage line movement across the beachface and predict the surface of the beach groundwater table (e.g. Parlange et al., 1984; Nielsen, 1990; Turner et al., 1997; Baird et al., 1998; Raubenheimer et al., 1999; Li et al., 2002a; Li et al., 2006). Most of the previous works focused on the one-dimensional Boussinesq equation. Moreover, some of the approaches neglect the sloping beachface, the decoupling between the groundwater seepage line and shoreline, the hydraulic conductivity variation across the beach and the non-linearity effect (e.g. Baird and Horn, 1996; Jeng et al., 2005). For example, Nielsen (1990) used an analytical solution to the Boussinesq equation and stressed the importance of the hydraulic conductivity. He assumed that the beachface slope was constant and showed the groundwater table fluctuations became negligible with increasing the shoreward distance. However, Baird and Horn (1996) noted that Nielsen's model neglected the decoupling between the groundwater seepage line and the shoreline. Following previous works, Baird et al. (1998) showed that the groundwater flow could be explained by the one-dimensional Boussinesq equation. Raubenheimer et al. (1999) also worked on both the linear and non-linear one-dimensional Boussinesq equation and showed that under their model assumptions, the horizontal flows on a beach are usually much larger than vertical flows. Li et al. (2002) presented a two-dimensional approximation of the linear Boussinesq equation and predicted the tide-induced beach groundwater fluctuations over a rhythmic shoreline. Recently, Jeng et al. (2005) also applied a 2D approximation for determining the tide-induced groundwater changes in a sloping sandy beach. They showed that the beach slope and the rhythmic coastline are important in predicting tide-induced beach groundwater changes. Li et al. (2006) also used the 2D form of the Boussinesq equation (in horizontal cross-shore and alongshore directions) showing that their model was sensitive to the ratio of K/Sy .

In the third chapter, a one-dimensional numerical model based on the linear Boussinesq formula was presented to study the effect of the beach properties and seaward water level conditions on changing the groundwater seepage line across the Muriwai beach profiles. Due to the lack of the field data at Muriwai beach, the inland groundwater table was assumed to vary between 1 and 3 metres above the mean sea level and it was used as the upper boundary of the model. The hydraulic conductivity and beach slope were extracted from the previous field work carried out by Robinson (2004). An approximation of wave set-up was also done using wave significant height reported in previous studies (Bryan et al., 2007). Finally the model result, which included groundwater exit point elevation, was compared with the surveyed groundwater seepage line on 18th Feb. and 28th Aug. 2003 (the field data was part of Robinson's master thesis, Waikato University).

In this chapter, the Boussinesq equation is used again to understand the groundwater seepage line changes across the Ngarunui beachface and study the effect of the inshore and offshore factors on changing the groundwater exit point. The strengths of the model described in this chapter rather than the 1D linear model presented in chapter 3 are outlined as below:

- Using a two-dimensional approximation of the Boussinesq equation in a precise fine mesh grid consisting of cross-shore and alongshore surveying data.
- Solving both linear and non-linear form of the Boussinesq equation and compare the model results with surveyed seepage line to study the effect of the non-linearity of the aquifer depth and hydraulic conductivity on Boussinesq equation results.
- Using comprehensive field experiment, which is described in Chapter 5, as model input data and assistance in the calibration method.

6.2 Field data

6.2.1 Beach surveying data and groundwater table measurement

As described in Chapter 5, the beach survey was carried out on 18th and 19th September 2013 using GPS laser scanner. The study area of 400 by 400 metre was selected to cover an area between the dunes and surfzone. The survey data were rotated by 22 degrees anti-clockwise to convert the data from the northing-easting coordinate system to an alongshore-cross shore system. The beach was then mesh-gridded with 1 metre alongshore and cross shore intervals ($\Delta x = \Delta y = 1$ m) using MATLAB code. Figure 6.1 shows the beach mesh grid and the location of the three transects and deployed instruments. The first transect (T1) was selected at 365 m north of the datum point and the second and the third transects (T2 and T3) were located at 215 m and 86 m in the alongshore direction. Along each transect, two Solinst piezometers and one *ADV* were deployed to measure the beach groundwater variation and wave height, respectively. As it described before, an *ISD* was located in behind the dune between T1 and T2 to measure the long-term variation of the groundwater table (Figures 5.1 and 5.2). The manual groundwater measuring was done at different times between the high and low tide. The groundwater seepage line was measured by walking along it using the RTK-GPS four times in the first and second measuring days (18th and 19th September 2013), which is described in previous chapter. These observed data were used to compare with the numerical modelling results.

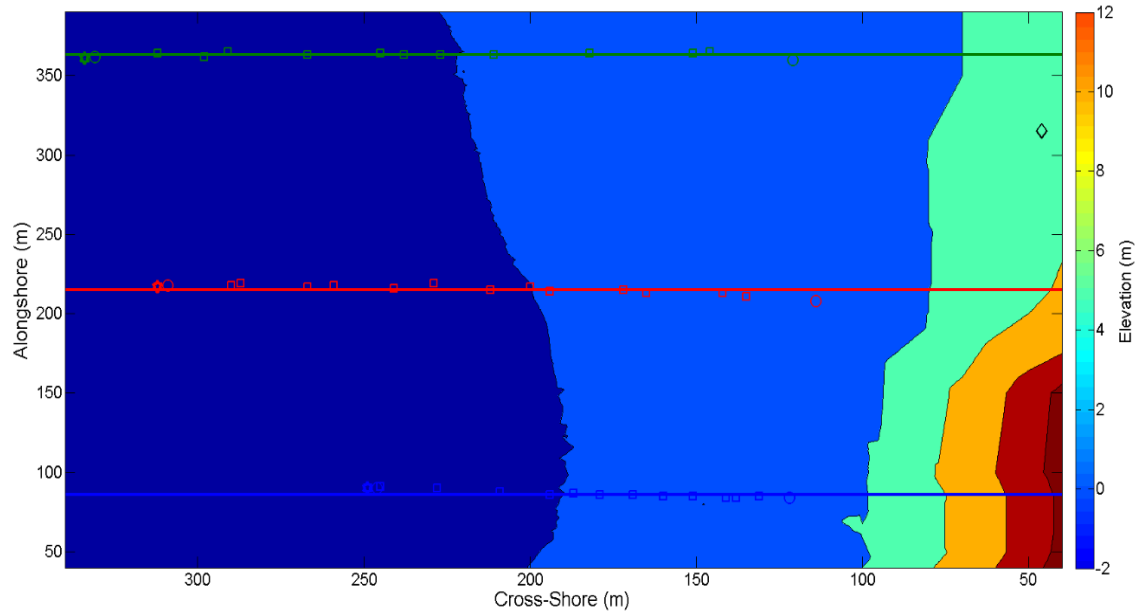


Figure 6.1 Mesh grid of beach surface elevation at Ngarunui Beach. Transects 1, 2 and 3 are shown with green (top), red and blue (bottom) lines respectively. A black diamond in dune shows the ISD location. Along each transect, the circles show the high tide and low tide Solinst piezometers (SHT, SLT), the hexagrams indicate the ADVs and the squares show the location of dipwells for manual groundwater measurement.

6.2.2 Tide and Wave data

An appropriate tide was selected from Manu Bay tide gage database (provided by Waikato Regional Council). Two time periods were considered: A) on the first day (18th), the outgoing tide between 8 am and 3 pm and then the incoming tide between 3 pm and 9 pm; B) on the second day (19th), the outgoing tide between 9 am and 3 pm. The significant wave height was provided from the NIWA wave hindcast model (output point No152) and the wave set-up calculated using the Bowen formula (Bowen et al., 1968), which is described in Chapter 3. Figure 6.2 shows the tide, significant wave height and wave set-up variation over the measuring days.

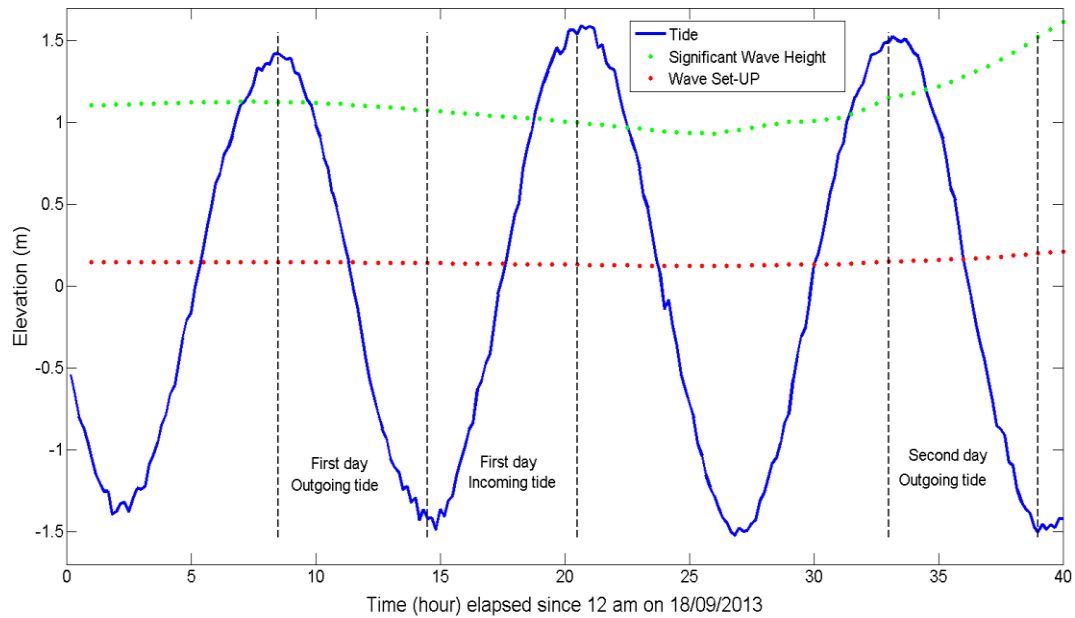


Figure 6.2 Variation of tide, significant wave height and wave set-up on 18th and 19th of September 2013.

6.3 Methods

As described in the third chapter, Baird et al. (1998) showed that the groundwater flow could be explained by the one-dimensional Boussinesq equation (Eq. 3.1). The assumption of applying this equation is that the Dupuit-Forchheimer (D-F) approximation explains the groundwater flow. The D-F approximation assumes that the groundwater flow is horizontal and changes in the hydraulic head with groundwater depth are negligible. In this case, the surface slope of the groundwater table is assumed to be relatively small (e.g. Kirkham, 1967, Baird et al., 1998). The two-dimensional form of the linear Boussinesq equation is as follows:

$$\frac{\partial h}{\partial t} = \frac{K.D}{S_y} \times \left(\frac{\partial^2 h}{\partial x^2} + \frac{\partial^2 h}{\partial y^2} \right) \quad (\text{Eq. 6.1})$$

where $h = h(x, y, t)$ is the groundwater elevation, K is the hydraulic conductivity of the beach, S_y is the specific yield (also described as a dimensionless parameter called porosity), D is the averaged-aquifer thickness, x is horizontal cross-shore distance, y is horizontal alongshore distance and t is time.

The non-linear form of the Boussinesq equation (2D form) can be described as:

$$\frac{\partial h}{\partial t} = \frac{1}{S_y} \frac{\partial}{\partial x} \left(Kh \frac{\partial h}{\partial x} + Kh \frac{\partial h}{\partial y} \right) \quad (\text{Eq. 6.2})$$

In all numerical calculations, the discrete approximation is used to solve the partial differential equation (*PDE*). In this approach, the results are calculated at a finite number of points in the physical domain. In this study, the mesh is the set of beach locations (nodes) where the discrete approach is computed. In next sections, the numerical model based on both 2D linear and non-linear Boussinesq equation will be described.

6.3.1 Numerical Model based on Linear Boussinesq equation

In order to solve two-dimensional linear Boussinesq equation (Eq. 6.1), *FTCS* (forward time, central space) scheme was used. In this numerical scheme, the first order forward difference in time (Eq. 6.3) and the second order central difference in space (Eq. 6.4) were applied.

$$\frac{\partial h}{\partial t} = \frac{h_{i,j}^{t+1} - h_{i,j}^t}{\Delta t} + o(\Delta t) \quad (\text{Eq. 6.3})$$

$$\frac{\partial^2 h}{\partial x^2} = \frac{h_{i,j-1}^t - 2h_{i,j}^t + h_{i,j+1}^t}{\Delta x^2} + o(\Delta x^2) \quad (\text{Eq. 6.4})$$

$$\frac{\partial^2 h}{\partial y^2} = \frac{h_{i-1,j}^t - 2h_{i,j}^t + h_{i+1,j}^t}{\Delta y^2} + o(\Delta y^2)$$

where, the $h_{i,j}^t$ is groundwater elevation in node $[i,j]$ at time step of t . $h_{i,j}^{t+1}$ is the elevation in the same node at the next time step ($t+1$). $h_{i,j+1}^t, h_{i,j-1}^t, h_{i+1,j}^t$ and $h_{i-1,j}^t$ are groundwater elevation in adjacent nodes at time step of t . $o(\Delta t)$, $o(\Delta x^2)$ and $o(\Delta y^2)$ are computational errors. Δx and Δy are the local distance between adjacent nodes in cross-shore and alongshore space respectively, and Δt is the time difference between adjacent time steps.

With applying these two equations in equation 6.1, the *FTCS* approximation of the linear Boussinesq equation can be written as follows:

$$h_{i,j}^{t+1} = \lambda \times (h_{i,j-1}^t + h_{i,j+1}^t + h_{i-1,j}^t + h_{i+1,j}^t) + (1 - 4\lambda) \times h_{i,j}^t \quad (\text{Eq. 6.5})$$

$$\lambda = \frac{\Delta t}{(\Delta L)^2} \times \frac{K.D}{S_y}$$

where ΔL is local distance in cross shore and alongshore direction ($\Delta L = \Delta x = \Delta y$)

6.3.2 Numerical Model based on Non-linear Boussinesq equation

In the same way as in the linear model, *FTCS* scheme was also used to solve the non-linear 2D Boussinesq equation. However, in this numerical scheme, the first order forward difference in time (Eq. 6.3) and the first order central difference in space (Eq. 6.6) were applied.

$$\frac{\partial h}{\partial x} = \frac{h_{i,j-1}^t - h_{i,j+1}^t}{2\Delta x} + o(\Delta x) \quad (\text{Eq. 6.6})$$

$$\frac{\partial h}{\partial y} = \frac{h_{i-1,j}^t - h_{i+1,j}^t}{2\Delta y} + o(\Delta y)$$

Combining Equations 6.3 and 6.6 with Equation 6.2; the *FTCS* approximation of the non-linear Boussinesq equation can be written as follows.

$$\begin{aligned} h_{i,j}^{t+1} = & r \times [k_{i,j}^t \times h_{i,j}^t \times (h_{i,j-1}^t + h_{i,j+1}^t + h_{i-1,j}^t + h_{i+1,j}^t)] + (1 - 4r \times h_{i,j}^t \times \\ & k_{i,j}^t) \times h_{i,j}^t + \frac{r}{4} \times [k_{i,j}^t \times (h_{i,j-1}^t - h_{i,j+1}^t)^2 + k_{i,j}^t \times (h_{i-1,j}^t - h_{i+1,j}^t)^2] + \frac{r}{4} \times [h_{i,j}^t \times \\ & (k_{i,j-1}^t - k_{i,j+1}^t) \times (h_{i,j-1}^t - h_{i,j+1}^t) + h_{i,j}^t \times (k_{i-1,j}^t - k_{i+1,j}^t) \times (h_{i-1,j}^t - h_{i+1,j}^t)] \\ & r = \frac{\Delta t}{(\Delta L)^2} \times \frac{1}{S_y} \end{aligned} \quad (\text{Eq. 6.7})$$

6.3.3 Using Numerical Model in Ngarunui Beach

As described previously, the study area was 400 by 400 metres. Using a 1 m space interval, a 400 by 400 matrix was defined as the initial matrix, which consisted of 160000 nodes. Figure 6.3 shows a schematic of nodes used in the model. In order to solve the numerical model, boundary conditions were required. The upper boundary condition was set to the water table elevation behind the dune, where tide variation has little effect on the groundwater table (ISD data, Section 5.3.1). The lower boundary condition was also set to the water level, which consist of the tide elevation and the wave set-up (Section 6.2.2). The sediment hydraulic conductivity and porosity were also estimated using the sediment grain size (section 5.2.2). The time interval (time difference between each time steps) was finalized after performing a sensitivity analysis based on the convergence model (see the next Section). In the first time step ($t=0$), the groundwater elevation was set to the initial value. In the next time step, groundwater elevation was calculated in all 160000 nodes using the ISD water table (WT) and tide elevation plus wave set-up. Hence, the upper and lower boundaries varied with time during model calculation at different time steps. It made it possible to use the exact value of the inland water table and offshore water level in the model. The rest of input parameters (ΔL , Δt , K , S_y and D in the linear model; and ΔL , Δt , and S_y in the non-linear model) were constant during the single run over all time steps. In fact at each time step, the elevation of every single node was calculated based on the elevation at this node and adjacent nodes at previous time step; using Equation (6.5) and (6.7) in the linear and non-linear model respectively.

The difference between the linear and non-linear Boussinesq equation can be described as the non-linearity effect of the groundwater elevation and hydraulic conductivity. In the linear form, the numerical model solves Equation 6.5 with constant value of the hydraulic conductivity (the average of K of the beach sediment) at all nodes, while the non-linear model solves Equation 6.7 with different K values at each node. In this case, beach sediment hydraulic conductivity, which was measured at different locations along the three transects (Figure 5.5), were used. The K matrix

was then determined using the mesh-gridding method on the K values. This non-linearity effect will be described more in the Discussion.

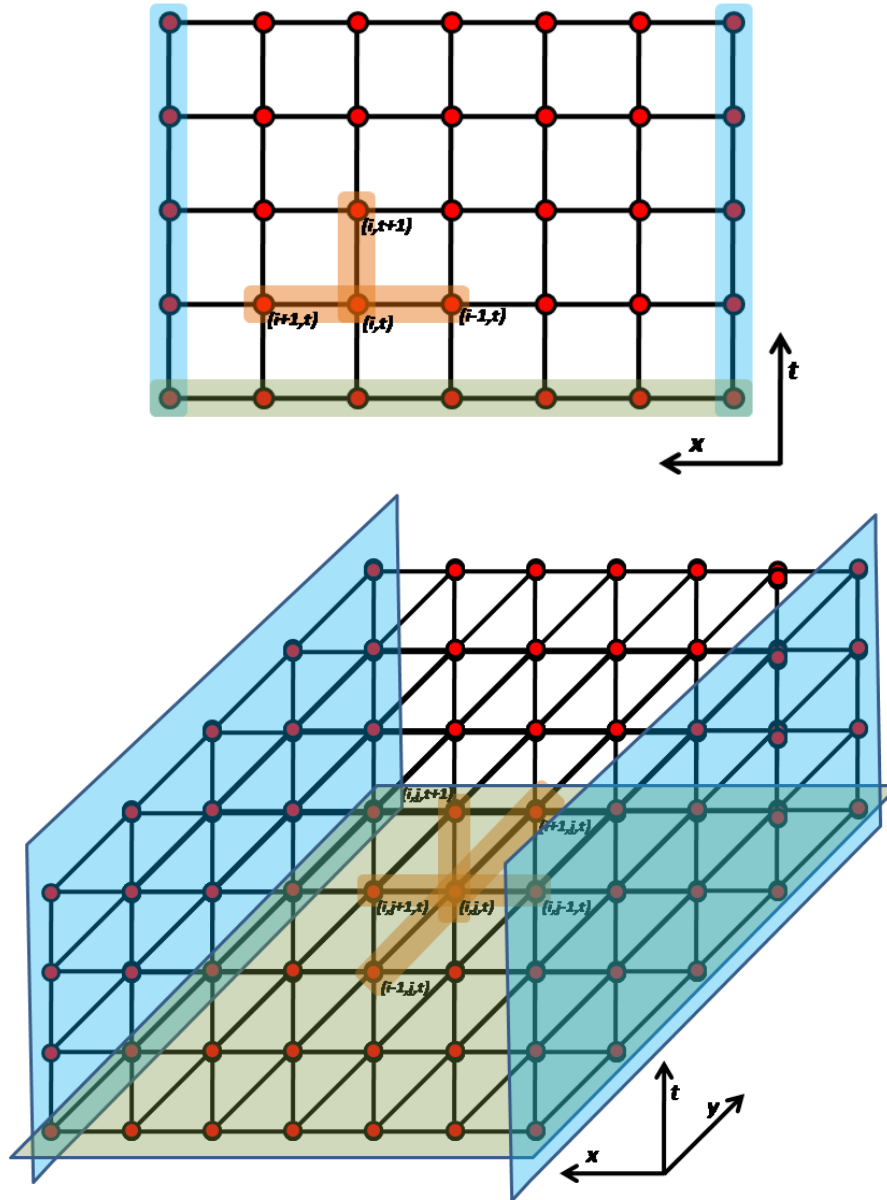


Figure 6.3 Schematic figure of nodes used in the 1D and 2D numerical model (upper and lower panels, respectively). The green line/area shows the initial condition of the numerical model. Right and left blue lines/parallelograms show the upper and lower boundary conditions respectively.

6.4 Sensitivity of the numerical model to involved factors

To study the effect of adjustable parameters in the model, including the time interval between each time step (Δt), the hydraulic conductivity (K), the inland water table (WT) and the wave set-up ($S-U$) on changing the calculated groundwater profile, a sensitivity analysis was done along the three transects using Equations 6.5 and 6.7 on the beach mesh-grid. In each analysis, the set of adjustable parameters were considered to be constant and one factor was changed to study its influence on the model result. This included 28 different runs of the linear and non-linear models.

6.4.1 Sensitivity of the model to the time interval (Δt)

To study the sensitivity of the model to the time interval (Δt), both the linear and non-linear models were run using different Δt (dt) and constant values of K (or a K matrix in the non-linear form), WT and $S-U$. Figure 6.4 shows the effect of changing dt on the groundwater profile and stability of the model along transect two. The other transects also show the same pattern. Decreasing Δt slightly changes the groundwater profile and increases the calculation accuracy; however it increases the number of time steps and the model run time. On the other hand, increasing Δt saves time but causes instability of the explicit finite-difference scheme. The divergence of results starts when Δt equals to 360 and 60 seconds in the linear and the non-linear model respectively. The Δt of 1 second, which leads to the convergence of results and optimum accuracy and run time, was selected as the time difference between time steps in both linear and non-linear models.

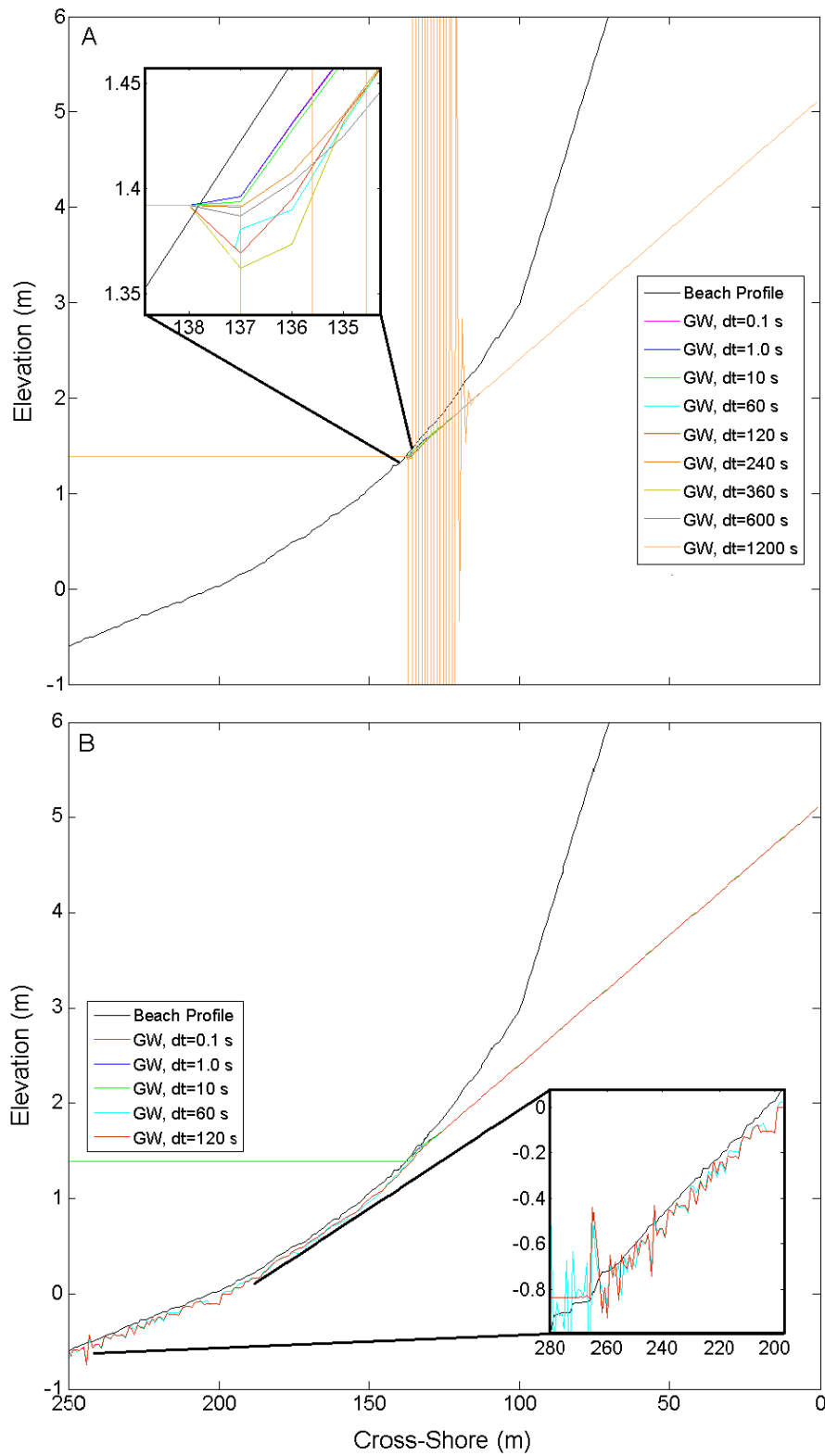


Figure 6.4 Sensitivity of the linear model (A) and non-linear model (B) to time interval.

6.4.2 Sensitivity of the model to the hydraulic conductivity (K)

To study the sensitivity of the model to the beach sediment hydraulic conductivity (K), both the linear and non-linear models were run using different K (or K matrix in the non-linear form) and constant values of Δt , WT and $S-U$. Figure 6.5 shows the effect of changing the hydraulic conductivity on the groundwater profile and stability of the model. The groundwater profile shape slightly changes with hydraulic conductivity in both the linear and non-linear models. The Figure indicates that the groundwater exit point elevation decreases with increasing the hydraulic conductivity.

My results also show that increasing the hydraulic conductivity may cause instability of the explicit finite-difference scheme and stop the model run. This is shown in Figure 6.5 (panel B) when K is doubled. However this change in the hydraulic conductivity does not cause the results to diverge in the linear model (panel A). The reason is the role of the K in solving Equations 6.5 (linear) and 6.7 (non-linear). In the linear model, changes in K (average hydraulic conductivity of beach sediment) vary the Courant number (λ) directly, while in the non-linear model hydraulic conductivity of each node is considered. This causes the non-linear model be more sensitive to the hydraulic conductivity, rather than linear model. It also differentiates between the effect of Δt and K on converging the non-linear model results, which will be described more in the Discussion.

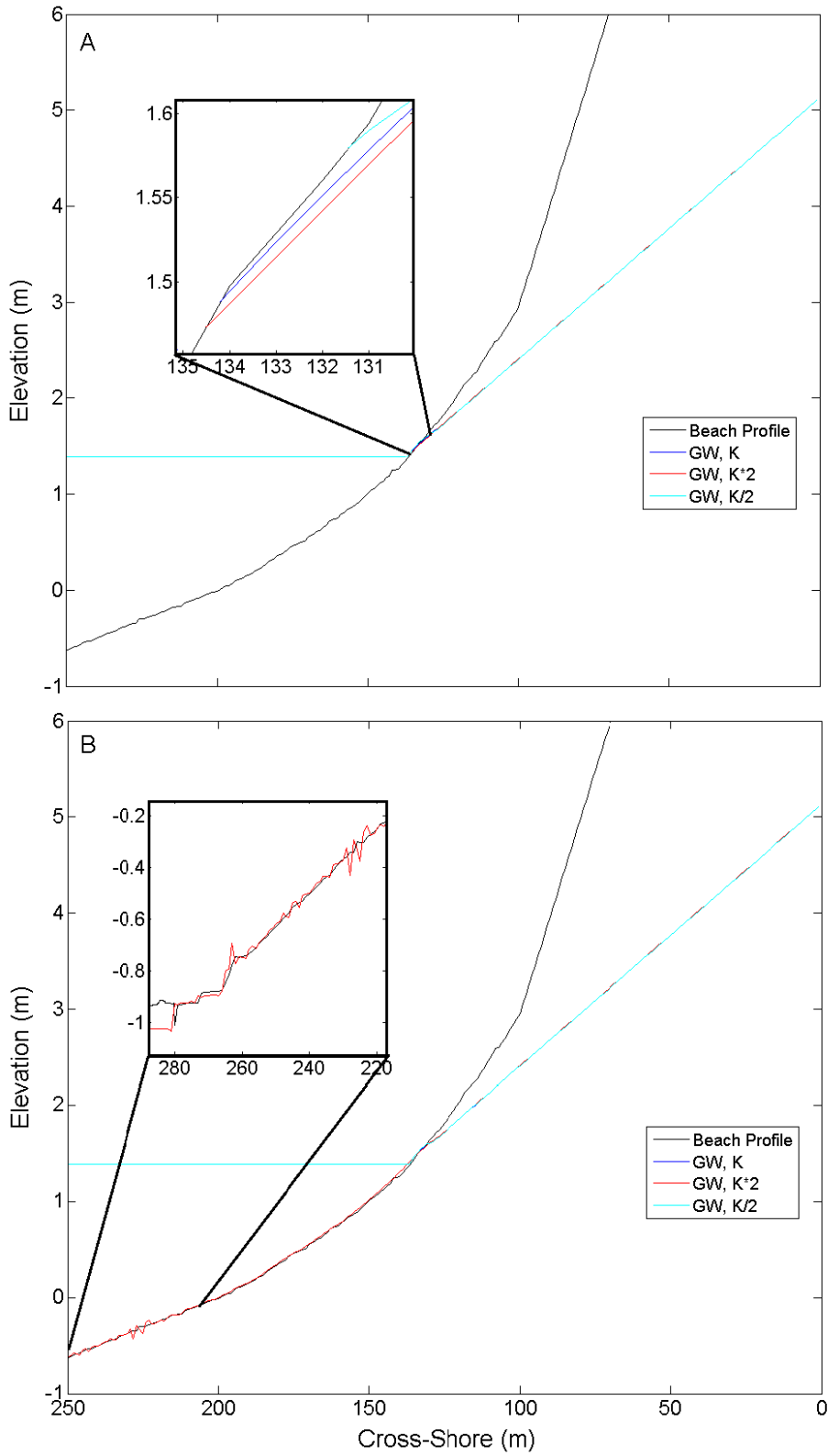


Figure 6.5 Sensitivity of the linear model (A) and non-linear model (B) to beach hydraulic conductivity.

6.4.3 Sensitivity of the model to the inland water table (WT)

To study the sensitivity of the model to the upper boundary condition (the inland beach water table), both linear and non-linear models were run using different WT and constant values of Δt , K and $S-U$. Figure 6.6 shows the effect of changing the inland groundwater table on the groundwater profile and the exit point elevation. The groundwater profile shape changes dramatically with changing the inland water table in both the linear and non-linear models. The Figure indicates that the groundwater exit point elevation increases with increasing the inland water table, which has been shown previously. This increment is up to 55 cm (in linear model) and 40 cm (in non-linear model) with 150 cm rise in upper water table elevation.

This indicates that changing the upper boundary condition of model, has a major effect on the groundwater exit point elevation and the location of the seepage line. The rise in the exit point elevation is bigger for high water table elevation rather than low inland water table.

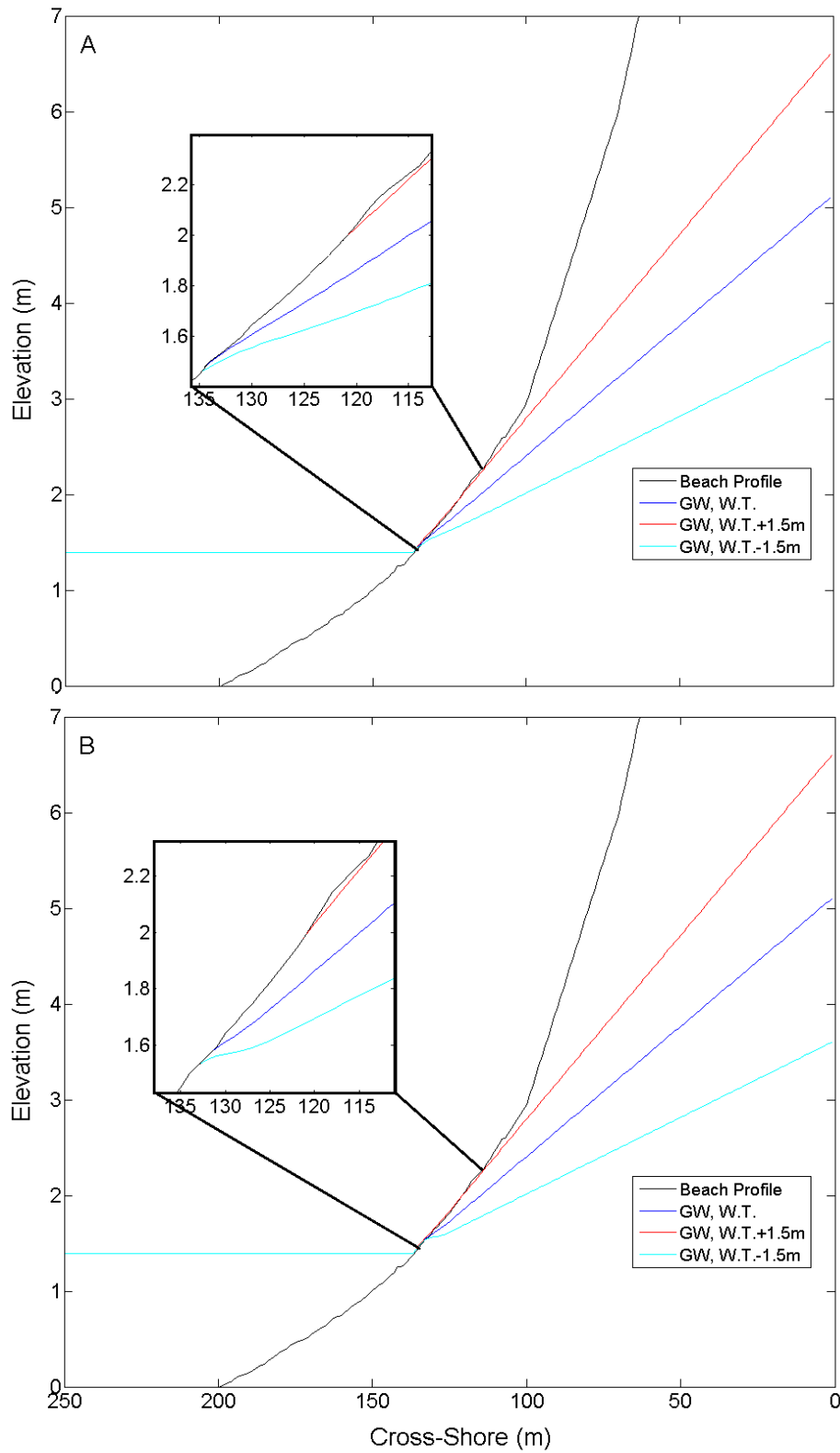


Figure 6.6 Sensitivity of the linear model (A) and non-linear model (B) to inland groundwater table.

6.4.4 Sensitivity of the model to the wave set-up (*S-U*)

To study the sensitivity of the model to the lower boundary condition (wave set-up), both linear and non-linear models were run using different *S-U* and constant values of Δt , K and WT . Figure 6.7 shows the effect of changing the wave set-up on the groundwater profile and exit point elevation. The groundwater profile shape changes with changing the wave set-up in both the linear and non-linear models. The Figure indicates that the groundwater exit point elevation increases with increasing the wave set-up. This increment is up to 28 cm (in linear model) and 20 cm (in non-linear model) with a 20 cm rise in the lower boundary condition. This indicates that changing the lower boundary condition of model affects the groundwater exit point elevation and location of the seepage line.

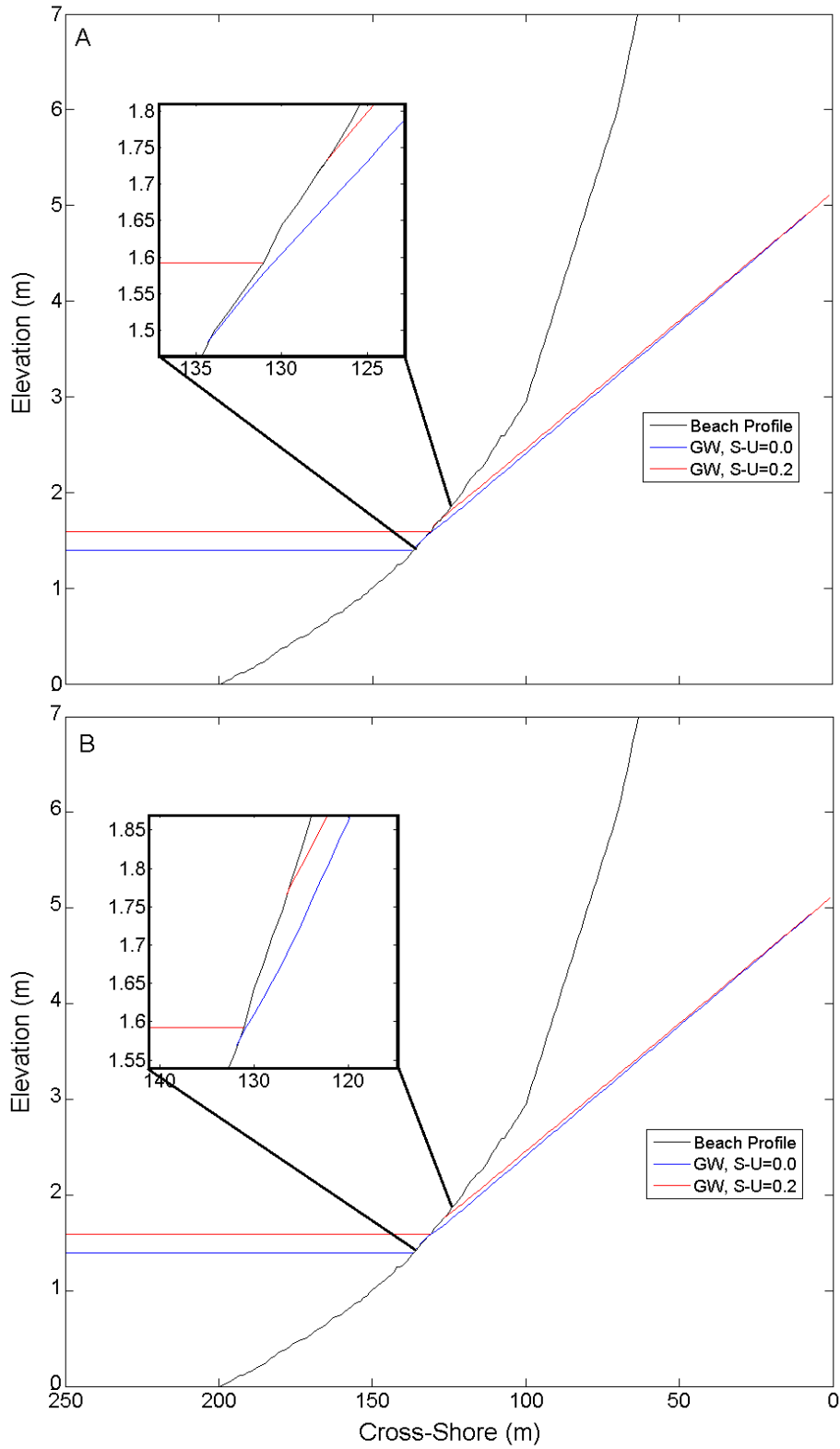


Figure 6.7 Sensitivity of the linear model (A) and non-linear model (B) to wave set-up.

6.5 Numerical modelling results

6.5.1 Groundwater exit point and extent of the seepage face

As it described in Section 6.3, the numerical model was developed based on the *FTCS* (forward time, central space) scheme to solve Boussinesq equation in both linear and non-linear forms (Eq. 6.1 and 6.2 respectively). The *FTCS* approximation of the linear and non-linear Boussinesq equation (Eq. 6.5 and 6.7 respectively) were then solved using a mesh-grid consisting 160000 nodes. This process was repeated for all time steps, calculating the groundwater profile at every 5 metres in the alongshore direction. The model results were then compared with groundwater survey data. In each alongshore location, the intersection of the final groundwater profile (groundwater profile calculated in the last time step) with beach profile was defined as the groundwater exit point (*GWEP*). Figures 6.8 and 6.9 show the variation of the groundwater exit point elevation along the three transects. The blue line in the Figure shows the tide variation on the 18th and 19th of September 2013. The red line indicates the calculated groundwater exit point using the numerical model (Figure 6.8 for linear model and Figure 6.9 for non-linear model). This was calculated between 8 am and 8 pm on the first measuring day covering the outgoing and incoming tide and between 9 am and 3 pm on the second day including the outgoing tide. The black squares show the surveyed groundwater elevation in different times. These data were obtained from the groundwater seepage line survey (previous Chapter).

Figure 6.8 shows that there is not much difference between the elevation of the exit point (calculated by the linear model) and the tide elevation between the high tide and mid tide in the outgoing tide. It means that there is not decoupling between the shoreline (*SL*) and the groundwater seepage line (*GWSL*). Decoupling starts from mid tide and difference between the elevation of *SL* and *GWSL* reaches a maximum at low tide. Panel A shows that during the incoming tide, the pattern is same as the outgoing tide (no decoupling between mid tide and high tide). Reversely, Panels B and C show

that decoupling continues to rise during incoming tide, which is unlikely to happen as described in the Discussion.

Figure 6.9 shows that there is not decoupling between the groundwater seepage line (calculated by the linear model) and the shoreline between high tide and mid tide, either in the outgoing tide or incoming tide. Decoupling starts from the mid tide and difference between the elevation of *SL* and *GWSL* reaches to the maximum at low tide. This decoupling process will be described in the Discussion.

Figures 6.10 and 6.11 also present the variation of the seepage face (*SF*) width (the cross-shore distance between the groundwater exit point and the shoreline) during the time. In linear model (Figure 6.10), along transect 1 (Panel B), the seepage face was only extended for few hours around the low tide, while in transects 2 and 3 (C and D) it can be seen during the incoming tide, which is unlikely to happen. In the non-linear model (Figure 6.11), in all three transects, the seepage face width increases when tide falls and decreases when the tide rises. The maximum seepage face width of 80, 100 and 50 metre were obtained in transects 1, 2 and 3 respectively, from the non-linear model around the low tide.

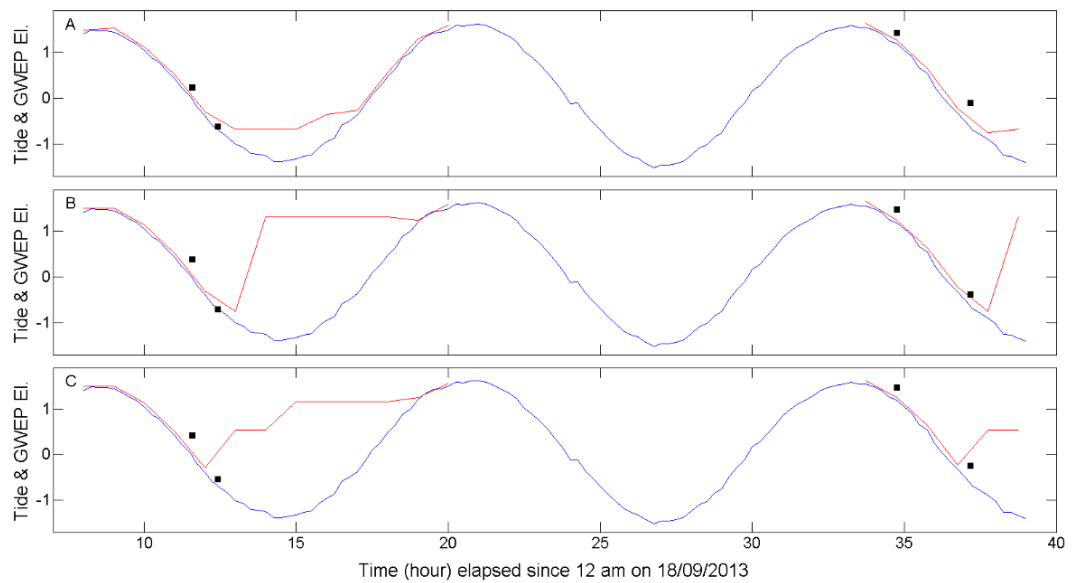


Figure 6.8 Linear model groundwater exit point elevation (red line), variation of the shoreline elevation (blue line) and surveyed groundwater seepage line (black squares) in Transect 1 (A), Transect 2 (B) and Transect 3 (C)

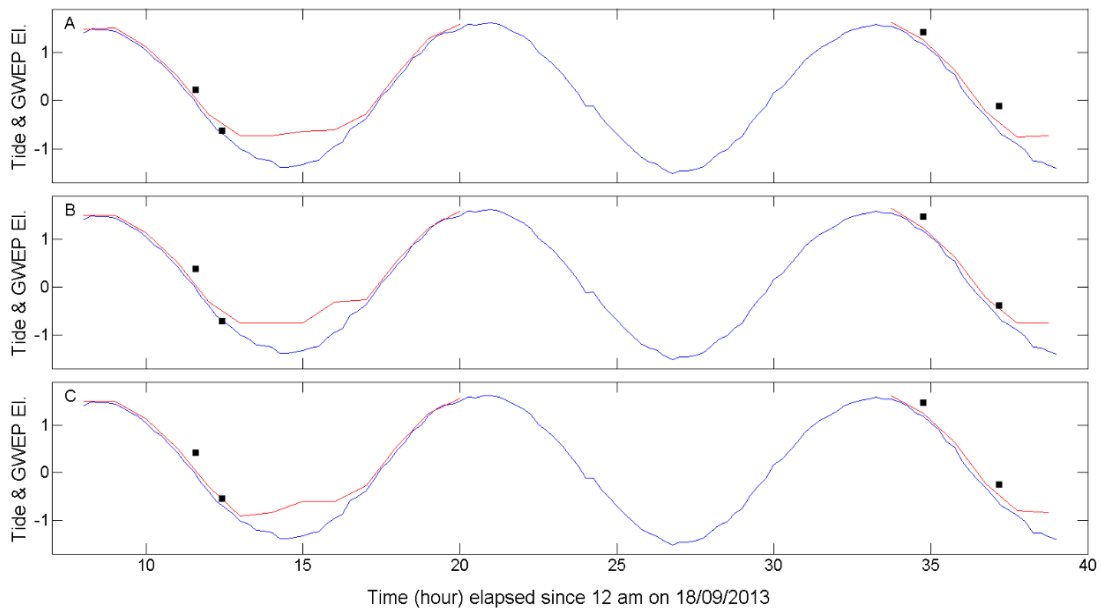


Figure 6.9 Non-linear model groundwater exit point elevation (red line), variation of the shoreline elevation (blue line) and surveyed groundwater seepage line (black squares) in Transect 1 (A), Transect 2 (B) and Transect 3 (C)

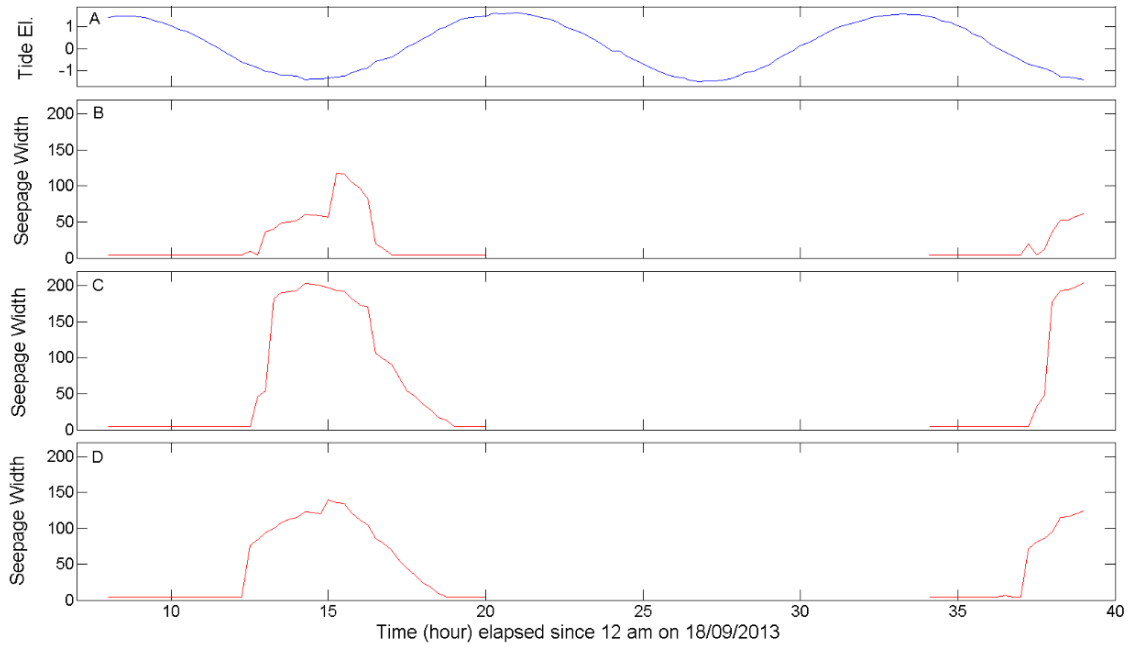


Figure 6.10 Groundwater seepage face width variation calculated from linear Boussinesq equation in Transect 1 (B), Transect 2 (C) and Transect 3 (D)

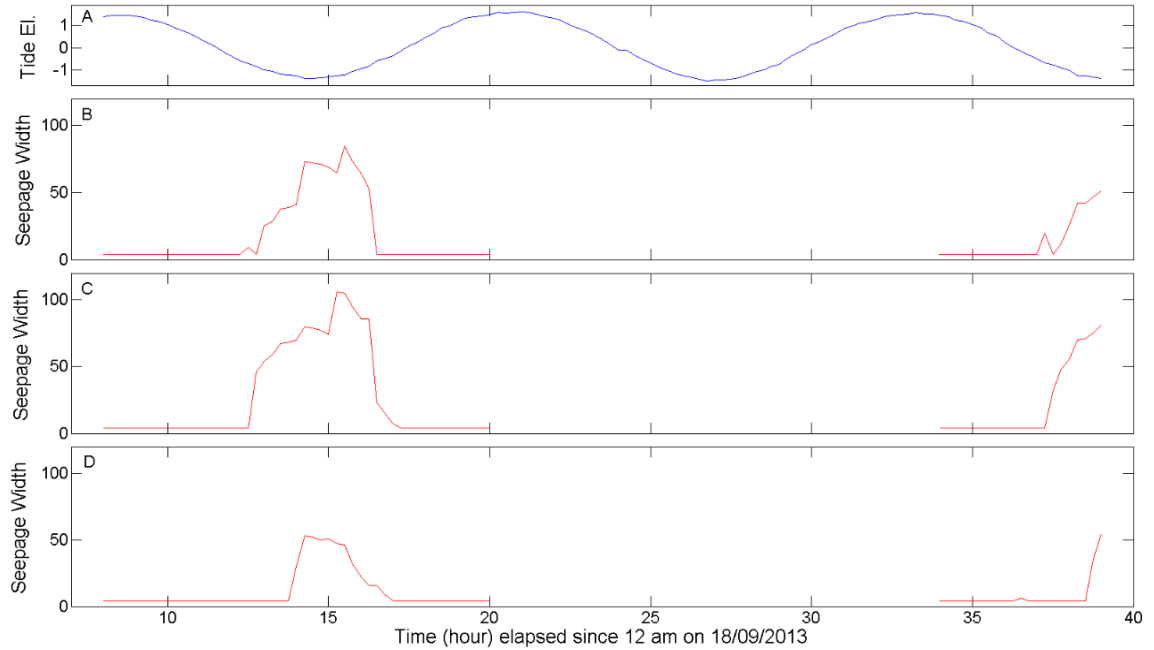


Figure 6.11 Groundwater seepage face width variation calculated from non-linear Boussinesq equation in Transect 1 (B), Transect 2 (C) and Transect 3 (D)

6.5.2 Comparison between the numerical model results and surveyed groundwater seepage line

To study the accuracy of the model based on Boussinesq equation, the calculated seepage line was compared with the surveyed groundwater seepage line at four different times during the measuring days. The measurements included seepage line tracking using a GPS laser scanner. It was not possible to survey the groundwater seepage line during the outgoing tide, as the day time was limited, hence, measurements were done during the incoming tide. Figures 6.12 and 6.13 show that both linear and non-linear model results are compatible with the surveyed data between high tide and mid tide. The non-linear model shows better results rather than linear model after the mid tide.

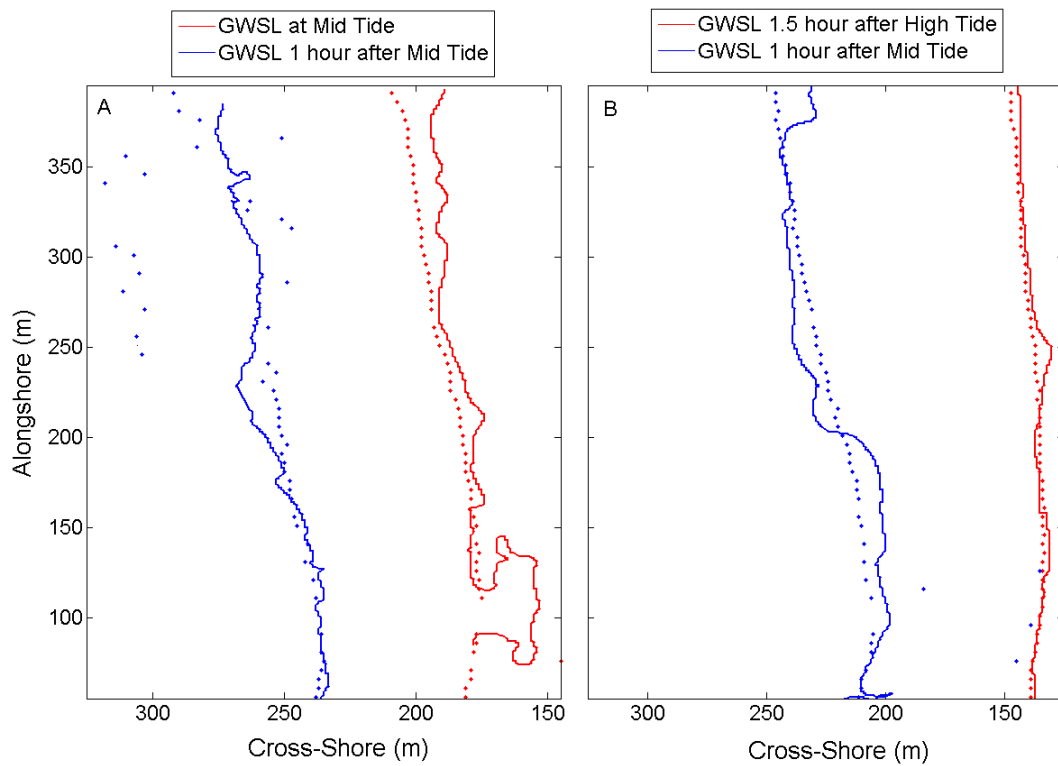


Figure 6.12 Comparison between the surveyed groundwater seepage line (solid line) and linear model results (dots). Panel A: First day (18th September 2013), Panel B: Second day (19th September 2013)

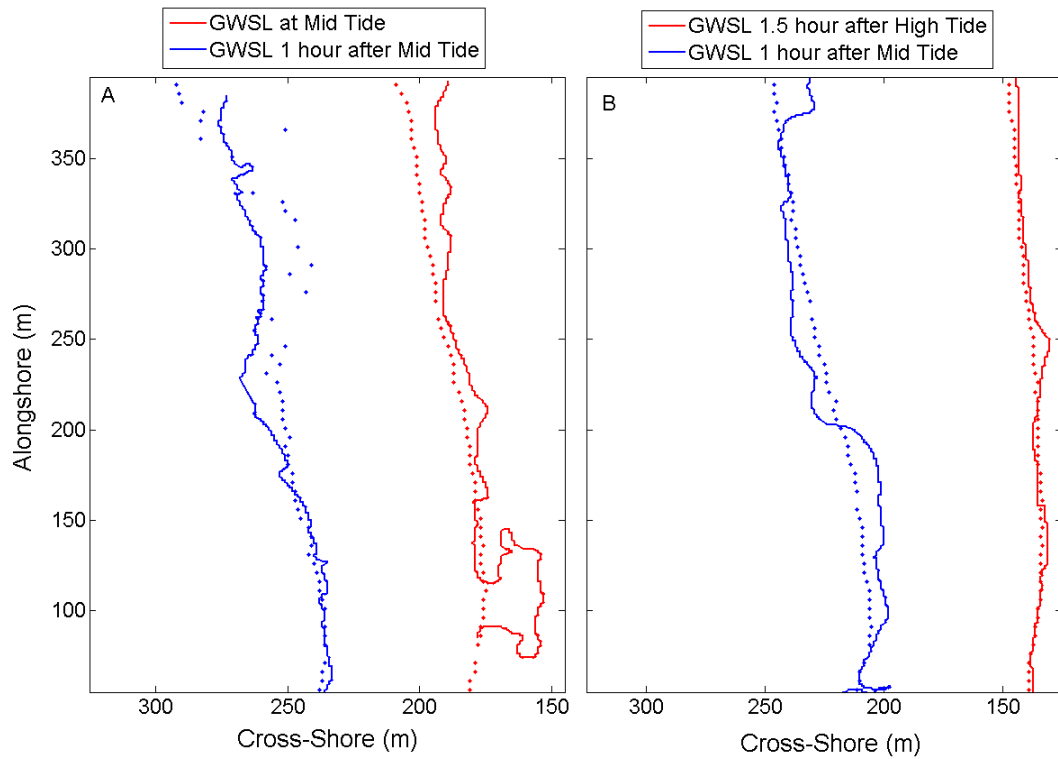


Figure 6.13 Comparison between the surveyed groundwater seepage line (solid line) and non-linear model results (dots). Panel A: First day (18th September 2013), Panel B: Second day (19th September 2013)

6.6 Discussion

The numerical analysis was done using the linear and non-linear Boussinesq equation to find the groundwater exit point along the Ngarunui beach and was used to study the observed decoupling between the groundwater seepage line and the shoreline.

Solving the linear Boussinesq equation (Eq. 6.1 and 6.5) is easier and faster (in terms of numerical running time) than the non-linear form (Eq. 6.2 and 6.7), but the non-linearity effect of the groundwater depth and the hydraulic conductivity are neglected. In the linear form, the Courant number ($\lambda = \frac{\Delta t}{(\Delta L)^2} \times \frac{K.D}{S_y}$) directly increases with increasing time interval (Δt), average hydraulic conductivity (K) and average aquifer depth (D), hence the effect of changing the hydraulic conductivity will be as same as changing the time interval. In addition, the hydraulic conductivity is assumed to be constant all across the beach, while it naturally changes in the alongshore and cross-shore directions on the beach. Another problem with the linear solution is assuming the constant average value for the aquifer depth, which it is not easy to predict. In the non-linear form, r ($r = \frac{\Delta t}{(\Delta L)^2} \times \frac{1}{S_y}$) does not depend on K and D . The average aquifer depth has not any role in the model; and the groundwater depth is calculated at each node instead. Furthermore, the hydraulic conductivity at each single node is considered, hence the alongshore and cross-shore variation of K will not be neglected and the effect of changing the hydraulic conductivity will not be same as the time interval. This important issue makes the non-linear model more sensitive to the hydraulic conductivity. Although as it shown in Figure 6.5B, the non-linear model may diverge with increasing K and stop during its run.

Among the varying parameters in the model, tide variation is the most important factor in changing beach groundwater elevation. Figure 6.14 shows the variation of the average of the groundwater surface with tide. At each time, the value shows the average of the groundwater elevation calculated at all nodes of the beach mesh-grid using the numerical model. It clearly shows that the calculated groundwater elevation

varies with tide supporting previous studies (e.g. Raubenheimer et al., 1999; Li et al., 1997, 2002, 2006; Jeng et al., 2005; Guo et al., 2010). The upper boundary condition is another important factor in changing the groundwater profile and elevation of the exit point. The groundwater exit point elevates significantly with increasing the upper boundary condition (inland water table). The third factor is lower boundary condition (wave set-up), which increases the groundwater exit point elevation and extends the seepage face width across the beach. The fourth factor is hydraulic conductivity, which has a reverse effect on the groundwater exit point elevation. Increasing hydraulic conductivity decreases the exit point elevation and shorten the seepage face. Finally, the time interval between time steps of the model does not affect the exit point, but increasing this factor may causes instability of explicit finite-difference scheme.

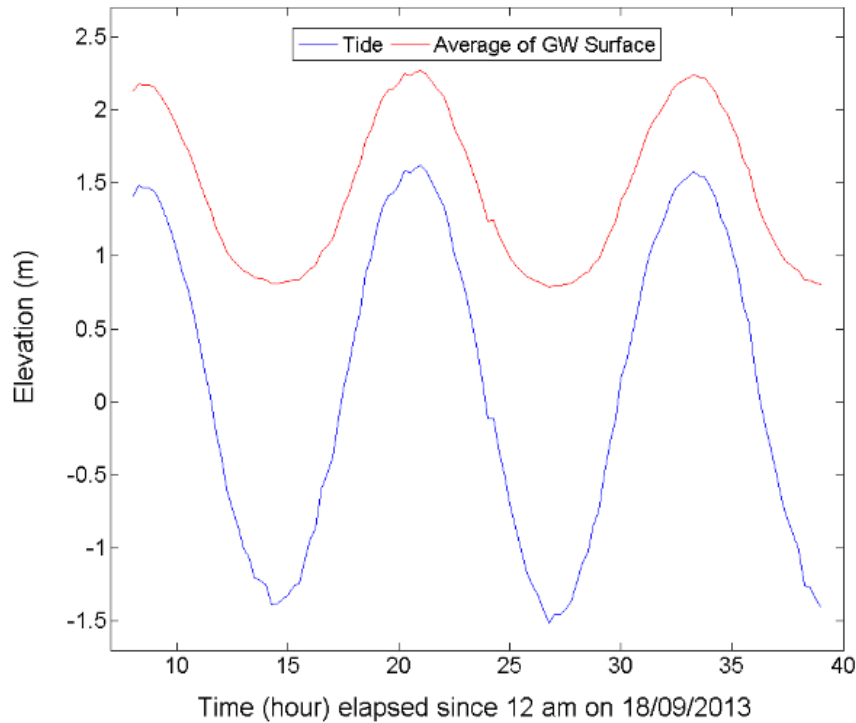


Figure 6.14 Variation of the “average of the groundwater surface, calculated by the numerical model” with tide

Both linear and non-linear models could predict the groundwater exit point location across the beach transects, variation of the exit point elevation and extent of the groundwater seepage face during falling and rising tide. The seepage face width increased as the time increased from mid tide during the outgoing tide and reached the maximum around low tide, and then decreased during the incoming tide. The difference between the seepage face variation in the linear and non-linear model is the extent of the seepage face during the incoming tide in the linear model.

Figures 6.15 and 6.16 show the decoupling between the shoreline and the seepage line between 8 am and 8:30 pm on the first measuring day covering the outgoing and incoming tide (Panels A, B and C); and between 9 am and 3 pm on the second day including the outgoing tide (panels D and E). Both linear (Figure 6.15) and non-linear models (Figure 6.16) show that there is not much decoupling between the groundwater seepage line (green dots) and the shoreline (blue line), which supports previous studies (e.g. Li et al., 1997; Turner, 1998; Huisman et al., 2011).

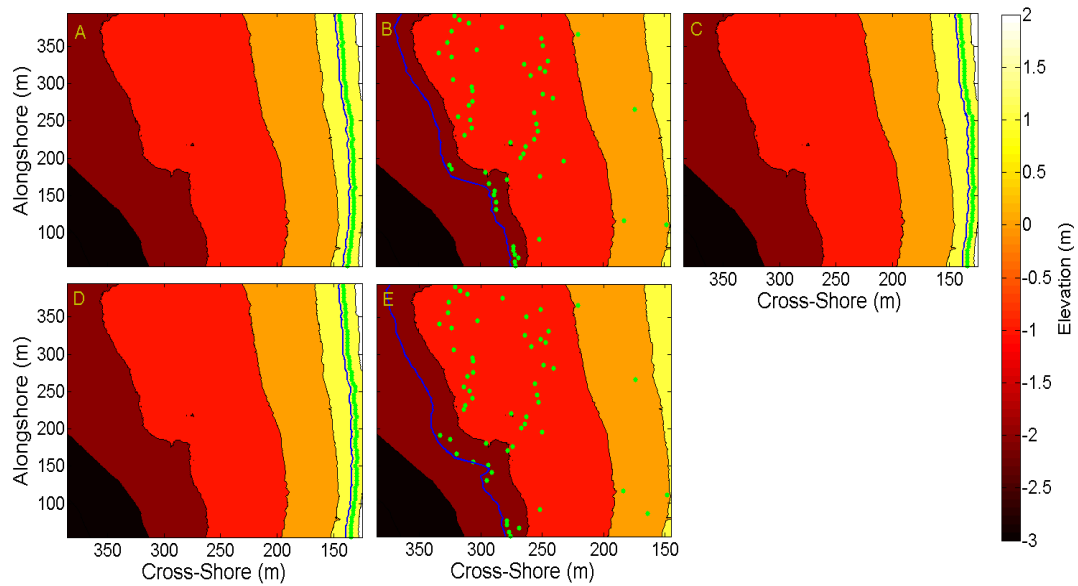


Figure 6.15 Decoupling between the groundwater seepage line (green dots, calculated from linear model) and the shoreline (blue line) at high tide (A), low tide (B), high tide (C) on 18th and at high tide (D), low tide (E) on 19th September

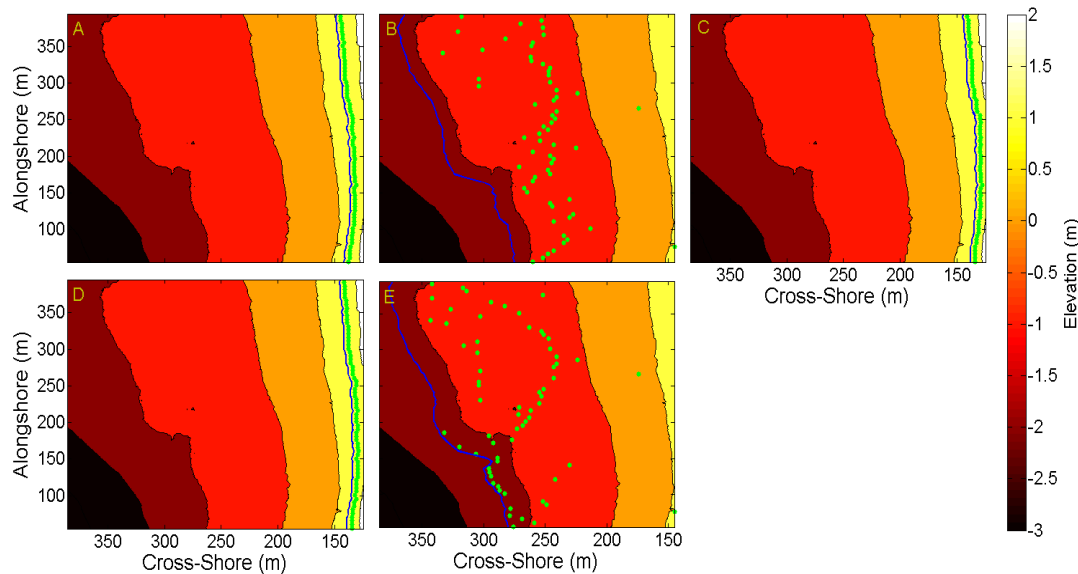


Figure 6.16 Decoupling between the groundwater seepage line (green dots, calculated from non-linear model) and the shoreline (blue line) at high tide (A), low tide (B), high tide (C) on 18th and at high tide (D), low tide (E) on 19th September 2013

In Ngarunui beach, hydraulic conductivity has an ascending trend in cross-shore direction towards the shoreline and also an ascending trend in alongshore direction towards south of the beach. The intertidal beachface slope is also bigger at south of the beach than the north. For example the cross-shore slope at transect 1 is almost 1/67 (mild), while it is 1/48 (gentle) at transect 3. Transect 2 is more similar to transect 1 than transect 3, in terms of intertidal beachface slope. Steeper slope and bigger hydraulic conductivity at south the beach could be the main reason for narrow seepage face in this area. On the other hand, milder slope and smaller hydraulic conductivity at middle and north part of the beach could cause the wider seepage face. As described in Chapter 3, statistical analysis on the surveyed data at Muriwai beach also showed that groundwater seepage line elevates with decreasing K and S , hence the seepage face extends. Turner, 1993 also indicated that seepage face is a function of the profile slope and permeability characteristics, however in the non-linear numerical model described in this chapter, the effect of the non-linearity of hydraulic conductivity, the inland water table changes and tide variations were considered to calculate the seepage face.

Figure 6.17 shows the comparison between the linear (Panels A, C and E) and non-linear (Panels B, D and F) models in terms of variation of the groundwater exit point elevation and the extent of the seepage face with tide. Two transects were selected for this purpose: Transect 1 (indicated with red colour in the Figure) in north of the beach, where the beach slope is mild, hydraulic conductivity is low and there is no rip current. Transect 3 (blue) in south of the beach, where the beach slope is steeper and hydraulic conductivity is bigger than the north; and there is a rip current almost in that area. The results of the linear and non-linear model are different, in terms of extending the seepage face during the incoming tide, which described as follows:

In the linear model, decoupling between the seepage line and the shoreline starts from mid tide in outgoing tide. Panels A and E (blue line) indicate that in south of the beach, decoupling continues to rise on the incoming tide. On the other hand, Panels A and C (red line) show that in north of the beach, the decoupling does not continue

after the mid tide in incoming tide. The unusual seepage face extent pattern showed by the linear model in south of the beach, could be caused by neglecting the non-linearity effect of the hydraulic conductivity in the linear model. As described in Chapter 5 and early this Chapter, the hydraulic conductivity is high in south part of the beach. It also varies in cross-shore direction, which was neglected in the linear model.

In the non-linear model, decoupling between the shoreline and groundwater seepage line starts since the mid tide during the outgoing tide and the seepage face can be seen over the incoming tide just before the mid tide (panels B, D and F, blue and red lines). The non-linearity effect of the aquifer depth and hydraulic conductivity seems to explain better results of the non-linear model rather than the linear model.

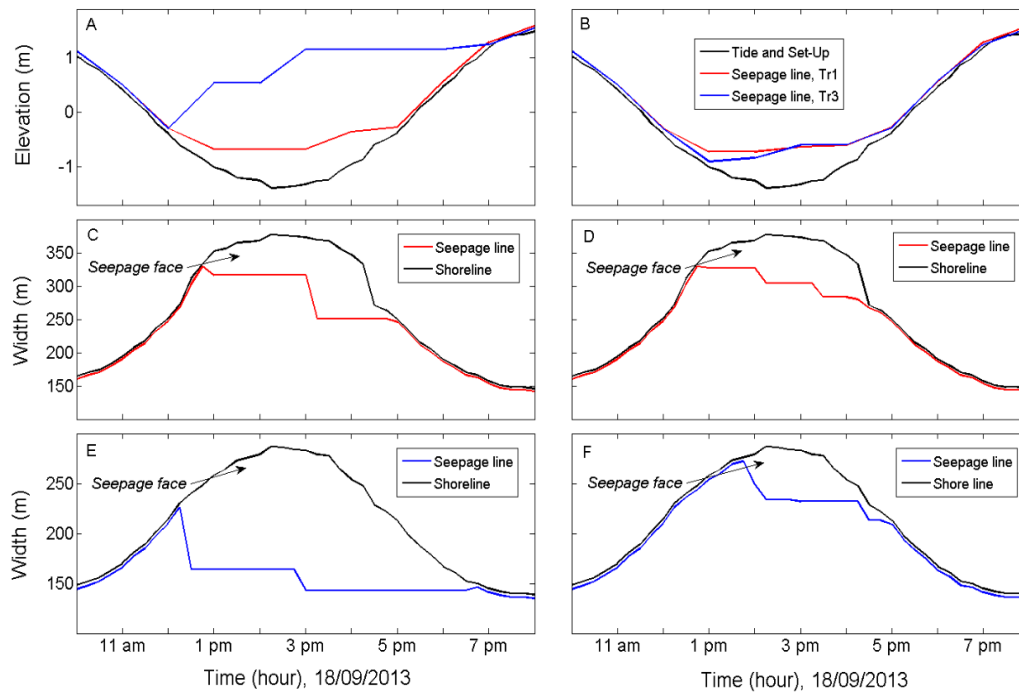


Figure 6.17 Variation of the groundwater exit point elevation (Panels A, B) and extent of the seepage face with the tide (Panels C, D, E, F) along two different beach transects (red indicates transect 1 and blue indicates transect 3). Left panels show linear model results and right panels show non-linear model results.

6.7 Conclusion

In conclusion, the numerical model based on the non-linear Boussinesq equation could predict the beach groundwater profile and determine the groundwater exit point across beach transects and extent of the seepage face. The seepage line calculated by the model is compatible with the surveyed groundwater seepage line (Figure 6.13). The non-linearity effect of the hydraulic conductivity and the groundwater depth may play an important role in accuracy of the results especially at low tide. The reason is that it considers hydraulic conductivity of the beach sediment in the lower part of the beach transects, where the conductivity is higher than upper part of the beach and this can affect the groundwater outcropping point. The sediment properties of this part of the beach are only important when the low tide occurs. This finding also highlights the role of the hydraulic conductivity in beach groundwater seepage line variation. The spatial distribution of the hydraulic conductivity seems to be more important than researchers previously thought.

In this study, it was also found that the groundwater seepage face predicted by the linear model was much bigger than the seepage face calculated by the non-linear Boussinesq model (e.g. Figures 6.10, 6.11, 6.12, 6.13 and 6.17). It can be concluded that the seepage face, which has been predicted in previous studies (using linear models) were probably overestimated. It also emphasises much more work on beach dewatering and effect of the groundwater outcropping the beachface on the beach erosion.

As it described before, a steeper beach profile and higher hydraulic conductivity are two important factors in decreasing the groundwater exit point elevation and shortening the seepage face width across the south of the beach. The field work including manual groundwater measurements in dipwells (Chapter 5) already showed that north part of the beach has the highest groundwater elevation over most of the tidal cycle. It also indicates that transect 3 in south part of the study area has a lower groundwater level than transect 2 on the lower part of the beach (Figure 5.17 and 5.18), which supports the numerical model results. The effect of the rip currents in

south of the beach may have an effect on lowering the groundwater exit point. The ADV located in this part of the beach shows a lower water level than ADVs in the middle and north of the beach although the difference is not significant (Figure 5.15). It seems that the effect of the rips may have a small effect on changing the groundwater seepage line rather than sediment properties and beach topography. It should be noted that my numerical model ran without a spatially-varying wave set-up along the beach. It caused my model results to exclude difference in the wave set-up, while the Solinst piezometer data recording and surveyed groundwater seepage lines (Chapter 5) included the spatially-varying wave set-up. The mismatch between the model results and survey data (Figure 6.13) especially around low tide, when the wave set-up effect is much important, can be because of neglecting the alongshore variation of the set-up and using just time-depending wave set-up. This issue can be the focus of next works on beach groundwater modelling.

Chapter 7 : Conclusions

In this research, two sites in the west coast of the New Zealand's north island were studied in this research: 1) Muriwai beach, which is a meso-tidal gently-sloping beach located on approximately 35 km west of Auckland and 48 km south of Kaipara Harbour entrance. 2) Ngarunui beach, which is also a dissipative gently-sloping beach, located near Raglan.

This thesis answered some fundamental questions, which mentioned in Section 1.2 as followed:

✚ What is the relationship between the observed groundwater seepage line and the intertidal beach volume and can this effect be separated from the influence of the rip currents?

✓ The field data collected by Amy Robinson (2003) at Muriwai beach was used to study the variation of the groundwater seepage line and its effect on the beachface volume. My statistical analysis showed that in most regions of the Muriwai beach, there is a clear correlation between the intertidal beach volume (V_o) and the groundwater seepage line ($GWSL$), with an elevated $GWSL$ causing a reduction of V_o . This inverse correlation occurred in all datasets and the effect of the higher groundwater seepage line on lower beachface volume is separated from the influence of rip currents.

✓ The seasonal analysis also indicated that the $GWSL$ in winter is more correlated with the V_o than summer. The higher inland groundwater table in winter likely causes more exfiltration on the beachface and, subsequently, lower beachface volume. The field results also indicated that V_o is more correlated with $GWSL$ at low tide rather than high tide, consistent with theory as increasing hydraulic head at low tide causes stronger seepage flow and greater potential for sediment remobilization. Hence, $GWSL$ has a greater effect lower on the beach, and beachface volume reduction is more influenced by the low tide $GWSL$.

✓ On the other hand my results showed that the correlation between the intertidal beach volume (V_o) and the surfzone morphology (SM) is not as easy to interpret as V_o and $GWSL$. The correlation between V_o and SM (characterized using pixel intensity measurements) indicated that unlike the $GWSL$, which always has

negative correlation with V_o , the slope of the regression line between the pixel intensity (PI) and V_o is sometimes negative and sometimes positive. I defined two different process pathways for the SM effect on changing V_o . In the first pathway, there is a positive correlation between V_o and PI as V_o generally decreases with decreasing PI . This is likely due to the rip currents causing sediment movement offshore, so that the beach is scoured out landward of the rip current. This often occurred at the middle of Muriwai Beach, which was a region of strong rip current activity. In the second pathway, there is a negative correlation between V_o and PI where V_o decreases with increasing PI . In this case, two mechanisms are responsible: the presence of oblique bars; and the influence of the surfzone morphology on wave set-up. The alongshore variation in PI does not differentiate between oblique bars and rip currents. With oblique sandbars, the shoreline is steeper where the bar is closer to the shore. Thus, an in-phase coupling between bar and shoreline due to the sediment exchange between the bar line and beachface can promote lower beachface volume.

✚ What is the best statistical model, which can describe the role of the groundwater seepage line and surfzone morphology in changing beachface volume? What is the accuracy of this statistical method?

✓ The variation in the intertidal beachface volume (V_o) was regressed against the groundwater seepage line field data ($GWSL$) and the surfzone morphology factor (SM), which was based on the pixel intensity of the time-averaged video images. Among the five different regression models, the multiple linear regression including $GWSL$ and SM without any cross terms ($V_o = a_1 + a_2 \times GWSL + a_3 \times SM$) was selected based on the highest r-square and statistically significant results with 95% confident level in the F-statistical analysis.

✚ How well can video images be used for extracting the groundwater seepage line and shoreline at a dissipative meso-tidal beach? What is the accuracy of this technique in comparison with surveying data?

✓ The video images taken by Cam-Era video system at Ngarunui Beach were used to study the application of the video images to extracting the groundwater seepage line and shoreline. According to my results the time-averaged images can be used well for extracting the groundwater seepage line. On the other hand, the comparison between the extracted shorelines from variance images and the surveyed shoreline (based on the field data by Guedes, 2010) indicated that the shoreline extracting algorithm using variance images is not always accurate. The results showed that in the incoming tide the elevation of the calculated beach surface is lower than the surveyed beach surface in some parts of the beach and higher in some other parts. In the outgoing tide the calculated beach surface is always higher than the surveyed beach surface. In the both tidal periods, the difference between the surveyed data and video based data in upper intertidal beach is much lower than lower part of the beach indicating that the video extracting algorithm works better at the high tide rather than the low tide.

 How does the groundwater seepage line on a dissipative meso-tidal beach change over a tidal cycle? How can video images be used to observe the decoupling of the groundwater seepage line from the shoreline?

✓ Both groundwater seepage line extracted from time-averaged images and shoreline extracted from variance images showed the decoupling process very well in both incoming and outgoing tide. During rising tide, the infiltration from the tidal wave causes the water table rise, although beach groundwater level increases much more quickly than rising tide. An hourly comparison of the decoupling process showed that the groundwater seepage line decouples from the shoreline more quickly on the lower part (less steep intertidal beachface) rather than the steeper upper part of the beach profile. On high tide, there is not much decoupling between the groundwater seepage line and the shoreline, which supports previous studies. In this case, the groundwater seepage line is located a few metres onshore of the shoreline. During falling tide, the groundwater seepage line starts to decouple again from the shoreline. As the beach drains more slowly than the tide falls, the groundwater seepage face appears between the *SL* and the *GWSL* because of the groundwater

exfiltration. Same as the incoming tide, in the outgoing tide, groundwater seepage line decouples from the shoreline more slowly on the upper part (steeper intertidal beachface) rather than the less steep lower part of the beachface. This decoupling process shows that Ngarunui Beach fills more rapidly than tide rise and drains more slowly than tide falls. This finding was tested precisely using my field data collected from the Solinst piezometers and manual water detectors at Ngarunui Beach in September 2013.

✓ Another finding of this study was how the seepage face (*SF*) width varies along the beach. The decoupling between the *GWSL* and *SL* extracted from video images clearly showed that the seepage face width is much greater in north and middle of the beach rather than the south part. According to the field data (Ngarunui Beach field data, September 2013), a steeper beachface profile and higher hydraulic conductivity are two important factors in decreasing the groundwater exit point elevation and shortening the seepage face width across the south of the beach. The rip current in south of the beach may also has an effect on lowering the groundwater exit point and shortening the seepage face width.

✚ What are the main parameters controlling the groundwater seepage line on a dissipative meso-tidal beach? Which driver (intertidal beach geometry, beach sediment porosity and hydraulic conductivity, tide variation, inland water table, rip currents and wave set-up) is the most important in explaining changes to the seepage line?

✓ The main parameters controlling the groundwater seepage line on a dissipative, meso-tidal beach includes the inland groundwater table, tide variation, wave set-up, intertidal beachface geometry, beach sediment porosity and the hydraulic conductivity. The numerical model results at Ngarunui beach showed that tide variation, intertidal beach morphology and the hydraulic conductivity are the most important factors in changing beach groundwater elevation. Higher tide elevation and wave set-up, and lower intertidal beachface slope increase the groundwater exit point elevation and extend the seepage face. Hydraulic conductivity has a reverse effect on the groundwater exit point elevation.

✓ In terms of groundwater seepage face extent across the beach, my numerical model results showed the wider seepage face in middle and north of the beach rather than the south (similar to the video imagery analysis). Steeper slope and bigger hydraulic conductivity at south of the beach could be the main reason for narrow seepage face in this area. On the other hand, milder slope and smaller hydraulic conductivity at middle and north part of the beach could cause wider seepage face. The field work including manual groundwater measurements in dipwells already showed that north part of the beach has the highest groundwater elevation over most of the tidal cycle. It also indicates that transect 3 in the south part of the study area has a lower groundwater level than transect 2 on the lower part of the beach, which supports the numerical model results. The effect of the rip currents in south of the beach may have an effect on lowering the groundwater exit point. The *ADV* located in this part of the beach shows a lower water level than *ADV*s in the middle and north of the beach although the difference is not significant. It seems that the effect of the rips may have a small effect on changing the groundwater seepage line rather than the sediment properties and the beach topography.

✚ Can numerical models (both linear and non-linear) based on the Boussinesq equation accurately predict the tidal groundwater changes across the beachface and determine the position of the groundwater exit point? Can the numerical model results show the decoupling between the groundwater seepage line and the shoreline?

✓ Both linear and non-linear forms of the Boussinesq equation were solved in two-dimensional mesh, which was more precise than the one-dimensional linear model solved in Muriwai Beach. A wide range of the field data was used in the numerical model. The three days fieldwork carried out in Ngarunui beach in September 2013 included a beach survey, groundwater seepage line survey, beach groundwater measurements, groundwater table measurement behind the beach dune and wave data collected in the swash zone. Beach survey data and groundwater measurements were used as the input data to the numerical model. The beach seepage line observations were also used for numerical model calibration and to compare with the model results. The output of the model included the groundwater exit point along

cross-shore transects and the alongshore variation of the groundwater seepage line during time. The results showed that both numerical models based on the linear and non-linear Boussinesq equation can predict the tidal groundwater changes across the beachface and determine the position of the groundwater exit point. However, my results showed that the seepage line calculated by the 2D non-linear Boussinesq model is more compatible with the surveyed groundwater seepage lines rather than linear model. The non-linearity effect of the hydraulic conductivity and the groundwater depth may play an important role in accuracy of the results.

✓ In terms of the decoupling process both linear and non-linear models showed that there is not much decoupling between the groundwater seepage line and the high tide shoreline. It indicated that the groundwater seepage line is just located a few metres onshore of the high tide shoreline. During the descending tide, the groundwater seepage face appears between the shoreline and the groundwater seepage line because of the groundwater exfiltration. Around the low tide the seepage face width reaches its maximum because of the decoupling between the *SL* and *GWSL*. The decoupling process determined by the numerical model supported my results from the video images analysis, which already showed the decoupling between extracted seepage lines from time-averaged images and extracted shorelines from variance images.

✓ The seepage face width, calculated by the numerical model, started to increase from the mid tide during the outgoing tide, reached the maximum around the low tide, and then decreased during the incoming tide. The difference between the seepage face variation in the linear and non-linear model was the extent of the seepage face during the incoming tide in the linear model. As field data and Solinst piezometers results at Ngarunui beach showed that the beach fills more easily than it drains and groundwater level increases much more quickly than the rising tide. Hence extending the seepage face with rising tide (as it was shown by the linear model) was unlikely to happen.

This research suggests a potential morphological feedback loop (Figure 7.1 A), where beach morphology influences the groundwater seepage line elevation and seepage face width both through beachface slope and beach hydraulic conductivity (according to the numerical model results obtained at Muriwai beach “chapter 3” and numerical model results, video images analysis and filed data analysis at Raglan beach “chapters 4, 5, 6”), which drive lower and higher beachface volume, which influence beach morphology (regarding the statistical studies at Muriwai beach “chapter 3”).

My findings also highlight the role of the non-linearity of the hydraulic conductivity in beach groundwater seepage line variation. The spatial distribution of the hydraulic conductivity seems to be more important that researchers previously thought.

This research may also suggests a potential surfzone morphodynamics feedback loop (Figure 7.1 B), where surfzone morphodynamics influences the groundwater seepage line elevation and seepage face width both through wave set-up effects and presence of rip currents (according to the numerical model results obtained at Raglan beach “chapters 6”), which drive lower and higher beachface volume (regarding the statistical studies at Muriwai beach “chapter 3”), which may influence surfzone morphodynamics. In this feedback loop, the effect of the surfzone morphodynamics on changing the beach morphology was emphasised, however the influence of the beach morphology on surfzone morphodynamics was not studied and can be the focus of future works.

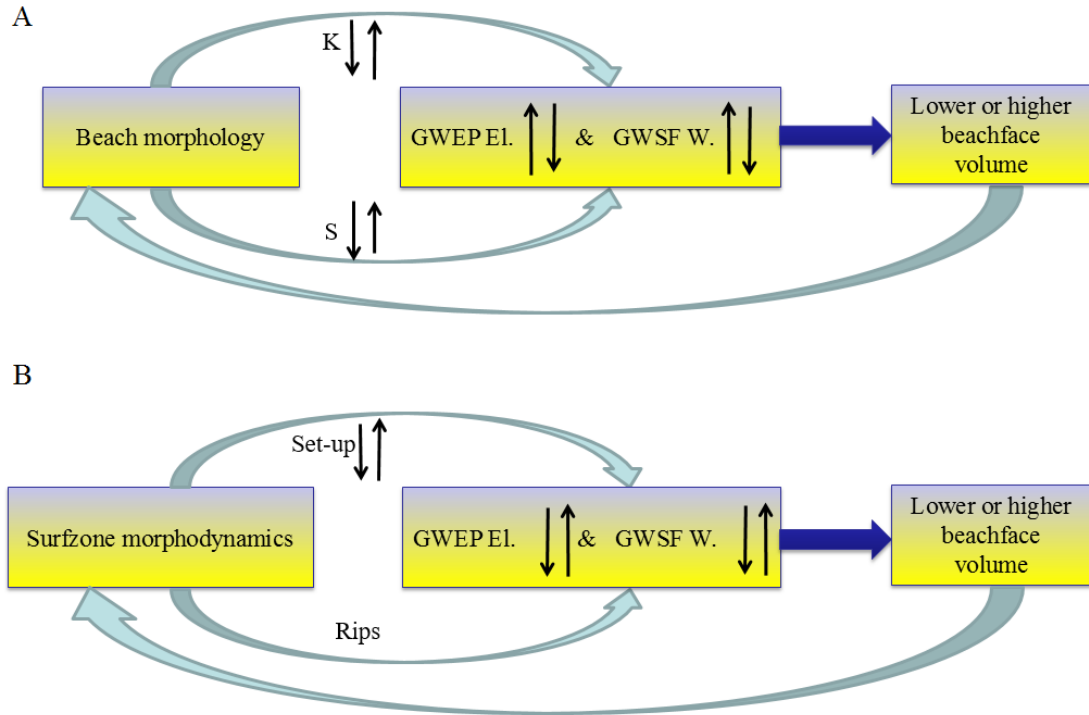


Figure 7.1 Potential beach morphological feedback loop (Panel A) and surfzone morphodynamics feedback loop (Panel B)

It should be noted that surfzone morphology factor (SM), which was used in the statistical analysis, was not good representation for the location of rips and surfzone morphology changes. Furthermore, the numerical model described in this thesis did not consider the spatially-varying wave set-up along the beach and just used the different wave set-up height with time. Hence, the effect of the spatially-varying wave set-up and the presence of rip currents on changing the beach groundwater elevation and the location of the seepage line can be the focus of future work on beach groundwater modelling, especially with the aspect of the beachface volume reduction and beach erosion due to the higher beach groundwater.

References

Aarninkhof S.G.J., Turner I.L., Dronkers T.D.T., Caljouw M., Nipius L., 2003. A video-based technique for mapping intertidal beach bathymetry. *Coastal Engineering* 49: 275–289.

Almar R., Coco G., Bryan K.R., Huntley D.A., Short A.D., Senechal N., 2008. Video observations of beach cusp morphodynamics. *Marine Geology* 254 (3–4), 216–223.

Baird A.J., Horn D.P., 1996. Monitoring and modelling groundwater behaviour in sandy beaches. *Journal of Coastal Research* 12 (3): 630-640.

Baird A.J., Mason T., Horn, D.P., 1998. Validation of a Boussinesq model of beach groundwater behaviour. *Marine Geology* 148: 55-69.

Bowen A.J., Inman D.L., Simmons V.P., 1968. Wave Set-Down and Set-Up. *Journal of Geophysical Research* 73(8): 2569-2577.

Brander R.W., Short A.D., 2000. Morphodynamics of a large-scale rip current system at Muriwai Beach, New Zealand. *Marine Geology*, 165: 27-39.

Bryan K.R., Robinson A., Briggs R.M., 2007. Spatial and temporal variability of titanomagnetite placer deposits on a predominantly black sand beach. *Marine Geology*, 236:45-59.

Castelle B., Bonneton P., Dupuis H., Senechal N., 2007. Double bar beach dynamics on the high energy meso-macrotidal French Aquitanian Coast: A review. *Marine Geology*, 245: 141-159.

Castelle B., Ruessink B.G., Bonneton P., Marieu V., Bruneau N., Price T.D., 2010. Coupling mechanisms in double sandbar systems. Part 2: impact on alongshore variability of inner-bar rip channels. *Earth Surface Processes and Landforms*, 35:771-781

Chickadel C.C., Holman R.A., Freilich M.H., 2003. An optical technique for the measurement of longshore currents. *Journal of Geophysical Research* 108, 3364

Drake T.G., Shreve R.L., Dietrich, W.E., Whiting, P.J., Leopold, L.B., 1988. Bedload transport of fine gravel observed by motion-picture photography. *Journal of Fluid Mechanics*, 192: 193-217.

Duncan J.R., 1964. The Effects of Water Table and Tide Cycle on Swash-Backwash Sediment Distribution and Beach Profile Development. *Marine Geology* 2: 186-197.

Eliot I.G., Clarke D.J., 1986. Minor storm impact on the beachface of a sheltered sandy beach. *Marine Geology*, 73: 61-83.

Eliot I.G., Clarke D.J., 1988. Semi-diurnal variation in beachface aggradations and degradation. *Marine Geology*, 79: 1-22.

Gorman R.M., Bryan K.R., Laing A.K., 2003. Wave hindcast for the New Zealand region: Deep-water wave climate. *New Zealand Journal of Marine and Freshwater Research*, 37:589-612.

Grant U.S., 1948. Influence of the water table in beach aggradation and degradation. *Journal of Marine Research*, 7: 655-660.

Guedes R.M.C., 2010. Raglan Field Experiment. Report, The University of Waikato.

Guo H., Jiao J.J., Li H., 2010: Groundwater response to tidal fluctuation in a two-zone aquifer. *Journal of Hydrology* 381: 364–371.

Haller M.C., Dalrymple R.A., Svendsen I.A., 2002. Experimental study of nearshore dynamics on a barred beach with rip channels. *Journal of Geophysical Research* 107. No. C6, 3061: 14-1 – 14-21

Harrison W., 1969. Empirical equations for foreshore changes over a tidal cycle. *Marine Geology*, 7: 529-551.

Hegge B.J., Masselink G., 1991. Groundwater-Table Responses to Wave Run-up: An Experimental Study from Western Australia. *Journal of Coastal Research* 7 (3): 623-634

Holland K.T., Holman R.A., 1993. The statistical distribution of swash maxima on natural beaches. *Journal of Geophysical Research* 98, 10271–10278.

Holland K.T., Raubenheimer B., Guza R.T., Holman R.A., 1995. Runup kinematics on a natural beach. *Journal of Geophysical Research* 100: 4985–4993.

Holman R.A., Lippmann T.C., O'Neill P.V., Hathaway K., 1991. Video estimation of subaerial beach profiles. *Marine Geology* 97: 225-231.

Holman I.P., 2006. Climate change impacts on groundwater recharge-uncertainty, shortcomings, and the way forward. *Hydrogeology Journal* 14: 637–647

Holman R.A., Stanley J., 2007. The history and technical capabilities of Argus. *Coastal Engineering* 54: 477–491.

Holman R.A., Sallenger A. H., 1985. "Setup and swash on a natural beach." *Journal of Geophysical Research* 90: 945-953.

Horn D.P., 2002. Beach Groundwater Dynamics. *Geomorphology* 48:121-146

Horn D.P., 2006. Measurements and modelling of beach groundwater flow in the swash-zone: a review. *Continental Shelf Research* 26: 622–652

Huisman C.E., Bryan K.R., Coco G., Ruessink B.G., 2011. The use of video imagery to analyse groundwater and shoreline dynamics on a dissipative beach. *Continental Shelf Research* 31: 1728-1738.

Jeng D.S., Barry D.A., Seymour B.R. Dong P., Li L., 2005. Two-dimensional approximation for tide-induced watertable fluctuations in a sloping sandy beach. *Advances in Water Resources* 28: 1040–1047.

Jeng D.-S., Seymour B.R., Barry D.A., Li L., Parlange J.-Y., 2005. New approximation for free surface flow of groundwater: capillarity correction. *Advances in Water Resources* 28:1032–1039.

Kirkham D., 1967. Explanation of paradoxes in Dupuit-Forchheimer seepage theory. *Water Resources Research*, 3: 609-622.

Koningsveld M.V., Davidson M., Huntley D., Medina R., Aarninkhof S., Jiménez J.A., Ridgewell J., Kruif A., 2007. A critical review of the CoastView

project: Recent and future developments in coastal management video systems. *Coastal Engineering* 54: 567-576.

Laurent J.C., 2000. The Provenance and Dispersal of Beach Sands on the West Coast of the North Island, New Zealand. Master's Thesis Earth Sciences, University of Waikato, Hamilton, New Zealand.

Lentz S., Raubenheimer B., 1999. Field observation of wave setup. *Journal of Geophysical Research* 104: 25867-25875

Li H., Boufadel M.C., Weaver J.W., 2008. Tide-induced seawater-groundwater circulation in shallow beach aquifer. *Journal of Hydrology* 352: 211-224.

Li H., Jiao J.J., 2003. Tide-induced seawater-groundwater circulation in a multi-layered coastal leaky aquifer system. *Journal of Hydrology* 274: 211-224.

Li L., Barry D.A., Pattiaratchi C.B., 1997. Numerical modelling of tide-induced beach water table fluctuations. *Coastal Engineering* 30: 105-123.

Li L., Barry D.A., Stagnitti F., Parlange J.Y., 1999. Tidal along-shore groundwater flow in a coastal aquifer. *Environmental Modeling and Assessment* 4: 179-188.

Li L., Barry D.A., 2000. Wave-induced beach groundwater flow. *Advances in Water Resources* 23 (4): 325-337.

Li L., Barry D.A., Stagnitti F., Parlange J.-Y., Jeng D.-S., 2000. Beach water table Fluctuations due to spring-neap tides: moving boundary effects. *Advances in Water Resources* 23: 817-824

Li L., Dong P., Barry D.A., 2002. Tide-induced watertable fluctuations in coastal aquifers bounded by rhythmic shorelines. *Journal of Hydraulic Engineering, ASCE* 128: 925-933

Li L., Barry D.A., Pattiaratchi C.B., Masselink. G., 2002. BeachWin: modelling groundwater effects on swash sediment transport and beach profile changes. *Environmental Modelling & Software* 17: 313-320

Li L., Horn D.P., Baird A.J., 2006. Tide-induced variations in surface temperature and water-table depth in the intertidal zone of a sandy beach. *Journal of Coastal Research*, 22(6): 1370-1381

Lippmann T.C., Holman R.A., 1989. Quantification of Sand Bar Morphology: A Video Technique Based on Wave Dissipation. *Journal of Geophysical Research*, 94: 995-1011

Lippmann T.C., Holman R.A., 1990. The spatial and temporal variability of sand bar morphology. *Journal of Geophysical Research* 95: 11575–11590.

Lippmann, T.C., Holman R.A., Bowen A.J., 1997. Generation of edge waves in shallow water. *Journal of Geophysical Research* 102, 8663–8679.

List J.H., Farris A.S., Sullivan C., 2006. Reversing storm hotspots on sandy beaches: Spatial and temporal characteristics. *Marine Geology*, 226: 261-279.

Lopez O.M., Jadoon K.Z., Missimer T.M., 2015. Method of Relating Grain Size Distribution to Hydraulic Conductivity in Dune Sands to Assist in Assessing Managed Aquifer Recharge Projects: Wadi Khulays Dune Field, Western Saudi Arabia. *Water*, 7(11), 6411-6426

Masterson J.P., Garabedian S.P., 2007. Effects of Sea-Level Rise on Ground Water Flow in a Coastal Aquifer System. *Ground Water* 45(2):209-217

Morris, B.D., Coco, G., Bryan, K.R., Turner, I.L., 2007. Video-derived mapping of estuarine evolution. *Journal of Coastal Research*, SI 50, 410–414.

Nielsen P., 1990. Tidal dynamics of the water table in beaches. *Water Resources Research*. 26: 2127-2135.

Nielsen P., 1999. Groundwater Dynamics and Salinity in Coastal Barriers. *Journal of Coastal Research* 15(3): 732-740

Odong J., 2007. Evaluation of Empirical Formulae for Determination of Hydraulic Conductivity based on Grain-Size Analysis. *Journal of American Science*, 3(3): 54-60

Parlange J.Y., Stagnitti F., Starr J.L., Braddock R.D., 1984. Free-surface flow in porous media and periodic solution of the shallow-flow approximation. *Journal of Hydrology*, 70: 251-263

Plant, N.G., Holman, R.A., 1997. Intertidal beach profile estimation using video images. *Marine Geology* 140, 1–24

Plant N.G., Aarninkhof S.G.J., Turner I.L., Kingston K.S., 2007. The Performance of Shoreline Detection Models Applied to Video Imagery. *Journal of Coastal Research* 23(3): 658-670.

Raubenheimer B., Guza R.T., Elgar S., 1999. Tidal water table fluctuations in a sandy ocean beach. *Water Resources Research*, 35(8): 2313-2320.

Raubenheimer B., Guza R.T., Elgar S., 2001. Field observations of wave-driven setdown and setup. *Journal of Geophysical Research* 106: 4629-4638.

Robinson A., 2004. The Interaction between Heavy Mineral Placers, Groundwater Seepage and Shoreface Morphology at Muriwai Beach. Master of Science Thesis, University of Waikato.

Ruessink B.G., Wijnberg K.M., Holman R.A., Kuriyama K., Van Enckevort I.M.J., 2003. Intersite comparison of interannual nearshore bar behavior. *Journal of Geophysical Research* 108.

Sallenger A.H., Holman R.A., Birkemeier W.A., 1985. Storm-induced response of a nearshore bar system. *Marine Geology* 64: 237–258.

Short A.D., Hesp P.A., 1982. Wave, beach and dune interactions in Southeastern Australia. *Marine Geology*, 48: 259–284.

Simarro G., Bryan K.R., Guedes R.M.C., Sancho A., Guillen J., Coco G., 2015. On the use of variance images for runup and shoreline detection. *Coastal Engineering* 99: 136-147.

Smith A.R., 1978. Color gamut transform pairs. *Siggraph* 78, Conference Proceedings: 12–19.

Smith R.K., Bryan K.R., 2007. Monitoring Beach Face Volume with a Combination of Intermittent Profiling and Video Imagery. *Journal of Coastal Research* 23(4): 892-898.

Song Z., Li L., Kong J., Zhang H., 2007. A new analytical solution of tidal water table fluctuations in a coastal unconfined aquifer. *Journal of Hydrology* 340: 256–260.

Thornton E.B., MacMahan J., Sallenger A.H., 2007. Rip currents, mega-cusps, and eroding dunes. *Marine Geology*, 240: 151-167

Turner I.L., 1993. Water table outcropping on macro-tidal beaches: A simulation model. *Marine Geology*, 115: 227-238.

Turner I.L., 1995. Modelling the Time-Varying Extent of Groundwater Seepage on Tidal Beaches. *Earth Surface and Landforms* 20: 833-843

Turner I.L., 1995. Simulating the influence of groundwater seepage on sediment transported by the sweep of the swash zone across macro-tidal beaches. *Marine Geology* 125: 153-174.

Turner I.L., Coates B.P., Acworth R.I., 1997. Tides, waves and the super-elevation of groundwater at the coast. *Journal of Coastal Research*, 13 (1): 46-60.

Turner I.L., Leatherman S.P., 1997. Beach dewatering as a 'soft' engineering solution to coastal erosion- A history and critical review. *Journal of Coastal Research*, 13 (4): 1050-1063.

Turner I.L., Nielsen P., 1997. Rapid water table fluctuations within the beach face: Implications for swash zone sediment mobility?. *Coastal Engineering* 32: 45-59.

Turner I.L., 1998. Monitoring groundwater dynamics in the littoral zone at seasonal, storm, tide and swash frequencies. *Coastal Engineering* 35: 1–16

Uunk L., Wijnberg K.M., Morelissen R., 2010. Automated mapping of the intertidal beach bathymetry from video images. *Coastal Engineering* 57: 461-469.

Walters R.A., Goring D.G., Bell R.G., 2001. Ocean tides around New Zealand. *New Zealand Journal of Marine and Freshwater Research* 35 (3), 567–580.

Weixing G., 1997. Transient groundwater flow between reservoirs and water-table aquifers. *Journal of Hydrology* 195: 370-384

Xiu-yuan M., Shu-guang L., Wei-shen Z., 2009. A new method in groundwater flow modelling. *Journal of Hydrodynamics* 21(2): 245-254

Appendix: Field Data Collection



Photo A-1. Beach and GWSL surveying on Wednesday 18th and Thursday 19th September 2013.



Photo A-2. ISD deployment, 27th August and 4th September 2013



Photo A-2. Continued



Photo A-3. Upper photo: designed tubes for installing in Solinst piezometers locations (longer tube for high tide piezometers and shorter ones for low tide piezometers). Middle and lower photos: high tide tube deployment in the second and third transects respectively.



Photo A-4. The location of dipwells in transect 3. Photo was taken around low tide (15:00) on Wednesday 18th September 2013. In the upper panel, blue color in top of the first onshore tube indicates the third transect (green for transect 1, red for 2 and blue for 3). The high tide Solinst piezometer (SHT) was installed in this tube. Dipwells were located almost 30 m far from each other between SHT and SLT.



Photo A-5. Location of the ADV, which was buried in the swash zone close to the low tide Solinst piezometer in the second and third transects.



Photo A-5. Continued



Photo A-5. Continued